

Integrated Photonics Filters with Distributed Bragg Reflector in Silicon-on-Insulator

A THESIS

submitted by

PARIMAL SAH

for the award of the degree

of

DOCTOR OF PHILOSOPHY



**DEPARTMENT OF ELECTRICAL ENGINEERING.
INDIAN INSTITUTE OF TECHNOLOGY MADRAS.**

Friday 6th April, 2018

THESIS CERTIFICATE

This is to certify that the thesis titled **Integrated Photonics Filters with Distributed Bragg Reflector in Silicon-on-Insulator**, submitted by **PARIMAL SAH**, to the Indian Institute of Technology, Madras, for the award of the degree of **Doctor of Philosophy**, is a bonafide record of the research work done by him under my supervision. The contents of this thesis, in full or in parts, have not been submitted to any other Institute or University for the award of any degree or diploma.

Dr. Bijoy Krishna Das
Research Guide
Associate Professor
Dept. of Electrical Engineering
IIT-Madras, 600 036

Place: Chennai, India

Date: Fri 6th Apr, 2018

Honesty is the best policy

-Anonymous

Dedicated to my **Family**
for their eternal love and support

ACKNOWLEDGEMENTS

My devotion towards work culture, skill to grow in a proficient group and potential to work scientifically got ameliorated with wonderful experience throughout my stay at IIT Madras for the Ph.D. program.

First and foremost, I would like to thank my supervisor, *Prof. Bijoy Krishna Das*, for his guidance and support over the course of this work throughout my time IIT Madras. His extraordinary dedication towards work and positive attitude to handle tough situations motivated me to work patiently and perfectly. He not only helped me to understand theories of integrated photonics but also taught me an intuitive way of analysis of research problem at hand.

I thank all my doctoral committee members, Prof. Prem Bisht, Dr. Balaji Srinivasan, Prof. Amitava Das Gupta and Dr. Sujatha N for their valuable comments and suggestions during the review meetings. I express my thanks to Mr. C. Rajendran, Jr. technical superintendent, Mr. J. Prakash, Jr. technician and Mr. T. Sridhar for their technical support in MEMS & Microelectronics lab.

I express my sincere thanks to Dr. Shantanu Pal my senior, for his important guideline for a peaceful research. He taught me the skill to align different optical components for end-fire coupling experiment. I am deeply thankful to Dr. Sujith Chandran my senior, for his advice and guidance in learning electron beam lithography techniques. I thank Sreevatsa Kurudi for developing LabView programs to automate the experimental setups that made many of our experiments possible with lesser time and effort. I am thankful to Sanjay Sahoo and Rajan Mishra who not only helped in technical aspect but also accompanied me in entertainment times. I would like to thank my close friend Satyajeeet Singh, Rana Pratap and Varun Singh for their wise advice and a constant source of moral support. I spent most of the leisure time with them in sharing our academic and non-academic matters. I thank my fellow labmates S. Meenatchi Sundaram, Siddharth, Riddhi, Sumi, Ramesh, Sooraj, Dadavaili, Chaithanya, Vivek, Seetha Lak-

shmi, Amrutha, Arijit Misra, Keerthana for their wishes and encouragements, Arnab, Pankaj, Meena and Shubhrajyoti for their wishes and encouragements.

I would like to acknowledge my parents (Father: *Shree Yogendra Narayan Sah* and Mother: *Shrimati Geeta Devi*), brothers and sisters for their love and supports throughout my life. I am also indebted to my in-laws for taking care of my personal life. Finally, all credit goes to my wife *Prachi*, she solely has taken all the responsibilities herself to take care of our daughter *Kavya*, and look after both of our families which allowed me to chase my dream. Without her love, support, care, efficient managerial skill and motivation, I could not have completed my Ph.D.

ABSTRACT

KEYWORDS: Silicon Photonics, Silicon-on-Insulator, Waveguides, Integrated Optics, Distributed Bragg Reflector, Integrated Bragg Grating, Rectangular Edge Filter, Optical Filter, Photonic Passband.

Various integrated optical distributed Bragg reflector (DBR) structures are investigated in a search for new wavelength filter devices which might be useful for futuristic multi-functional integrated silicon photonics. Starting from intuitive concepts to novel device designs, their fabrication process optimization, and characterizations of these devices have been carried out within the scope of this thesis. The design parameters are studied/optimized following the trend of CMOS compatible silicon photonics technology in silicon-insulator substrate with device layer thickness of 220 nm and 250 nm (BOX layer thickness: 2-3 μm , handle wafer thickness: 500 μm). However, for all experimental demonstration, we have used only the device layer thickness of 250 nm (procured from Soitec, France). The DBR structures were defined by periodic modulation of waveguide width; enabling both waveguide and DBR structures to be defined simultaneously using single lithographic step.

Initially, DBR and DBR cavity were designed in a single mode waveguide with gratings at both side walls with waveguide width 560 nm, slab height 150 nm, grating modulation 50 nm (each side), cavity length 145 nm and grating length 500 μm . The experimental results for the DBR devices fabricated with these parameters are: $R > 99\%$, $Q\text{-factor} = \sim 10^5$ at $\lambda_B \sim 1600$ nm for $\Lambda = 290$ nm, which is in close agreement with theory noting that $\frac{d\lambda_B}{d\Lambda} \sim 5.5$ nm/nm. After successful demonstration of DBR and DBR cavity, a novel design of integrated optical design of razor-edge filter device was demonstrated with a multi-mode waveguide (supporting at least two modes) with asymmetric side-wall grating, which is adiabatically interfaced with input/output single-mode waveguides. The input/output access waveguides are terminated with grating couplers for optical characterizations. Design parameters are optimized for a sharp

razor-edge filter response in optical C-band ($1530 \text{ nm} \leq \lambda_{edge} \leq 1565 \text{ nm}$). The sub-micron features and the entire footprint of the devices were defined with a single-step e-beam lithography process using negative-tone resist and subsequent dry etching of $\sim 100 \text{ nm}$ using an inductively coupled reactive ion etching system. All the fabricated devices exhibit a razor-edge filter response at $\lambda_{edge} \sim 1560 \text{ nm}$ with an edge-extinction of $> 40 \text{ dB}$ at the rate of 118 dB/nm . The razor-edge step is followed by a broad passband of $\sim 40 \text{ nm}$ till the first order Bragg reflected wavelength of $\lambda_B^{00} \sim 1600 \text{ nm}$ in the transmission characteristics obtained for $1520 \text{ nm} \leq \lambda \leq 1620 \text{ nm}$. Tunability of a razor-edge filter is verified with cladding refractive index change and the observed refractive index sensitivity of the edge is $\sim 18 \text{ nm/RIU}$. The limit of detection for 1-dB transmitted power extinction at λ_{edge} of a typical fabricated device is estimated to be $5.3 \times 10^{-4} \text{ RIU}$.

Finally, a photonic passband filter device is designed with a multi-mode waveguide with side wall grating, which is adiabatically interfaced with input/output single-mode waveguides. We have demonstrated first time the optical passband filter in transmission port of waveguide. The pass-bands are bounded by two highly extinguished stop-bands (with an extinction of $> 35 \text{ dB}$ with edge roll-off of $> 70 \text{ dB/nm}$) of $\Delta\lambda_{sb} > 15 \text{ nm}$. The existence of two stopbands is due to two Bragg phase-matching conditions. As the filter response is in the transmission, flat-top is naturally achieved however passband ripple were further minimized within $\sim 1 \text{ dB}$ by providing an adiabatic taper at input and output interfaces of DBR grating. The bandwidth is further narrowed down by cascading two gratings with detuned parameters. A semi-analytical model is used to analyze the filter characteristics ($1500 \text{ nm} \leq \lambda \leq 1650 \text{ nm}$). The pass bandwidth of waveguide devices integrated with single-stage gratings are measured to be $\sim 24 \text{ nm}$, whereas for the device with two cascaded gratings with slightly detuned periods ($\Delta\Lambda = 2 \text{ nm}$) exhibit pass bandwidth down to $\sim 10 \text{ nm}$. The characterization results are found to be consistent with theoretical predictions.

The special filter characteristics of the above mentioned DBR devices may find potential applications such as refractive index sensor, thermo-optic switching, intensity modulator, noise filter for nonlinear devices and/or Raman spectroscopy.

TABLE OF CONTENTS

ACKNOWLEDGEMENTS	v
ABSTRACT	vii
LIST OF TABLES	xii
LIST OF FIGURES	xx
ABBREVIATIONS	xxi
NOTATION	xxiii
1 Introduction	1
1.1 Motivation	2
1.2 Research Objective	12
1.3 Thesis Organization	14
2 Waveguide DBR and DBR Cavity	16
2.1 SOI Waveguide Design	17
2.2 DBR in Single Mode Waveguide	25
2.2.1 Phase Matching Conditions	27
2.2.2 Coupling Co-efficient	32
2.2.3 DBR: Simulation Results	35
2.2.4 $\lambda/4$ Phase-Shifted DBR Cavity	38
2.3 Experimental Results and Discussion	41
2.3.1 Mask Layout	42
2.3.2 Stitch Field Error Correction	44
2.3.3 Proximity Error Correction	45
2.3.4 Device Fabrication : Optimized Process Parameters	48

2.3.5	Characterization Results	49
2.4	Fabrication Tolerance	57
2.5	Summary	58
3	Rectangular-Edge Filter	61
3.1	Design and Theoretical Analysis	63
3.1.1	Numerical Evaluation of Bragg Wavelength	66
3.1.2	REF Device Parameters Optimization	70
3.2	Simulation Results	77
3.2.1	Adiabatic Taper Design	78
3.2.2	FDTD Simulations	80
3.2.3	Thermal Detuning	85
3.2.4	Effect of Cladding Material	87
3.3	Experimental Results and Discussions	88
3.3.1	Fabrication	88
3.3.2	Experimental Results	91
3.3.3	Tunability of the REF Characteristics	94
3.4	Summary	96
4	Photonic Passband Filter	98
4.1	Limitations of Single Stage DBR on Pass Bandwidth	101
4.2	Device Description and Design	104
4.3	Experimental Results and Discussions	107
4.3.1	Device Fabrication	107
4.3.2	Photonic Passband Filter: Single-Stage DBR	111
4.3.3	Photonic Passband Engineering: Cascaded DBR	113
4.4	Fabrication Tolerance	115
4.5	Summary	116
5	Conclusion	118
5.1	Thesis Summary	118
5.2	Future Scopes	121

A	List of Publications Based on Thesis	122
A.0.1	Patent	122
A.0.2	Journal	122
A.0.3	Conference (Presentations / Proceedings/Workshop)	122

LIST OF TABLES

2.1	Range of waveguide width allowing one, and/or two, and/or three mode(s) confinement at three different slab height calculated at $\lambda = 1550$ nm.	21
2.2	Wafer cleaning	41
2.3	Optimized parameters for waveguide and grating fabrication	51
2.4	Slope of effective index versus W, h curves at W = 760 nm, H = 250 nm and h = 150 nm	58
2.5	Figure of merit comparisons of DBR cavity with earlier reported works.	59
3.1	Cut-off width of the waveguide for higher order modes calculated for three different values of slab heights h , assuming $H = 250$ nm.	72
3.2	REF device parameters of waveguide and grating used for FDTD simulation	81
3.3	FDTD simulation parameters	81
4.1	Device specifications for the fabricated devices as shown in Fig. 4.7(a).	108
4.2	Device parameters extracted from the experimental results shown in Fig. 4.10.	112

LIST OF FIGURES

1.1	Block diagram of the optical memory system demonstrated in 2015 [21].	2
1.2	A schematic of integrated silicon photonic chip for quantum application. It includes photon sources, pump-removal filters, passive and active optics, single-photon detectors, and control and feedback electronics (moving from left to right on circuit). Besides various devices such as microring resonator, Mach-Zehnder interferometer, thermo-optic phase-shifter, DBR is also proposed for filtering application [26].	3
1.3	Schematic diagram of a proposed wavelength-selectable optical add-drop multiplexer [77].	6
1.4	(a) The quarter-wave phase-shifted Bragg grating modulator scheme (top) and its cross-section view (bottom); and (b) measured transmission characteristic with various reverse-bias voltages applied to the device [81].	7
1.5	(a) Schematic of DBR based broadband filter device. The wavelength reflected at the first contra-directional DBR is reflected again by an identical contra-directional DBR. The metal heaters control both contra-DCs; (b) reflection characteristic of the device for different temperatures applied to only one contra-DC; and (c) spectral response with the heat applied to both contra-DCs [78].	8
1.6	(a) Schematic of the spiral DBR with the minimum bending radius of R_0 . (b) grating details shown by zoom-in view. Λ : grating period, W_{corr} : corrugation width, g : waveguide spacing, and (c) Transmission spectra of the device with (a) $R_{=0} = 20 \mu\text{m}$. The experimental spectra and modeled spectra is shown in solid black lines and the dashed red lines respectively [91].	10
1.7	(a) The schematic of the integrated biosensor with phase shifted vertical side wall grating, and (b) spectral response of two-phase shifted grating for different channel fluid refractive indices [52].	11
1.8	A cartoon to represent rectangular edge filter using DBR integrated with a multimode waveguide interfaced with single-mode input/output waveguide (at middle). Input-output wavelength characteristics are also shown (at left/right).	13

1.9	A cartoon to represent a cascaded DBR (DBR ₁ and DBR ₂) of different periodicity (Λ_1 and Λ_2) integrated with a multimode waveguide, and interfaced with single-mode input/output waveguide (at middle). The expected input-output wavelength characteristics are also shown (at left/right).	14
2.1	A cross sectional view of a SOI wafer.	16
2.2	3D schematic of rib waveguide in SOI; cross section of the rib waveguide with parameters: waveguide width W , rib height H and slab height h	17
2.3	Effective indices of various TE and TM guided modes($\lambda = 1550$ nm) vs waveguide width calculated for device layer thickness or waveguide height $H = 250$ nm with slab heights: (a) $h = 0$ nm, (b) $h = 50$ nm, (c) $h = 70$ nm, (d) $h = 100$ nm and (e) $h = 120$ nm.	19
2.4	Effective indices (n_{eff}^{00} , n_{eff}^{01} and n_{eff}^{02}) of the guided modes vs waveguide width (supporting only TE-like guided modes), calculated for two different device layer thickness and slab height h as a parameter at an operating wavelength $\lambda = 1550$ nm: (a) $H = 220$ nm and (b) $H = 250$ nm, and slab height as parameter.	20
2.5	Cut-off width for 1 st order guided mode (represented by W_1^{cut}) and 2 nd order guided mode (represented by W_2^{cut}) as a function of slab heights h calculated for two different values of device layer thickness (220 nm, 250 nm). The results are plotted for TE -like guided modes at $\lambda = 1550$ nm.	20
2.6	Effective indices of the guided modes as a function of waveguide slab height calculated for $H = 250$ nm and waveguide width as parameter at $\lambda = 1550$ nm (supporting only TE-like guided modes).	21
2.7	The electric field amplitude distribution of guided fundamental modes calculated for $W = 500$ nm, and $h = 0$ nm, at an operating wavelength $\lambda = 1550$ nm: (a) and (b) are dominant component $\mathcal{E}_x(x, y)$ and $\mathcal{E}_y(x, y)$ for the fundamental mode TE_{00} and TM_{00} , respectively calculated for device layer thickness $H = 220$ nm; (c) and (d) are dominant component $\mathcal{E}_x(x, y)$ and $\mathcal{E}_y(x, y)$ for the fundamental mode TE_{00} and TM_{00} , respectively calculated for device layer thickness $H = 250$ nm. . . .	22
2.8	The electric field amplitude distribution for the dominant component $\mathcal{E}_x(x, y)$ of guided TE-modes obtained for $W = 760$ nm, and $h = 150$ nm at a operating $\lambda = 1550$ nm: (a) and (b) are TE_{00} and TE_{10} , respectively calculated for device layer thickness $H = 220$ nm; (c) and (d) are TE_{00} and TE_{10} , respectively calculated for device layer thickness $H = 250$ nm.	23

2.9	Effective indices of the guided modes as a function of operating wavelength, calculated for a device layer thickness of $H = 250$ nm, slab height $h = 150$ nm and waveguide width as parameter (supporting only TE-like guided modes): (a) single-mode regime, and (b) multimode regime (supporting two lower order guided modes).	24
2.10	3D schematic of a SOI waveguide integrated with a DBR and input/output grating couplers (GC_i / GC_o).	25
2.11	(a) 3D schematic of input Grating coupler and (b) Schematic of input Grating coupler (GC_i) showing wave vectors: incident \vec{AO} , undiffracted transmitted \vec{OB} and diffracted guided \vec{OE}	28
2.12	Schematic representation of Bragg reflection with wavevector diagram with β_k, β_n and G are the wavevector of k_{th} order forward propagating mode, n_{th} order backward propagating mode and grating wavevector respectively.	31
2.13	(a) 3D scheme of a DBR structure with symmetric waveguide width modulation in SOI along with its design parameters, (b) the corresponding cross-sectional view. The hashed regions indicate the modal overlapping with the grating perturbation.	32
2.14	Coupling coefficient versus wavelength calculated for single mode waveguide of $W = 650$ nm and $h = 150$ nm for two device layer thickness (220 nm and 250 nm) with ΔW as parameter.	34
2.15	Coupling constant versus grating modulation width calculated for single mode waveguide of $W = 650$ nm and h as parameter (a) for $H = 220$ nm, and (b) for $H = 250$ nm. The mode fields were computed at $\lambda = 1550$ nm.	34
2.16	Schematic representation of top view of DBR in a single mode waveguide with period Λ and length L_g . E_{in}^f and E_{in}^b are the forward and backward propagating electric field amplitude at the input of the grating, and E_{out}^f and E_{out}^b are the forward and backward propagating electric field amplitude at the output of the grating. Example of input, reflected and transmitted characteristics are also shown.	35
2.17	(a) Transmission and (b) reflection spectrum of the DBR grating integrated in single mode SOI waveguide with W, H, h as 560 nm, 250 nm, 150 nm, respectively and $\Lambda, \Delta W, L_g$ as 282 nm, 50 nm, 500 μm , respectively. It is plotted using transfer matrix method for DBR. . .	37
2.18	(a) 3D schematic of device with $\lambda/4$ phase-shifted cavity. In cross sectional view, W_1, W_2, H, h are waveguide width in input output, waveguide width at grating region, core height and slab height respectively. . .	39

2.19	Transmission spectrum of a DBR cavity with symmetric side-wall grating integrated in a single mode SOI waveguide with W , H , h as 560 nm, 250 nm, 150 nm, respectively and Λ , ΔW , L_g as 282 nm, 50 nm, 250 μm at each side of a BGR cavity of length 141 nm, respectively. It is plotted using transfer matrix method for DBR cavity. (inset: the enlarged view of the resonance peak at $\lambda_r \sim 1550$ nm.	40
2.20	Schematic of 3D wafer containing waveguide, DBR grating and DBR grating cavity with input/output grating coupler at each step of fabrication process flow: (a) Starting SOI wafer, (b) HSQ masked wafer (mask is shown in blue colour), (c) Etched wafer using ICPRIE system (with HSQ mask covering top surface of devices) and (d) Final wafer with devices; arrow direction shows the intermediate process between the two connecting wafer stages.	42
2.21	Mask layout (designed using Raith NANOSUITE) of (a) DBR devices, labels indicate i. alignment marker, ii. grating coupler, iii. FBMS path as waveguide, iv. DBR and v. write field shown by dotted square; (b) alignment marker and (c) taper connecting grating coupler to waveguide, conventional arms, and FBMS path are shown by arrow.	43
2.22	(a) Mask layout of DBR with conventional areas, waveguide with FBMS path and write field crossing line, (b) SEM images of DBR device showing stitch field error (horizontal and vertical displacement) at write field crossing line, and (c) SEM images of DBR device showing stitch field induced unwanted grating tooth at write field crossing line.	44
2.23	SEM images of input grating coupler showing proximity error (a) due to FBMS path kept near to conventional path, (b) due to FBMS path kept away to conventional path and (c) due to FBMS path kept away to conventional path and reduced conventional path dose.	46
2.24	SEM image of an integrated DBR waveguide (a) cross sectional view and (b) side view. The image was taken at 45 degree inclination of the sample with horizontal. The etch depth is ~ 100 nm on a device layer thickness of 250 nm.	47
2.25	SEM images of (a) input grating coupler, (b) tapered part of input grating coupler, (c) out grating coupler and (d) tapered part of output grating coupler	50
2.26	SEM image of the grating coupler showing duty ratio of ~ 50 % with grating period - 610 nm.	50
2.27	SEM images of the fabricated devices in a single mode SOI waveguide: (a) straight waveguide, (b) DBR grating and (c) phase shifted grating.	51

2.28	(a) A photograph of the characterization setup showing input/output fiber holder and device under test (DUT) and (b) Scheme of the experimental set-up used for device characterizations, $GC_{i/o}$ - grating input/output couplers, TLS - tunable laser source ($1520 \text{ nm} \leq \lambda_L \leq 1620 \text{ nm}$, $P_L = 250 \mu\text{W}$), OSA - optical spectrum analyzer, DBR - distributed Bragg reflector. TLS is accessed from the in-built OSA system (Apex 2043B).	53
2.29	Schematic representation of fabrication process flow of the three devices (straight waveguide, DBR grating and DBR grating cavity) in SOI with input/output grating coupler: (a) starting SOI wafer, (b) Devices patterned with e-beam resist HSQ, (c) Devices after dry etching of patterned devices and (d)	54
2.30	Transmission spectra of the DBR grating with waveguide parameters: $W = 560 \text{ nm}$, $H = 250 \text{ nm}$, $h = 150 \text{ nm}$; grating parameters: $\Lambda = 290 \text{ nm}$, $\Delta W = 50 \text{ nm}$ at both the side walls of the waveguide.	55
2.31	Transmission spectra of the DBR grating cavity with waveguide parameters: $W = 560 \text{ nm}$, $H = 250 \text{ nm}$, $h = 150 \text{ nm}$; grating parameters: $\Lambda = 290 \text{ nm}$, $\Delta W = 50 \text{ nm}$ at both the side walls of the waveguide with cavity length $L_c = 145 \text{ nm}$	56
2.32	Transmission spectra of a DBR grating cavity with top cladding as air (in black colour) and water (in red colour).	57
3.1	Schematic representation of the proposed REF device: (a) 3D schematic view of the proposed device and generic cross-sectional view of the SOI rib waveguide with design parameters W , H and h ; BOX - buried oxide. The handle silicon layer (typical thickness of $\sim 500 \mu\text{m}$) has not been shown below the BOX layer (typical thickness $1\text{-}3 \mu\text{m}$) in the scheme; (b) top view showing grating in one of the side-walls; A, B, C and D represent typical guided mode field distributions; β'_0 , β_0 , β_1 and β_{slab} are the propagation constants (arrow heads represent the direction of propagation);	63
3.2	Expected wavelength spectrum of a REF device. The stopbands are shown to be resulting due to coupling between different mode pairs. They are centered at phase matched wavelengths: λ_B^{00} , λ_B^{01} and λ_{slab}^m ($m > 1$)	65
3.3	Flowchart: Iterative flowchart to compute Bragg wavelengths and effective indices	68
3.4	(a) Effective refractive indices versus wavelength; waveguide width being a parameter; (b) plot of the cut-off wavelength versus waveguide width	69

3.5	Bragg wavelength convergence in iterative manner at $\Lambda = 290$ nm; waveguide width being the parameter. At $\sim 6^{th}$ iteration, Bragg wavelengths start converging. The effective indices were calculated for $H = 250$ nm and $h = 150$ nm.	69
3.6	Bragg wavelengths ($\lambda_B^{00}, \lambda_B^{01}$) obtained from iterative computation versus waveguide width for different grating periods. The effective indices were calculated for $W = 560$ nm, $H = 250$ nm and $h = 150$ nm. . . .	70
3.7	Effective indices of the guided modes vs waveguide width (supporting only TE-like guided modes) calculated for a fixed device layer thickness of $H = 250$ nm and slab height as parameter.	71
3.8	Cross section of a SOI rib waveguide with side wall grating at one side (hashed line shows the grating overlap region). The device parameters are defined as: device later thickness H , slab height h and waveguide width W_1 and W_2 with and without grating perturbations respectively.	73
3.9	(a) Coupling constants κ_{00} and κ_{01} for backward propagating fundamental and first order modes respectively as a function of grating modulation width ΔW . The values are calculated by evaluating mode-field distributions for a waveguide width of $W_2 = W_1 + \Delta W$, where $W_1 = 560$ nm, $H = 250$ nm, and $h = 150$ nm; (b) the distribution of electric field amplitude for the fundamental mode $\mathcal{E}_{0y}(x,y)$; and (c) the distribution of electric field amplitude for the 1st order mode $\mathcal{E}_{1y}(x,y)$, both calculated for $W_2 = 760$ nm.	74
3.10	Schematic representation of coupling constant κ_{00} and κ_{01} in side wall gratings. (a) symmetric side wall grating with propagating mode field profile, (b) integrand for κ_{00} , (c) integrand for κ_{01} , and (d) asymmetric side wall grating with propagating mode field profile, (e) integrand for κ_{00} , (f) integrand for κ_{01} . The notations represent: A - forward propagating mode, B - backward propagating mode and C - overlap area within the grating modulation region.	76
3.11	(a) Schematic of step transition in waveguide width connecting input/output waveguide to grating region and (b) power coupling efficiency into forward propagating fundamental and 1st order modes, and their sums as a function of ΔW for abrupt junction with $W_1 = 560$ nm.	79
3.12	(a) Schematic of step transition in waveguide width connecting input/output waveguide to grating region and (b) power coupling efficiency into forward propagating fundamental and 1st order modes, and their sums as a function of taper length L_T between $W_1 = 560$ nm and $W_2 = 760$ nm.	80
3.13	(a) 3D schematic of a symmetric side wall grating. FDTD simulation spectrum for a symmetric side wall grating: (a) transmission spectrum, (b) reflection spectrum. The parameter values used for the simulation are $W_1 = 560$ nm, $H = 250$ nm, and $h = 150$ nm, $\Delta W = 200$ nm, $\Lambda = 290$ nm, $L_g = 100$ μm	82

3.14	FDTD simulation for four different device lengths: (a) transmission spectrum, (b) reflection spectrum. The parameter values used for the simulation are $W_1 = 560$ nm, $\Delta W = 200$ nm, $H = 250$ nm, and $h = 150$ nm.	83
3.15	(a) Effective indices versus waveguide temperature plot and (b) Bragg wavelength versus waveguide temperature plot for a SOI rib waveguide with parameters: $W = 760$ nm, $H = 250$ nm and $h = 150$ nm. The calculation was done along a fixed cross section.	85
3.16	Transmission characteristics (obtained by FDTD simulation) at two different temperatures: $T_1 = 300$ K and $T_2 = 325$ K.	86
3.17	Transmission characteristics (obtained by FDTD simulation) by varying top cladding material as air (in black) and water (in red). The parameters used for the device are $W_1 = 560$ nm, $\Delta W = 250$ nm, $H = 200$ nm, and $h = 150$ nm.	87
3.18	Mask layout of REF devices, green colour represents straight waveguide interfaced with input/output grating couplers, red colour in the middle of devices represents the DBR (a) with $\Delta W = 200$ nm (10 devices) and $\Delta W = 0$ nm (two devices), (b) with $\Delta W = 150$ nm to 200 nm in the step of 10 nm (six devices) and $\Delta W = 0$ nm (two devices).	89
3.19	Mask layout of REF devices, green colour represents straight waveguide, red colour bars represents the DBR (a) with $\Delta W = 150$ nm and (b) with $\Delta W = 200$ nm.	90
3.20	SEM images showing top view of rib waveguide ($W = 560$ nm, $H = 250$ nm, and $h = 150$ nm) with side-wall grating modulation: (a) $\Delta W = 150$ nm, and (b) $\Delta W = 200$ nm	91
3.21	Typical transmission characteristics of a REF device with $L_g = 500$ μ m, $\Delta W = 200$ nm (red), and that for a reference waveguide without DBR grating (black).	92
3.22	Normalized edge-filter characteristics (in C-band) of seven different REF devices (D1 to D7) each fabricated with $L_g = 500$ μ m, and $\Delta W = 200$ nm each.	93
3.23	Normalized transmission characteristics of six REF devices (D8 to D13) with ΔW varying from 150 nm to 200 nm in steps of 10 nm (each devices has DBR length $L_g = 500$ μ m). Inset: slope of the transmitted power $S_{edge} = \frac{dP_T}{d\lambda}$ as a function of ΔW estimated at -20 dB transmission at the edge.	94
3.24	Normalized transmission characteristics of a 500- μ m-long REF device (D5) with top cladding materials as air (black) and DI water (red).	95
3.25	Sharp-edge filter characteristics of the devices for air cladding (in black) and DI water cladding (in red): (a) device with $\Delta W = 200$ nm (D5), and (b) device with $\Delta W = 180$ nm (D10).	96

4.1	Schematic of grating assisted design (top view) of (a) Y-junction, (b) Multi-mode-interferometer and (c) Mach-Zehnder interferometer. The example of expected wavelength spectrum at each ports are also shown.	99
4.2	A cartoon to represent rectangular edge filter using integrated Bragg grating with the DBR device, input-output wavelength characteristics shown together.	100
4.3	Calculated spectral widths of photonic passband ($\Delta\lambda_{pb}$) and its center wavelength (λ_C), and side stopbands ($\Delta\lambda_{sb}^{00}$ and $\Delta\lambda_{sb}^{01}$) as a function waveguide width W_2 supporting only two lower order modes in TE-polarization, for three different grating periods.	103
4.4	Schematic of 3D integrated cascaded grating devices with grating period Λ_1 and Λ_2 ; the cross section of the device with the device parameters: W_1, W_2 - waveguide widths, H, h - core height and slab height is shown at bottom right corner.	104
4.5	Schematic representation of the transmission spectra of the proposed photonic bandpass filter devices: (a) DBR ₁ with period Λ_1 ; (b) DBR ₂ with period Λ_2 ; and (c) cascaded DBR ₁ and DBR ₂ as represented in Fig. 4.4.	105
4.6	Normalized effective group delay τ/τ_0 and reflectance R of a DBR as function of wavelength.	106
4.7	Optical photographs of fabricated (a) whole sample with all the sets of devices and (b) one set of devices.	109
4.8	SEM images of fabricated devices: (a) adiabatically tapered grating of periodicity 288 nm; and (b) transition region of two cascaded DBR gratings of $\Lambda_1 = 290$ nm and $\Lambda_2 = 288$ nm.	110
4.9	Transmission spectra of three multimode waveguides each integrated with 250- μ m-long DBR grating ($\Lambda = 282$ nm, $\Delta W = 350$ nm) in one of the side-walls of a multimode waveguide with W, H, h as 560nm, 250 nm and 150 nm, respectively. Their average transmission spectrum (red color) and the transmission spectrum corresponding to a reference waveguide (black color) are also shown.	111
4.10	Transmission characteristics of DBR devices with grating period $\Lambda = 282$ nm - 292 nm, in step of 2 nm with $L_g = 250$ μ m grating ($\Lambda = 282$ nm, $\Delta W = 350$ nm) in one of the side-walls of a multimode waveguide with W, H, h as 560nm, 250 nm and 150 nm	112
4.11	Transmission spectra of two single stage DBR (with different periodicity) and one cascaded DBR (with periodicity Λ_1 and Λ_2) (a) for DBR of period 288 nm, 290 nm, and their cascade, and (b) for DBR of period 290 nm, 292 nm, and their cascade. The DBR with $L_g = 250$ μ m grating, $\Lambda = 282$ nm, $\Delta W = 350$ nm was integrated in a multimode waveguide with W, H, h as 560nm, 250 nm and 150 nm, respectively.	114

ABBREVIATIONS

Acronyms

C-Band	Conventional wavelength band ($\lambda \sim 1527$ to 1567 nm)
L-Band	Long wavelength band ($\lambda \sim 1567$ to 1607 nm)
WDM	Wavelength-division-multiplexing
BOX	Buried Oxide
CMOS	Complementary Metal Oxide Semiconductor
DBR	Distributed Bragg Reflector
DI	De-ionized (water)
EOE	Electrical-Optical-Electrical
DUT	Device Under Test
FSR	Free Spectral Range
ICP	Inductively Coupled Plasma
MZI	Mach Zehnder Interferometer
OADM	Optical Add-Drop Multiplexer
RIE	Reactive Ion Etching
SEM	Scanning Electron Microscope
SMF	Single Mode Fiber
SOI	Silicon-On-Insulator
SGW	Sub-Wavelength Grating
TE	Transverse Electric (polarization)
TM	Transverse Magnetic (polarization)

Chemical Names

CHF₃	Tri-fluoro Methane
HF	Hydrofluoric Acid
HNO₃	Nitric Acid
H₂O	Water

H₂O₂	Hydrogen Peroxide
H₂SO₄	Sulphuric Acid
NH₄OH	Ammonium Hydroxide
SF₆	Sulfur Hexafluoride
Si	Silicon
SiO₂	Silicon dioxide
TCE	Tri-chloro Ethylene

Units

dB	decibel
dBm	decibel milli-watt
mW	milli watt
μW	micro watt
μm	micrometer
ns	nano Second
μC	micro Coulomb
sccm	standard cubic centimeter per minute
mTorr	milli-Torr (of pressure)
mbar	milli-Bar (of pressure)
ml	milli-liter (of fluid)

NOTATION

\mathbf{n}	Refractive index
\mathbf{n}_{eff}	Effective refractive index
ϵ	Permittivity
λ	Wavelength
$\Delta\lambda$	Bandwidth
β	Propagation constant
ϕ	Phase of the EM wave
L	Length (refers to device length, component length)
Γ	Overlap integral coefficient
α	Loss per unit length
κ	coupling coefficient between the modes.

CHAPTER 1

Introduction

Modern world in its technical context has been exponentially growing in optical telecommunication technology for several decades. Fiber optics communication fulfilled the market demand for high speed, high capacity and long-haul data communication with cost-effectiveness and reliability over time [1, 2, 3, 4, 5, 6]. Besides long-haul communication, short-haul rack-to-rack, system-to-system, and chip-to-chip communication have been realized by using stand-alone integrated optoelectronics devices fabricated on substrates like glass, GaAs, InP, LiNbO₃, etc. [7]. However, none of these substrate materials has been found to be suitable for large-scale integrated optical circuit applications. Since the beginning of this millennium, integrated silicon photonics is evolved not only for stand-alone devices but also to overcome electrical interconnect bottle-neck in integrated CMOS electronics to sustain Moor's Law [8, 9, 10, 11]. Researchers are now trying to co-integrate electronics driver circuitry with photonics components using advanced CMOS technology for low-cost and high-speed optical transceiver. Alternatively, integrated photonics chip is fabricated independently using CMOS technology and flip-chip bonded with the electronics IC to accomplish electrical-optical-electrical (E-O-E) conversion [12]. Till date, many individual components and functional circuits have been demonstrated in silicon-on-insulator (SOI) platform using so-called CMOS compatible silicon photonics technology [13, 14, 15]. As fiber Bragg grating played a vital role in developing many products starting from health-care to sensing application to high-speed optical networks [16, 17, 18, 19], integrated optical Bragg gratings in SOI substrate also bears a huge research potential for on-chip optoelectronic applications. This thesis work was intended to investigate various aspects of distributed Bragg reflector (DBR) in SOI for conventional as well as futuristic novel on-chip/off-chip applications. In following three sections, we will discuss thesis motivation, research objective, and organization of the thesis chapters, respectively.

1.1 Motivation

The real motivation behind this thesis work was the state-of-the-art research progress around the globe, industry interests and after all research opportunity in the area of silicon photonics at IIT Madras. We present here first a detail literature review on silicon photonics research highlighting state-of-the-art research progress and then prospects of DBR based devices for various silicon photonics application. Along with huge success in the advancement of CMOS technology, the demand of large data storage and high-speed data routing in the modern electronic world has put a bottleneck in interconnect delay produced by metal interconnects within electronic chips, microprocessors, and devices in order to achieve ultra-high scale integration [20]. Silicon-based optical interconnect on the other hand allows ultra-high bandwidth at ITU frequencies providing solutions for inter- and/or intra-chip routing of the electrical signal via Electrical-Optical-Electrical (E-O-E) conversion.

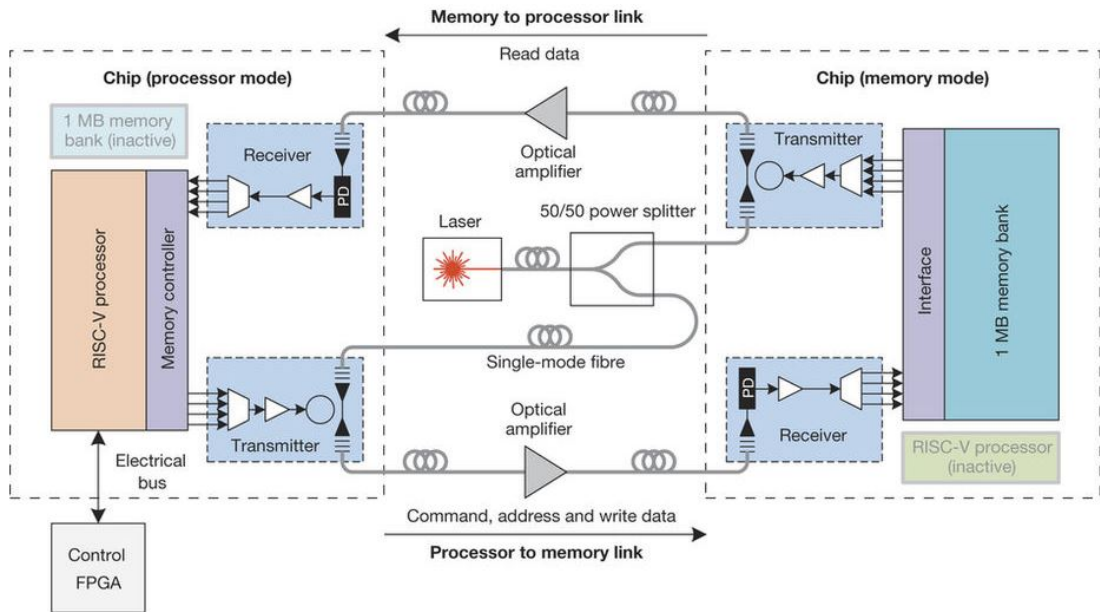


Figure 1.1: Block diagram of the optical memory system demonstrated in 2015 [21].

Many individual integrated optical components or combinations of optical components (small-scale integration) were proposed and implemented using CMOS compatible silicon photonics technology. For instance, the US based first silicon photonics company Luxtera announced the world's first 40 Gigabit Optical Active Cable (OAC) in 2007 [22]. Intel demonstrated their 4x12.5 Gbps condensed wavelength division mul-

timeplexing (CWDM) silicon photonics link using integrated hybrid silicon lasers [23, 24] in 2010. IBM unveiled the holey optochip to transfer information at Terabit per second speed in 2012 [25]. Integrated microprocessor circuits were demonstrated on a single-chip that communicates directly using light (see Fig. 1.1). This represents an excellent example of photonics integrated with electronics using bulk silicon CMOS technology. It is comprised of 850 photonics components for optical interconnect and 70×10^6 transistors for on-chip memory and logic. 2D image data was communicated between two chips via light.

Recently, an ideal silicon photonics chip has been proposed for quantum computers and secured communication [26]. Fig. 1.2 for instance, shows the proposed schematic of CMOS-compatible integrated silicon photonics platform for quantum communication applications. It shows how a single photon could be generated, routed and detected on a single silicon chip. It includes almost all integrated optical components e.g., grating couplers, multimode interference coupler, directional coupler, microring resonator, Mach-Zehnder interferometer, thermo-optic phase-shifter, and of course distributed Bragg reflector.

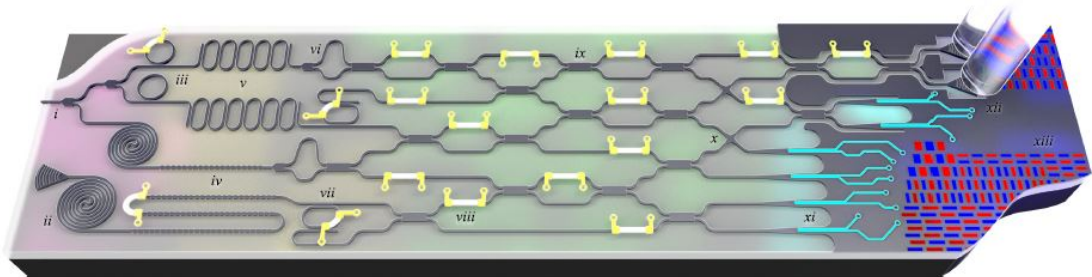


Figure 1.2: A schematic of integrated silicon photonic chip for quantum application. It includes photon sources, pump-removal filters, passive and active optics, single-photon detectors, and control and feedback electronics (moving from left to right on circuit). Besides various devices such as microring resonator, Mach-Zehnder interferometer, thermo-optic phase-shifter, DBR is also proposed for filtering application [26].

The research success of above mentioned integrated silicon photonics chips are obvious because of: (i) optical transparencies of silicon crystal at communication windows ($\lambda \sim 1.3 \mu\text{m}$ and $\sim 1.55 \mu\text{m}$); (ii) availability of high-quality optical-grade SOI wafers [27, 28]; (iii) higher refractive index of silicon allows tighter confinement of optical mode(s) permitting compact devices in the scale of some tens of nanometers [29], (iv)

well established CMOS based planner technology allows integration of different functional group on single chip [27], (v) availability of third order susceptibility allowing it suitable for non-linear optics and/or quantum optic applications [30, 31]. The silicon photonics gains its popularity by not only integrating many optical functional devices in a single chip but also allowing thermo-optic and electro-optic controllability [32, 33], integrability of III-IV and IV-V element group [34], and presence of third-order nonlinearity [31]. With the discovery of electro-optic effect in silicon, active tuning of spectral and spatial characteristics of the photonics devices has become possible, hence opening new horizon of research by setting new possibilities in silicon photonics [32, 35]. The integrability of micro-heater with the optoelectronics devices in silicon provides another degree of freedom which not only facilitate active tuning but also are able to compensate fabrication related unwanted errors in device parameters [33, 21]. The nanoscale interrogation and manipulation using integrated microheater were demonstrated in many research articles as [36, 37]. Also, integrability of III-IV and IV-V element group fuels the (i) on-chip laser fabrication, although it is in its infantry stage of evolution at present and (ii) on-chip photo-detector fabrication, serving as a receiver circuit [34, 38]. Furthermore, the presence of third order nonlinearity in silicon is being utilized in four-wave mixing, Raman spectroscopy and frequency up/down conversions [30, 31]. Many optical functions such as modulation, splitting, multiplexing, de-multiplexing, filtering, switching, sensing etc.[39, 15, 40, 41] have been investigated in silicon-on-insulator (SOI) platform using a variety of integrated optical components such as multi-mode interference coupler (MMIC) [42, 43], directional coupler (DC) [44, 45], Mach-Zehnder interferometer (MZI) [46], microring resonator (MRR) [47], arrayed waveguide grating (AWG) [48], distributed Bragg reflector (DBR) grating [49, 50, 51, 52, 53] etc. The SOI waveguide integrated with DBR of sub-wavelength grating period have broad area of application such as optical modulator [54], add-drop MUX/DEMUX filter, refractive index sensors, spectroscopy, dispersion engineering [55, 56], optical cloaking [57], broad-band grating coupler [58], narrow line-width DBR filters [59, 60], high-Q Fabry-Perot resonator [61], DBR laser [62] etc. For instance, in Fig. 1.2, the component iv. Bragg reflector pump removal filter and (vii) wavelength-division multiplexer (WDM) shown on the chip can be implemented using DBR.

Group velocity and chromatic dispersion can be engineered using a chirped and

an apodized Bragg grating structures. This helps to model active delay line in optical communication [63, 64]. For example, unwanted side lobe ripple reduction and usable bandwidth maximization were demonstrated in SOI in [65]. Sub-wavelength grating (SWG) is the fully etched gratings with a grating period lesser than the Bragg wavelength. It has been used to engineer the effective refractive index of the guiding medium by changing the value of its grating pitch [66, 67, 68]. Using sub-wavelength grating, a large number of waveguide crossings with low loss is shown in [69, 70]. By integrating SWG with micro-ring resonator [71, 72], it was shown that the confinement of light in the waveguide core decreases in SWG ring, hence increasing the sensitivity of the resonator to sense cladding refractive index. Coupling of light from the optical fiber to the integrated silicon waveguides is a great challenge as it suffers coupling loss due to mode mismatch between fiber mode and integrated waveguide mode due to a mismatch in their cross-sectional area. For device characterization purposes at the laboratory level, grating coupler integrated along with waveguide gives better solutions among all other coupling methods. Very high-efficiency grating couplers have been designed and demonstrated by different research groups [73, 74, 75]. Thus a plenty of literature already available demonstrating DBR features for silicon photonics applications. Some of them are briefly reviewed here describing some important device designs and their working principles

Add-Drop Multiplexer

An optical add-drop multiplexer is an important component in the optical communication system. The multiplexer and demultiplexer circuit help to add and drop a wavelength channel carrying data. Integration of DBR with a directional coupler, MZI and MMI help to separate add port, drop port and through port channels. In each case reflected wave is being separated out from the incoming wave via drop port [76, 77, 78, 79, 80]. For instance, Tsao et. al. in 2002 introduced an MMI based OADM in SOI. The corresponding schematic diagram of the wavelength-selectable optical add-drop multiplexer (OADM) in SOI is shown in Fig. 1.3. The DBR is integrated on an MMI coupler and, n-type, p-type poly-Si are integrated along the side of the MMI to provide electron-hole concentration as well temperature. By applying voltages at p and n

contact of $V_p = 0.8$ V and $V_p = -0.8$ V, the wavelength switching of 0.9 nm was shown by FDTD simulation. Thus any channel can be dropped at the Drop Port by applying corresponding voltage. However, the circuit is complex and so many device parameters have to be controlled for implementing as practical application.

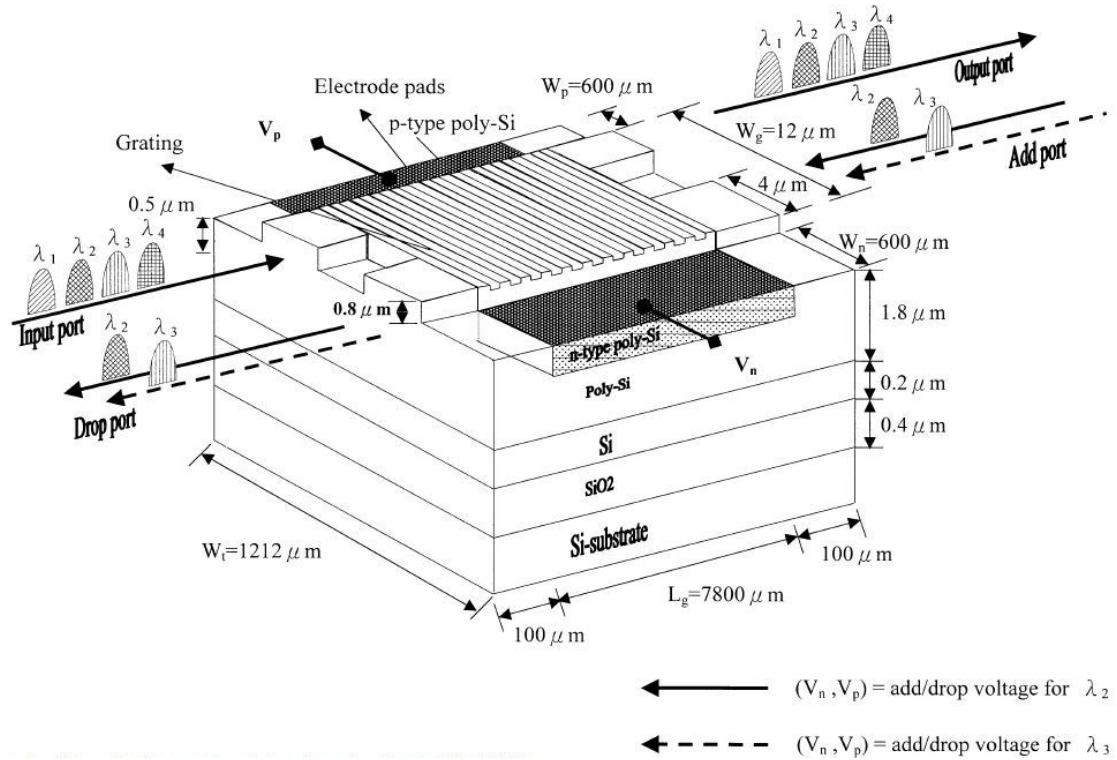
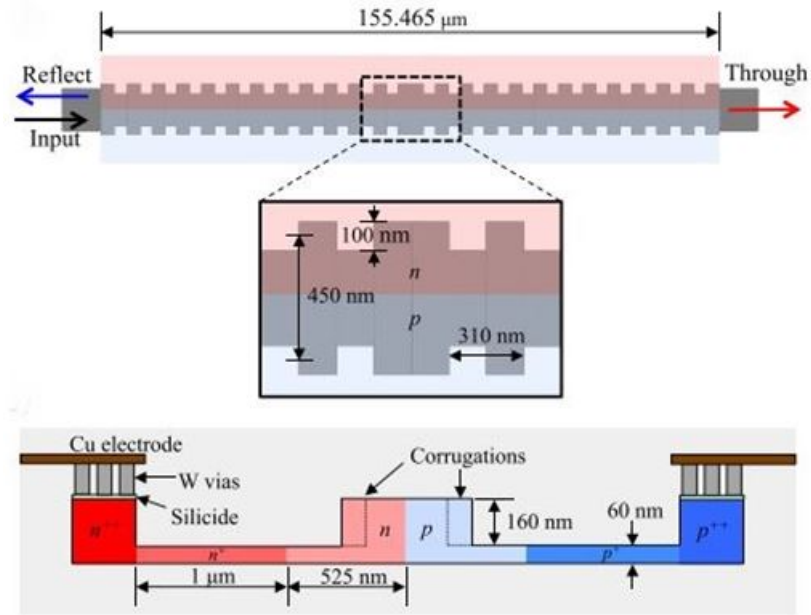


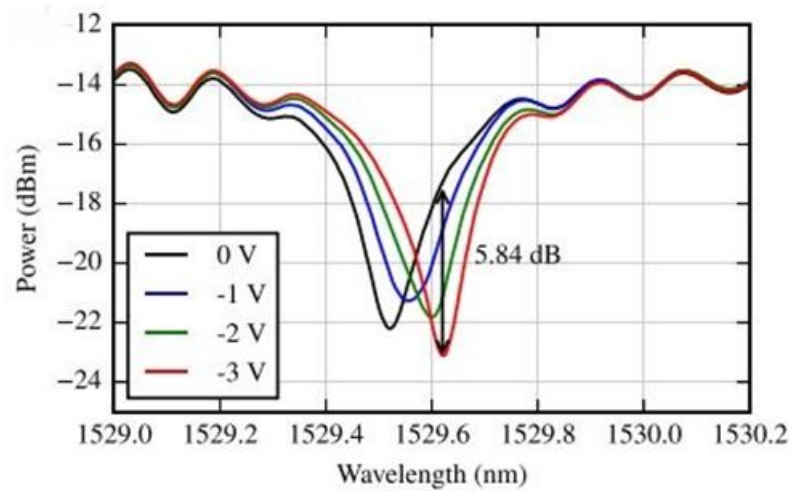
Figure 1.3: Schematic diagram of a proposed wavelength-selectable optical add-drop multiplexer [77].

P-N Junction Modulator

Modulating optical wave with the electrical signal carrying data is an important function to encode electrical data bit into an optical signal. A high-speed optical modulator is in market demand nowadays. Using free carrier plasma dispersion effect by integrating p-n or p-i-n diode across the DBR device and applying an electrical modulating signal, the wavelength characteristic of the DBR devices can be shifted in wavelength. The shift occurred in the Bragg wavelength provides intensity modulation as on-off switching. The extinction ratio, 3 dB optical bandwidth, insertion loss and other properties of the modulator depends upon the device geometry and mode of operations of the p-n/p-i-n diode [82, 81, 83]. For instance, Caverley et.al. in 2015 demonstrated quarter-wave



(a)



(b)

Figure 1.4: (a) The quarter-wave phase-shifted Bragg grating modulator scheme (top) and its cross-section view (bottom); and (b) measured transmission characteristic with various reverse-bias voltages applied to the device [81].

phase-shifted Bragg grating modulator on SOI for the first time. It resulted in the data rate of 32 Gb/s in the open eye diagram. The Schematic of the quarter-wave phase-shifted Bragg grating modulator, including a zoomed-in view of the region near the phase-shift, is shown in Fig. 1.4(a). Sidewall DBR is integrated in 220 nm device layer waveguide. A p-n diode integrated with the BDR with applied voltage provides the wavelength shift in the spectral characteristic. A continuous wave light signal operating

at Bragg wavelength gets its intensity modulated when a negative voltage is applied across the p-n junction. However, there is the need to improve the performance further by achieving higher Q-factor and higher extinction ratio of the DBR cavity resonance as the Q-factor achieved is 6×10^3 which is lower for an efficient modulator.

Flat-Top Bandpass Filter

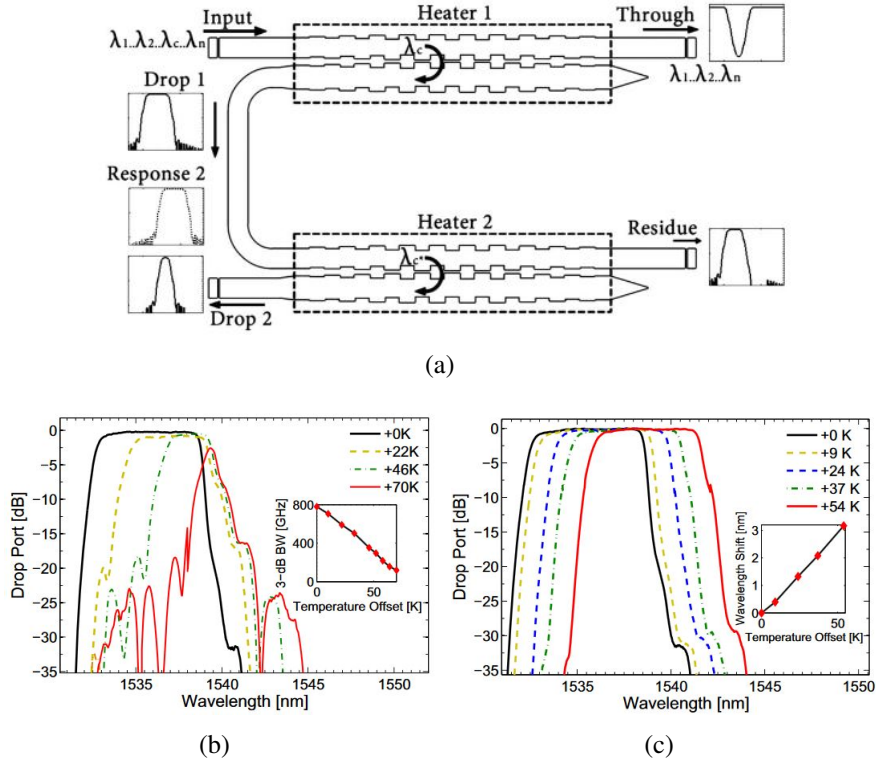


Figure 1.5: (a) Schematic of DBR based broadband filter device. The wavelength reflected at the first contra-directional DBR is reflected again by an identical contra-directional DBR. The metal heaters control both contra-DCs; (b) reflection characteristic of the device for different temperatures applied to only one contra-DC; and (c) spectral response with the heat applied to both contra-DCs [78].

Another application of DBR is as wavelength filter device. The band pass, band reject, low pass high pass, comb and notch filters can be designed using DBR [84, 85, 76, 86, 87, 63, 61, 88]. Different kind of DBR are sub-wavelength grating, phase shifted grating [89], chirped and apodized grating, phase mismatched grating, directional coupler assisted grating, slot waveguide assisted grating, sidewall gratings etc. For instance, St-Yves et. al. in 2015 demonstrated the broadband tunable DBR filter in SOI (see Fig. 1.5). The device spectral characteristic shows the out-of-band contrast as high as 55 dB,

bandwidth tuning of 670 GHz, wavelength tunability with unlimited FSR. Fig. 1.5(a) shows the schematic of a pair of a contra-directional coupler (DC) based DBR filter, both operating at drop port. The temperature tunability of the bandwidth and central wavelength is shown by heating only one contra-DC and both contra-DCs respectively.

High Q Fabry-Perot Resonance Filter

A phase shifted grating is the DBR with a cavity and it works as a Fabry-Perot resonator where DBR acts as the reflecting mirror with very high reflectivity [90]. A conventional uniform Bragg grating shows stopband in transmission spectrum at Bragg wavelength, but using phase shifted DBR, the narrow transmission peak(s) can be obtained in the stopband centered at Bragg wavelength. The narrower bandwidth of the transmission peak makes it suitable for many sensing and communication applications.

Based on cavity length one or many transmission peaks can be observed in the transmission stopband of a DBR. If the cavity length is exactly equal to a quarter wavelength, it resonates at only one wavelength [92, 85, 81, 89]. For instance, Zhi Zou et. al. in 2016 demonstrated the phase shifted grating integrated in SOI strip waveguide (of 60 nm thickness) in a spiral shape to increase the grating length up to 2 mm. Fig. 1.6 shows the corresponding device design and transmission characteristics. Such a long grating length provides very high DBR reflectivity, hence increasing the Q-factor as high as 1×10^5 . The wavelength tunability is also demonstrated by integrating a TiN based microheater on the top of the grating. The device was tuned to work as stopband filter as well by applying suitable power to microheater. However, the spiral bend would introduce loss in the grating and it also increases the device footprint.

Lab-on-Chip Sensor

Compact, high sensitivity, reliable and cost-effective integrated sensor finds wide range of applications as in biomedical science to detect biomolecule (tumor cells or diseased cells), in defense (as for example night detector), in industry (as for example in bridge, transformer etc), in material science, in environment science (to detect pollution level of air, water, gas composition) etc. Integrated DBR in SOI-based sensors because of its

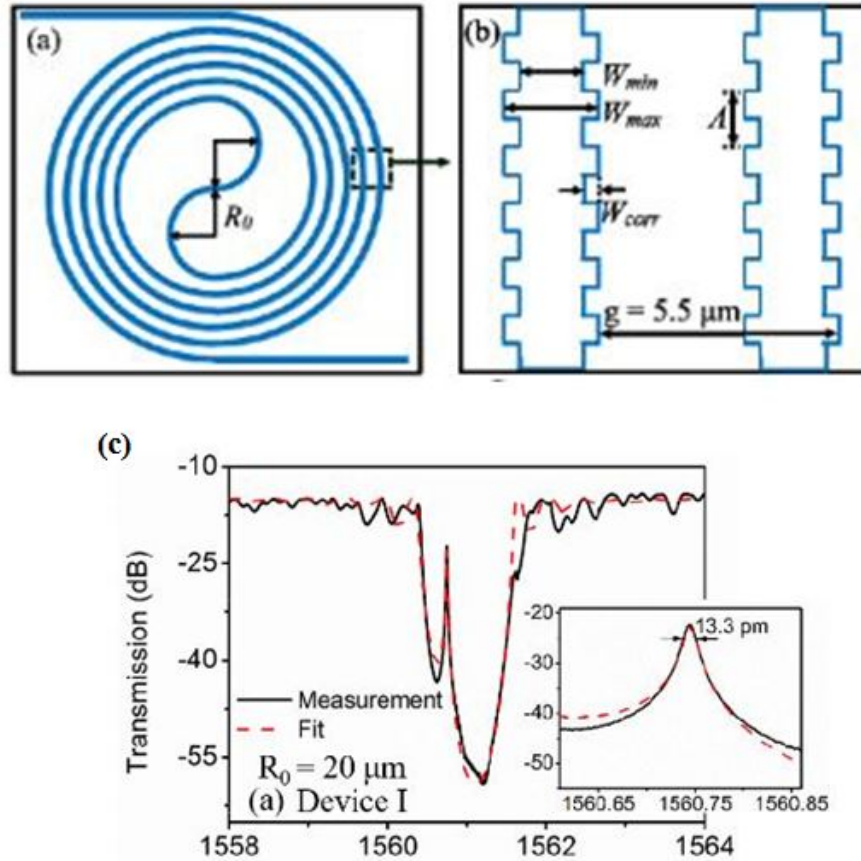
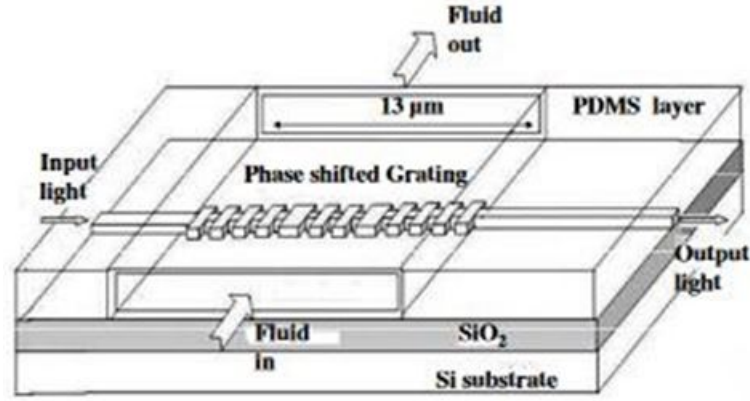
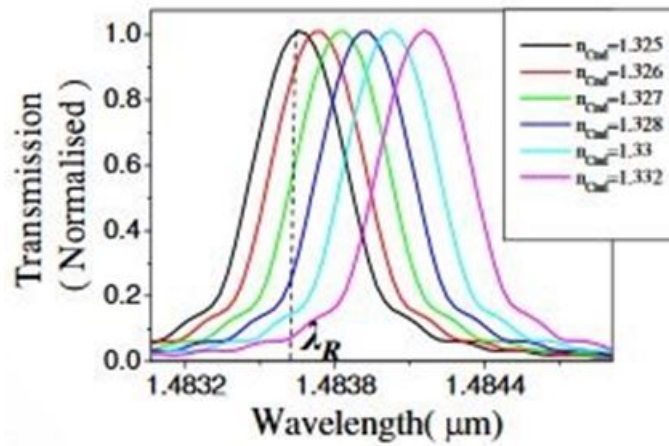


Figure 1.6: (a) Schematic of the spiral DBR with the minimum bending radius of R_0 . (b) grating details shown by zoom-in view. Λ : grating period, W_{corr} : corrugation width, g : waveguide spacing, and (c) Transmission spectra of the device with (a) $R_0 = 20 \mu\text{m}$. The experimental spectra and modeled spectra is shown in solid black lines and the dashed red lines respectively [91].

high Q-factor, high reflectivity, compact size and an active tuning possibility of silicon, become a good choice for various sensing applications. Phase-matched wavelength (or Bragg wavelength) resulting due to periodic structures can be either shift in wavelength and/or its intensity can be modulated by the variation of its surrounding cladding material. The cladding material with different molecular structure, physical and chemical properties like concentration, refractive index etc, hence can be sensed by the use of grating structures [52, 93]. The sensitivity of DBR based sensor can be improved by designing gratings to obtain high Q-factor resonance, high reflectivity at lower waveguide and cavity losses. For example, Prabhathan et. al. in 2009 presented an integrated biosensor based on the phase shifted vertical side wall grating in SOI. Fig. 1.7(a) shows the corresponding schematic diagram of the integrated biosensor. A fluidic channel introduced using the PDMS layer allows the fluid of unknown refractive index to flow over



(a)



(b)

Figure 1.7: (a) The schematic of the integrated biosensor with phase shifted vertical side wall grating, and (b) spectral response of two-phase shifted grating for different channel fluid refractive indices [52].

the grating. As the fluid become top cladding, the waveguide effective index changes. The change in refractive index offers the corresponding shift in wavelength. Thus by properly calibrating the Bragg wavelength shift with respect to a fluid of known refractive index, an unknown fluid can be detected. The detection limit for the refractive index in this example was reported as high as $\sim 5 \times 10^{-5}$. The detection limit can be further improved by increasing the Q-factor of the phase-shifted DBR cavity resonance filter.

Thus from the literature survey, it is evident that integrated optical DBRs can be designed for all most all on-chip silicon photonics applications. Till date, a good number of Ph.D. thesis have been produced investigating different aspects of DBR designs and application in SOI Platform. However, all these DBR designs are integrated in single-

mode SOI waveguides and mostly defined with periodic modulation of waveguide width symmetrically. To our knowledge, DBR structures with asymmetric waveguide width modulation (grating defined in one side-wall) and also DBR structures in multimode waveguides were not given much attention. With the view of this, we outlined a set of research objectives which is discussed in the following section.

1.2 Research Objective

As it is revealed from our literature survey, a variety of novel devices have been demonstrated earlier using DBR structures in SOI substrate for various applications. However, to our knowledge, none of them studied integrated optical DBR structure by asymmetric waveguide width modulation. As we intuitively realized the potential of such DBR grating in a multimode waveguide in terms of spectral features, we set following research objectives to be studied in chronological order:

1. To design and demonstrate integrated optical DBR and DBR cavity with symmetric waveguide width modulation. This is for self-understanding of critical design parameters and to optimize in-house fabrication process parameters.
2. To investigate integrated optical DBR defined by asymmetric waveguide width modulation. The performance of such structure is to be understood first by semi-analytical simulation results and then validated with numerical finite difference time domain (FDTD) simulations. Finally, the demonstration of a filter device with optimized design parameters which could be potentially useful for many aforementioned silicon photonics applications.
3. To explore cascaded DBR structures with asymmetric waveguide width modulations for a resonance-free bandpass filter with higher side-band suppressions.

Feasibility of the intuitive research objectives discussed above can be established by a qualitative discussion. The last two objectives are set to investigate novel and application specific filtering characteristics of integrated optical grating structures in silicon photonics platform. A cartoon representing the wavelength characteristics of the DBR device is shown in Fig. 1.8 to illustrate objective number 2. A wide band of wavelength with flat intensity is being launched in the DBR device integrated with multimode waveguide from the single-mode input waveguide. The fundamental mode,

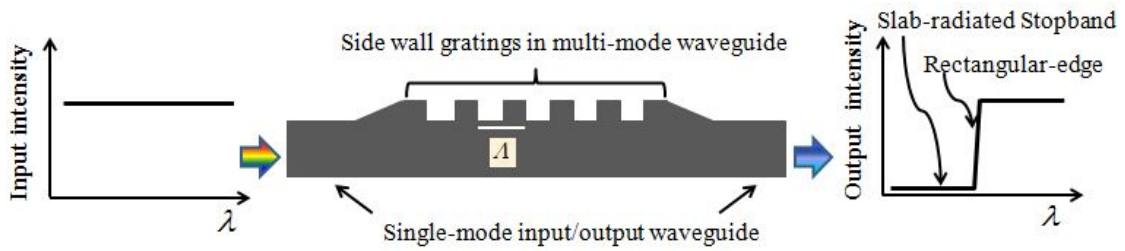


Figure 1.8: A cartoon to represent rectangular edge filter using DBR integrated with a multimode waveguide interfaced with single-mode input/output waveguide (at middle). Input-output wavelength characteristics are also shown (at left/right).

first lower order mode propagating in backward direction couples to forward propagating fundamental mode at two different phase-matched wavelengths in the DBR region. The rectangular-edge results at the lower phase-matched wavelength. Other higher order non-confined slab modes propagating in backward direction also couple to forward propagating fundamental mode at different phase-matched wavelengths in the DBR region. Their stopbands overlap to give flat and approximately zero transmission to the left side of the rectangular-edge filter. Thus, the output transmission characteristic results into rectangular edge filter. To the left side of the rectangular edge is the wide stopband arising due to wavelength radiating to the slab. Thus, in this objective the desired wavelength characteristic should have the following criteria:

1. It should result in a steeper filter edge.
2. It should stop a large band of wavelength without reflecting them back into the source.
3. The larger passband should result in transmission spectrum and,
4. Higher order mode coupled in backward direction should not reach to the source.

A cartoon representing the wavelength characteristics of the cascaded DBR device is shown in Fig. 4.2 to illustrate objective number 3. A wide band of wavelength with flat intensity is being launched in the cascaded DBR device with a different periodicity, integrated with a multimode waveguide. The wider and wavelength-shifted passbands in the transmission of the individual DBR (with period Λ_1 and Λ_2) overlap to result in the relatively narrower delay-free passband. Thus, the output transmission characteristic results into the desired passband filter. Thus, the transmission characteristic of the cascaded DBR structure should have the following criteria:

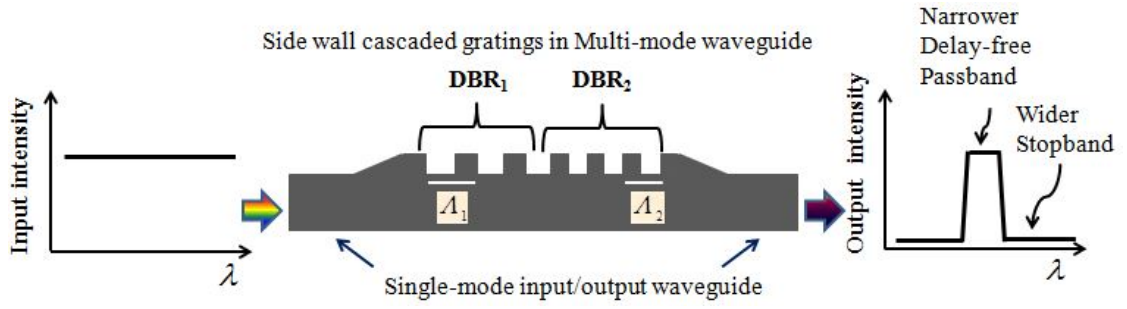


Figure 1.9: A cartoon to represent a cascaded DBR (DBR₁ and DBR₂) of different periodicity (Λ_1 and Λ_2) integrated with a multimode waveguide, and interfaced with single-mode input/output waveguide (at middle). The expected input-output wavelength characteristics are also shown (at left/right).

1. has narrower passband in transmission spectrum
2. has wider stopbands on both sides of the passband in transmission spectrum
3. has high passband to stopband extinction ratio
4. the bandwidth of the passband can be engineered by controlling device parameter.

1.3 Thesis Organization

Within the scope of this thesis work, we have systematically studied based on above-mentioned research objectives. The entire research outcome has been discussed in four chapters; they are discussed here in brief.

In Chapter 2, we have included the SOI waveguide, DBR and quarter phase-shifted DBR cavity by symmetric waveguide width modulation. Waveguide is studied using numerical mode solver for confined mode field distributions and their effective indices to explain single mode and multimode region of the waveguide, wave polarization and waveguide dispersion. DBR and quarter phase-shifted DBR cavity integrated in a single mode waveguide using symmetric sidewall grating have been discussed with the help of phase matching condition, coupled mode theory and transfer matrix method to study its wavelength characteristics. The DBR devices were designed, fabricated and experimentally analyzed for high reflectivity and better Q-factor.

In Chapter 3, we have presented a novel design of a rectangular edge filter (REF) device by integrating asymmetric side-wall DBR in a multimode SOI waveguide. The

theoretical modeling of the device was counter validated with FDTD simulation results. The transmission spectrum of the fabricated device shows the rectangular-edge shaped characteristics with steep edge. Tuning of the spectral characteristics has been presented in the context of heat and cladding index variation.

In chapter 4, the photonic passband is studied by integrating asymmetric side-wall DBR in a multimode SOI waveguide. We mention the limitation of band-pass narrowing in single stage grating which can be overcome by the cascaded grating of two dissimilar periods. Therefore, the cascaded grating and its effect on band-pass narrowing are discussed with design, theoretical analysis followed by fabrication and experimental results in detail.

Finally, in Chapter 5 we have concluded the results by presenting Summary of the entire thesis work and future research scopes.

CHAPTER 2

Waveguide DBR and DBR Cavity

Semiconductor industries have already standardized the specifications of SOI wafers for integrated silicon photonics. The SOI wafer is made up of three-layered materials (see Fig. 2.1). Bottom silicon substrate layer of a typical thickness of $\sim 500 \mu\text{m}$ is to provide mechanical support. The middle buried oxide (BOX) layer of thickness $2 - 3 \mu\text{m}$ is to work as a bottom cladding for the waveguide. The top silicon layer which is also called "device layer" can be chosen depending on the application (typically $\geq 220 \text{ nm}$) and integrability of optical as well as electronic devices in sub-micron dimensions. Fortunately, intrinsic silicon is transparent for communication wavelengths ($\lambda \sim 1.31 \mu\text{m}$ and $1.55 \mu\text{m}$) and beyond as its bandgap $E_g = 1.1 \text{ eV}$. The refractive index of silicon device layer (3.477) is sufficiently large compared to those of cladding silicon di-oxide (1.477) at $\lambda \sim 1550 \text{ nm}$ - enabling smaller core dimension for an optical waveguides.

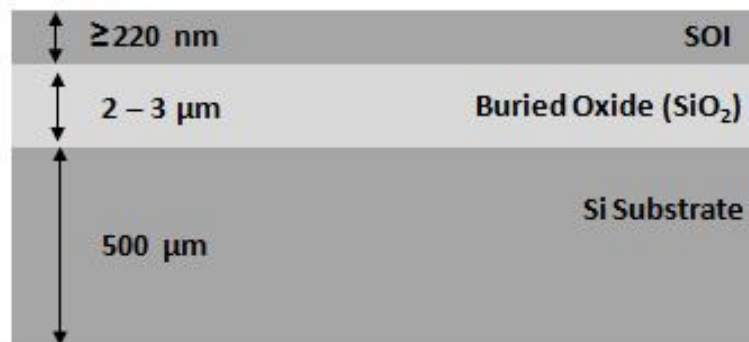


Figure 2.1: A cross sectional view of a SOI wafer.

The most fundamental building block of integrated silicon photonics is the photonic-wire waveguides with submicron dimensions. Silicon waveguide in above mentioned SOI substrate is designed by using commercially available eigen-mode solver. DBR integrated with single-mode waveguide has been investigated using coupled-mode theory. A MATLAB code has been developed to solve the coupled-mode equations for the DBR structures. The final design parameters for the waveguide and grating are opti-

mized by evaluating spectral response. The DBR devices with a set of optimized design parameters were fabricated in-house and characterized for process optimization.

In this chapter, we discuss first the designs of single-mode SOI waveguide, integrated optical DBR by symmetric modulation of waveguide width and a $\frac{\pi}{4}$ phase-shifted cavity. Afterwards, fabrication and process optimization of these devices have been discussed.

2.1 SOI Waveguide Design

Optical waveguides are generally designed in the rib-shaped core rather than cylindrical shape like optical fiber due to ease of fabrication processes, scalability, and integrability with other electronic devices using CMOS compatible planar technology. The 3D schematic of a typical rib or ridge-shaped waveguide in SOI is shown in Fig. 2.2. The design parameters are waveguide width (W), device layer thickness or waveguide core height (H) and slab thickness (h). While the value of W is finite, the value of h can vary from 0 to $\lesssim H$ for a single-mode waveguide design operating at desired wavelength band. A non-zero value of h is preferred for integrating active elements like thermo-optic and/or electro-optic phase-shifter. For our design we also consider non-zero value of h for single-mode guidance in TE polarization ($\lambda \sim 1550$ nm).

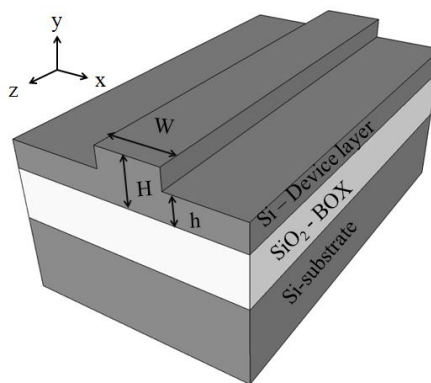


Figure 2.2: 3D schematic of rib waveguide in SOI; cross section of the rib waveguide with parameters: waveguide width W , rib height H and slab height h .

We have studied the polarization dependent and wavelength dependent guidance of above mentioned SOI rib waveguides using Lumerical Mode Solutions [94] for the

device layer thickness of 220 nm and 250 nm. However, the same is studied for larger dimension rib waveguide in Sujith et al. [95], or elsewhere. From numerical simulations one can easily obtain vector field distributions of the guided modes and their respective effective indices as eigen values. Looking into the electric field components of guided mode field solutions we can identify whether it is a TE ($\mathcal{E}_x \gg \mathcal{E}_y$) or TM ($\mathcal{E}_x \ll \mathcal{E}_y$) or hybrid ($\mathcal{E}_x \approx \mathcal{E}_y$) polarized. For our discussion, we have assumed a guided mode is TE polarized if $\frac{\mathcal{E}_x}{\mathcal{E}_x + \mathcal{E}_y} > 50\%$. Generally, we found that the TM mode starts guiding for a deeply etched waveguide or $h \rightarrow 0$.

Fig. 2.3 shows the effective indices as a function of W for guided TE and TM modes using device layer thickness of $H = 250$ nm at wavelength $\lambda = 1550$ nm for different slab height thickness starting from $h = 0$ nm to $h = 130$ nm. It is observable from Fig. 2.3(a) that both the TE and TM mode(s) exist in the fully etched waveguide. It is also observable from Fig. 2.3(b), 2.3(c), 2.3(d) and 2.3(e) that as waveguide slab height increases (or waveguide etch depth reduces) the TM mode(s) (plotted in red colour) are reducing in number. At slab height $h = 130$ nm with device layer thickness of 220 nm and 250 nm, the TM mode become cut-off that no TM mode guide (see Fig. 2.3(f)). For shallow-etched waveguides, the slope of the effective indices with respect to the waveguide width is lesser than that for the deeply-etched waveguide at lower waveguide width region. Thus, the effective indices for the lower value of waveguide width and for the lower value of slab height are more waveguide dimension dependent and any small change in device dimension (W and/or h) due to fabrication error would change the refractive indices and hence the spectral characteristics sufficiently. On the other hand, the effective indices for the higher values of waveguide width and for the higher value of slab height are more relaxed.

The effective indices of the fundamental, first lower order and second lower order TE polarized guided modes have been computed numerically as a function of W and keeping h as the parameter at wavelength $\lambda = 1550$ nm, for $H = 220$ nm and $H = 250$ nm as shown in Fig. 2.4(a) and 2.4(b) respectively. It is evident from the figure that for the waveguide with slab height greater than 130 nm, only TE or TE -like mode(s) exists for the given waveguide dimensions. That is, no TM mode exists within the waveguide for the given waveguide dimensions. In all these plots Fig. 2.3 and Fig. 2.4 the effective

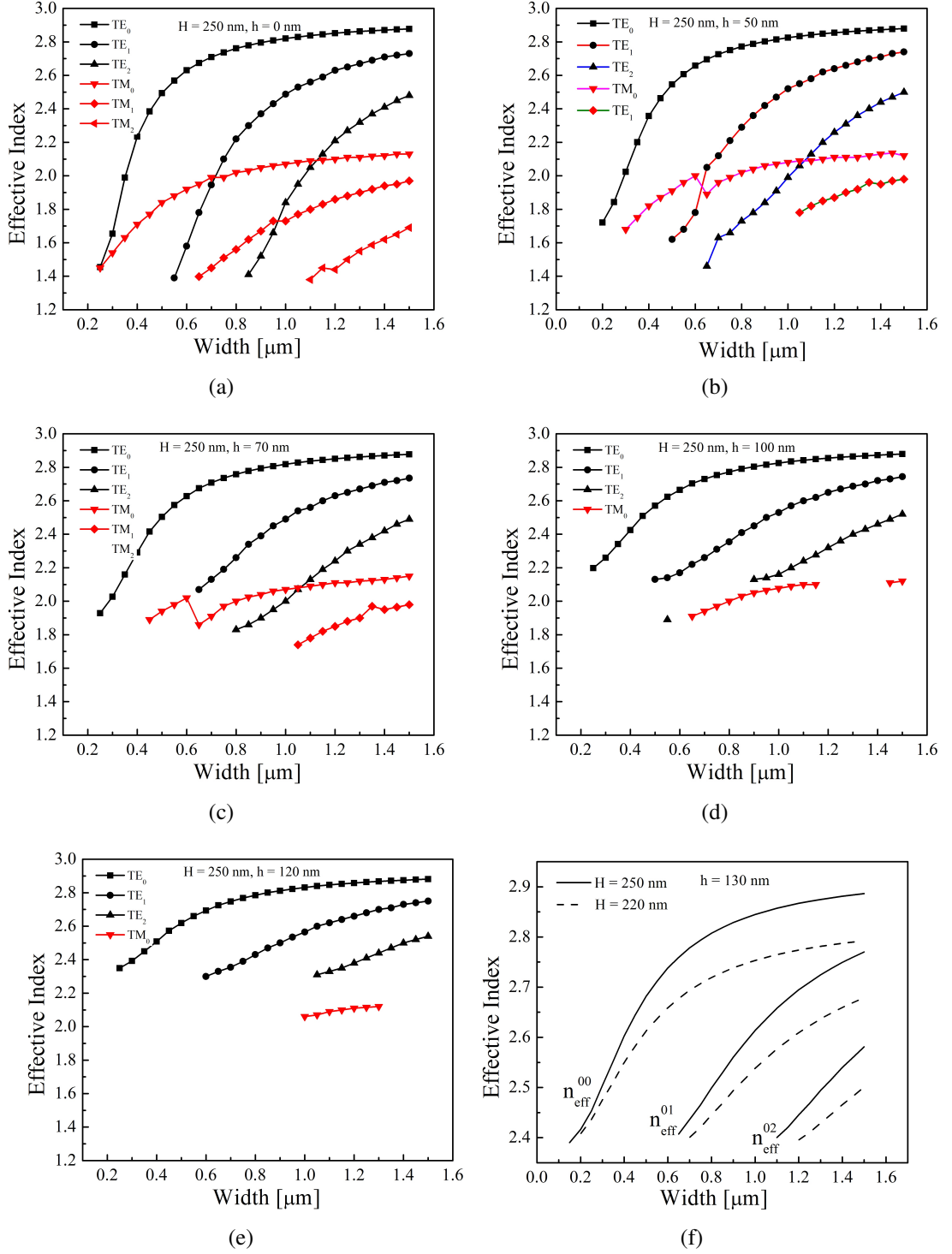


Figure 2.3: Effective indices of various TE and TM guided modes ($\lambda = 1550$ nm) vs waveguide width calculated for device layer thickness or waveguide height $H = 250$ nm with slab heights: (a) $h = 0$ nm, (b) $h = 50$ nm, (c) $h = 70$ nm, (d) $h = 100$ nm and (e) $h = 120$ nm.

indices increases faster as a function of waveguide width for lower values of W and saturates for higher values of W . Cut-off width W_m^{cut} corresponding to a transverse mode

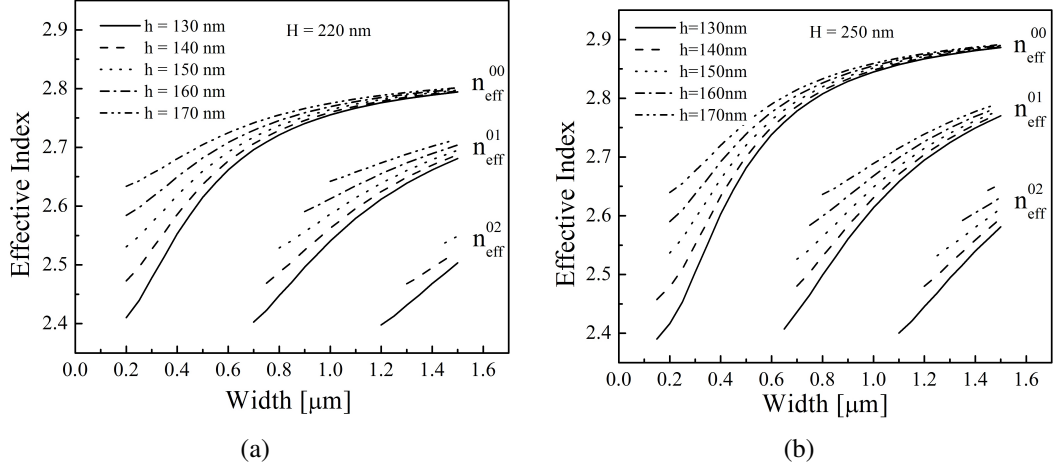


Figure 2.4: Effective indices (n_{eff}^{00} , n_{eff}^{01} and n_{eff}^{02}) of the guided modes vs waveguide width (supporting only TE-like guided modes), calculated for two different device layer thickness and slab height h as a parameter at an operating wavelength $\lambda = 1550$ nm: (a) $H = 220$ nm and (b) $H = 250$ nm, and slab height as parameter.

say TE_{0m} mode (m being the mode order) is defined as the width of the waveguide below which the mode is not allowed to propagate in the waveguide. The mode TE_{0m} becomes evanescent mode for $W < W_m^{cut}$. The cut-off widths for a fixed slab height are more for higher order modes. Fig. 2.5 shows the cut-off waveguide widths (W_m^{cut}) plot versus slab height for first-order and second-order guided modes ($m = 1$ and 2) for two different device layer thickness. The values of $W < W_m^{cut}$ were extracted from Fig. 2.4.

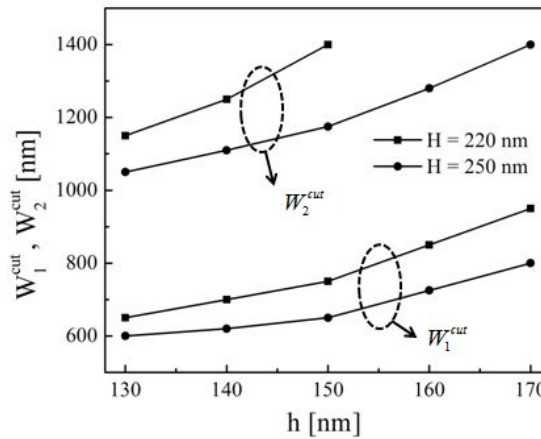


Figure 2.5: Cut-off width for 1st order guided mode (represented by W_1^{cut}) and 2nd order guided mode (represented by W_2^{cut}) as a function of slab heights h calculated for two different values of device layer thickness (220 nm, 250 nm). The results are plotted for TE-like guided modes at $\lambda = 1550$ nm.

Range of waveguide width for confined mode(s) can be extracted for which (i) only TE_{00} mode, (ii) both TE_{00} and TE_{01} modes and (iii) all TE_{00} , TE_{01} and TE_{02} modes will be guiding and the same is being tabulated in table 2.1 for three different slab heights at device layer thickness $H = 250$ nm, which will help to decide any waveguide parameters for certain number of modes to be guiding. From the previous discussions, Table 2.1: Range of waveguide width allowing one, and/or two, and/or three mode(s) confinement at three different slab height calculated at $\lambda = 1550$ nm.

Slab height h [nm]	Waveguide width W [nm]		Existing guided mode(s)		
	$H = 220$ nm	$H = 250$ nm	TE_{00}	TE_{01}	TE_{02}
140	below 680	below 620	✓	x	x
	680 to 1250	620 to 1110	✓	✓	x
	above 1250	above 1110	✓	✓	✓
150	below 740	below to 665	✓	x	x
	740 to 1400	665 to 1175	✓	✓	x
	above 1400	above 1175	✓	✓	✓
160	below 850	below to 725	✓	x	x
	8520 to 1600	725 to 1280	✓	✓	x
	above 1600	above 1280	✓	✓	✓

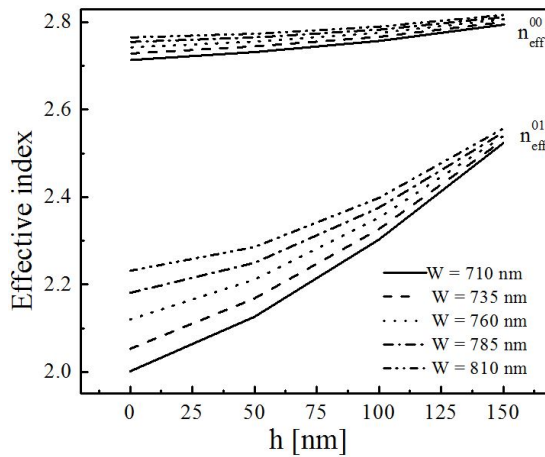


Figure 2.6: Effective indices of the guided modes as a function of waveguide slab height calculated for $H = 250$ nm and waveguide width as parameter at $\lambda = 1550$ nm (supporting only TE-like guided modes).

the deeply-etched and shallow-etched rib waveguide shows the different mode confine-

ment and mode polarization. The idea of change in refractive index upon changing etch depth hence is the key design factor for the rib waveguide geometry. For this, waveguide effective indices of fundamental and first-order guided modes were plotted as slab height as shown in Fig.2.6, waveguide width being the parameter such that only TE mode(s) is guiding. The shallowly-etched condition shows less index difference between fundamental and first-order mode. This property will be utilized in designing narrow passband filter which will be covered in following subsections.

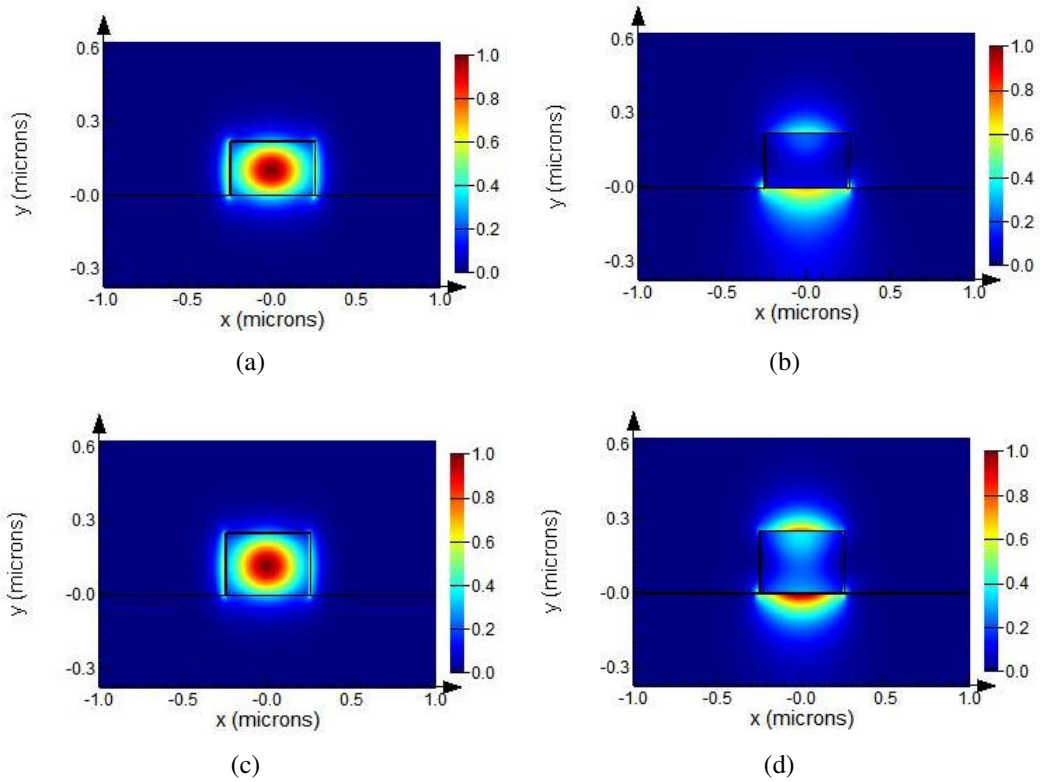


Figure 2.7: The electric field amplitude distribution of guided fundamental modes calculated for $W = 500$ nm, and $h = 0$ nm, at an operating wavelength $\lambda = 1550$ nm: (a) and (b) are dominant component $\mathcal{E}_x(x, y)$ and $\mathcal{E}_y(x, y)$ for the fundamental mode TE_{00} and TM_{00} , respectively calculated for device layer thickness $H = 220$ nm; (c) and (d) are dominant component $\mathcal{E}_x(x, y)$ and $\mathcal{E}_y(x, y)$ for the fundamental mode TE_{00} and TM_{00} , respectively calculated for device layer thickness $H = 250$ nm.

For the fully-etched waveguides, we computed $\mathcal{E}_{0x}(x, y)$ for both the TE_0 and TM_0 modes evaluated for waveguide width $W = 500$ nm, $h = 0$ nm ($\lambda = 1550$ nm) for two device layer thickness (220 nm, 250 nm) using "Lumerical Mode Solver". They are shown in Figs. 2.7.

For a given waveguide parameters $W = 800$ nm, $h = 150$ nm ($\lambda = 1550$ nm) the

dominant mode field components $\mathcal{E}_{0x}(x, y)$ and $\mathcal{E}_{1x}(x, y)$, evaluated for two device layer thickness (220 nm, 250 nm) using "Lumerical Mode Solver" are shown in Figs. 2.8. Modes are tightly confined within the core of the waveguide. The fundamental mode peak electric field lies in the center of the waveguide, while the first lower mode electric field peaks (blue color: negative field amplitude and red color: positive field amplitude) lies towards the edge of the sidewalls of the waveguide.

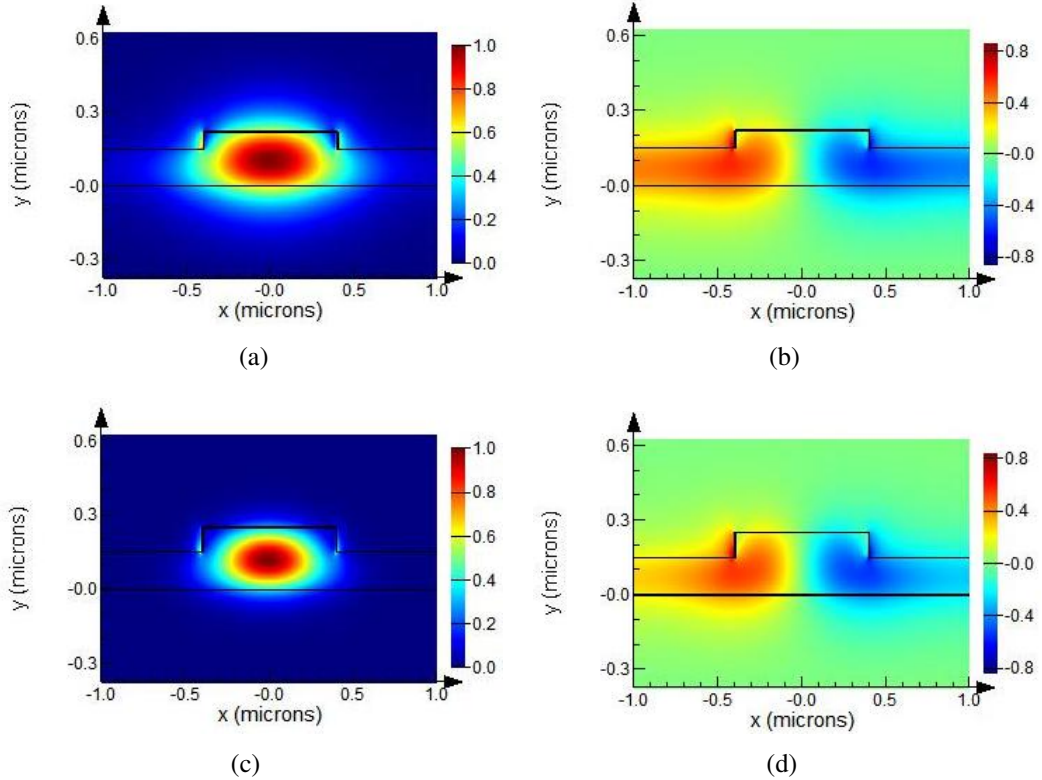


Figure 2.8: The electric field amplitude distribution for the dominant component $\mathcal{E}_x(x, y)$ of guided TE-modes obtained for $W = 760$ nm, and $h = 150$ nm at a operating $\lambda = 1550$ nm: (a) and (b) are TE_{00} and TE_{10} , respectively calculated for device layer thickness $H = 220$ nm; (c) and (d) are TE_{00} and TE_{10} , respectively calculated for device layer thickness $H = 250$ nm.

In optics, dispersion is the phenomenon in which the phase velocity of a wave depends on its frequency. This dependency can be due to material property and device geometry. The dispersion caused due to guided modes as their propagation constant varies is called intra-modal dispersion [96]. But, by designing a single mode waveguide, the intra-modal dispersion can be removed. For silicon, the material dispersion is negligible for the wavelength range $1520 \text{ nm} < \lambda < 1620 \text{ nm}$. However, for simulation of dispersion effect of SOI waveguide the material dispersion is consider by commercial

mode solver "Lumerical MODE Solutions" [94].

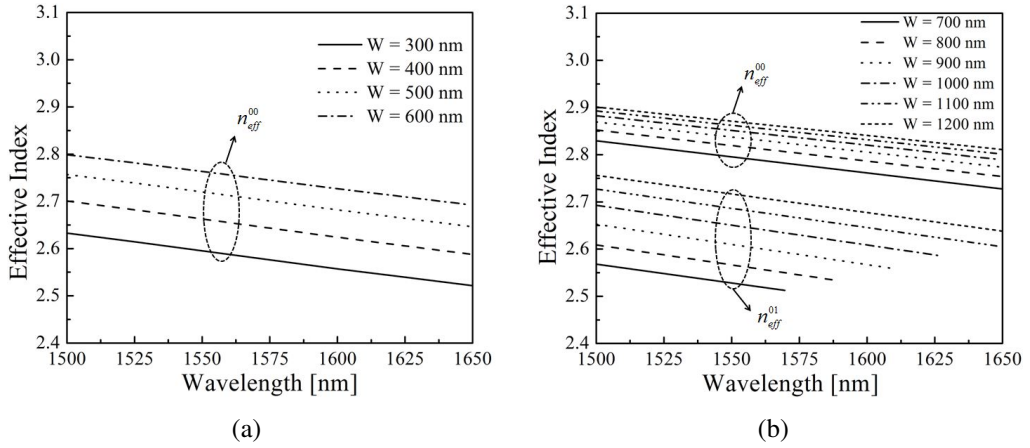


Figure 2.9: Effective indices of the guided modes as a function of operating wavelength, calculated for a device layer thickness of $H = 250$ nm, slab height $h = 150$ nm and waveguide width as parameter (supporting only TE-like guided modes): (a) single-mode regime, and (b) multimode regime (supporting two lower order guided modes).

For the devices having wavelength-dependent characteristics like integrated Bragg grating, ring resonators etc, the study of dispersion become more important. For example, the DBR devices are highly wavelength dependent near Bragg wavelength. Therefore, a study of wavelength dependency of refractive indices will truly account for actual analytical modeling of the device. For that, effective refractive indices varying as the wavelength computed for a waveguide with parameters $H = 250$ nm and $h = 150$ nm, and W as parameter (using Lumerical MODE Solutions) are shown in Fig. 2.9. Fig. 2.9(a) shows the waveguide dispersion characteristic for the single-mode waveguide, while Fig. 2.9(b) shows the waveguide dispersion characteristic for the multimode waveguide having two lower order guided modes. It is evident from Fig. 2.9(b) that the fundamental mode becomes cut-off at a longer wavelength, also the cut-off wavelength $\lambda_{cut-off}$ is longer for larger waveguide width. Thus, one has to be very careful while deciding device dimension for single mode condition operating for wider wavelength range.

2.2 DBR in Single Mode Waveguide

In this section, the performance of a DBR structure designed with symmetric width modulation of a single mode waveguide has been discussed. Such a waveguide DBR structure can be defined along with input/output access waveguides. Since our single mode waveguide design is with shallow etched rib structure (etching depth ~ 100 nm), one can also define input/output fiber optic grating couplers using the same lithography process and subsequent dry etching. The working principle of a grating coupler is also discussed here as it helps to understand the phase matching condition of a DBR structure. A typical waveguide DBR along with input/output fiber optic grating couplers has been shown schematically in Fig. 2.10. For optical characterization, the light is launched into the input grating coupler through input optical fiber while the light is collected from the output grating coupler through output optical fiber. Since the width of the grating coupler waveguide is matched to the mode size of an optical fiber (in order to get increase coupling efficiency), it has been adiabatically tapered down to match the width of the waveguide.

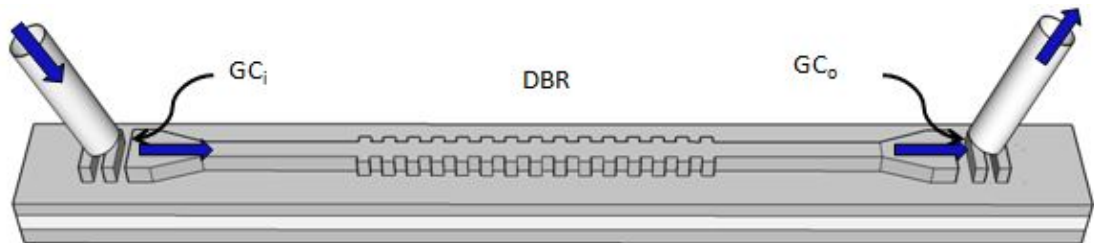


Figure 2.10: 3D schematic of a SOI waveguide integrated with a DBR and input/output grating couplers (GC_i / GC_o).

Periodic perturbations in waveguide DBR (or grating coupler) helps to couple the lightwave from one mode to another mode (or waveguide mode to fiber mode). If the perturbation is small then simple coupled mode theory (with first-order approximation) is good enough for design [51]. Coupled mode theory is the study of coupling between individual unperturbed guided modes existing in guiding structure due to periodic perturbation of dielectric in the guiding medium. An unperturbed wave inside a guided structure propagating along Z -axis can be expressed as the linear sum of guided modes

as (assumed only for dominant electric field component of TE guided modes):

$$E(x, y, z, t) = \sum_k A_k E_k(x, y) e^{-i\beta_k z} \quad (2.1)$$

where A_k and β_k are the constant amplitude and propagation constant corresponding to k_{th} mode respectively. In the presence of perturbation, the amplitude of the mode fields are no more constant but it becomes slowly varying function of z and the total electric field can be written as:

$$E(x, y, z, t) = \sum_m A_k(z) E_k(x, y) e^{-i\beta_k z} \quad (2.2)$$

Using Eq. 2.1 and 2.2 in Maxwell's wave equation for coupling between two modes designated by 1 and 2 (e.g., forward and backward propagating modes in a single mode waveguide). Thus, one can derive the coupled mode equations:

$$\begin{aligned} \frac{d}{dz} A_1 &= -i \frac{\beta_1}{|\beta_1|} \kappa_{12}^m A_1(z) e^{i\Delta\beta z} \\ \frac{d}{dz} A_2 &= -i \frac{\beta_2}{|\beta_2|} \kappa_{21}^m A_2(z) e^{-i\Delta\beta z} \end{aligned} \quad (2.3)$$

where $\Delta\beta$ is given by:

$$\Delta\beta = \beta_1 - \beta_2 - mG \quad (2.4)$$

and κ_{ij}^m is the coupling constant between the guided mode i_{th} to j_{th} , for $i = 1, 2; j = 1, 2$ for m_{th} order grating diffraction. Eq 2.3 can be solved for co-directional and contradi-rectional coupling by applying proper boundary conditions. Maximum coupling occurs between the modes when phase matching condition is fulfilled as $\Delta\beta = 0$, i.e.

$$\beta_1 - \beta_2 - mG = 0 \quad (2.5)$$

for non zero value of the coupling constant κ_{ij}^m . They are discussed in the following subsections.

2.2.1 Phase Matching Conditions

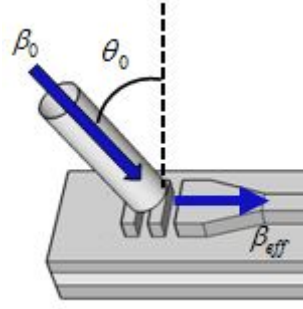
The phase matching condition for a DBR structure in a single mode waveguide can be well understood once we discuss the same between fiber modes and waveguide modes via input/output grating couplers. Coupling the lightwave from an optical fiber to optical interconnect on-chip and vice versa suffers coupling loss due to mode mismatch especially in the end-fire coupling or butt-coupling method. Also in these coupling methods, one needs to prepare well-polished end-facets to reduce loss due to light scattering at the rough interface. Mode-mismatch loss and scattering loss is together known as coupling loss. The coupling efficiency can be increased up to some extent using lensed fiber coupling but increasing extra cost. The desirable features of a fiber to chip coupler system thus are cost-effective, highly efficient and easily integrable. In recent decade many research group addressed the coupling issue and suggested the grating coupler can give higher coupling efficiency, easily accessible and can be integrated with optical interconnects [73, 75, 74]. Nevertheless, it can be integrated with waveguide devices in single step lithography for specific devices as in our proposed device structures.

The schematic to represent the fiber-to-chip light coupling via grating coupler and corresponding vector diagram to illustrate the phase matching condition is shown in Fig. 2.11. Lightwave of free space wavelength λ incidents at an interface formed by two medium *medium*₁ and *medium*₂ having refractive indices n_0 and n_1 respectively with the angle of incident and the angle of transmission θ_0 and θ_1 respectively (see Fig. 2.11(b)). A periodic perturbation along the interface of the medium (along with CO) of period Λ is defined to define grating coupler. Propagation constants or wave vectors in *medium*₁ and *medium*₂ can be written as: $\beta_0 = \frac{2\pi}{\lambda}n_0$ (shown by vector \overrightarrow{AO}) and $\beta_1 = \frac{2\pi}{\lambda}n_1$ (shown by vector \overrightarrow{OB}) respectively. Then from Snell's law (assuming no periodic perturbation):

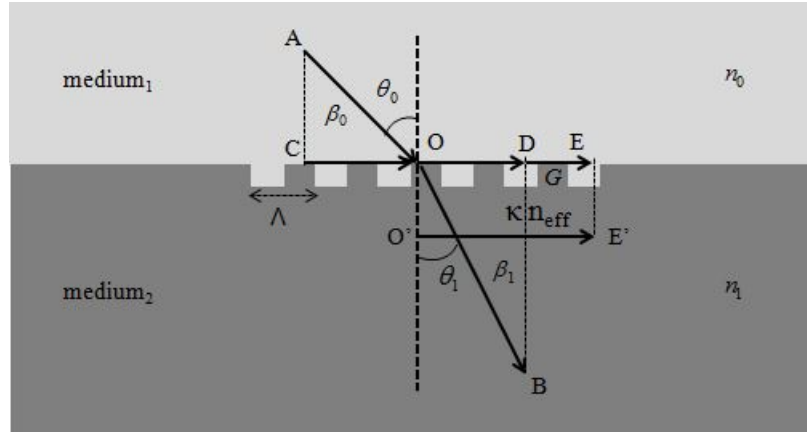
$$n_0 \sin \theta_0 = n_1 \sin \theta_1 \quad (2.6)$$

Defining magnitude of the free space wave vector by $k = \frac{2\pi}{\lambda}$ and multiplying both side of equation Eq. 2.6 with k :

$$\beta_0 \sin \theta_0 = \beta_1 \sin \theta_1 \quad (2.7)$$



(a)



(b)

Figure 2.11: (a) 3D schematic of input Grating coupler and (b) Schematic of input Grating coupler (GC_i) showing wave vectors: incident \vec{AO} , undiffracted transmitted \vec{OB} and diffracted guided \vec{OE} .

Left side term of Eq. 2.7 is equal to CO and right side term of Eq. 2.7 is equal to OD (using simple trigonometric ratios in $\triangle ACO$ and $\triangle BDO$). So, $CO = OD$ reveals that the phase constants along the interface of the two medium must be equal; as CO is the component of the wave vector β_0 in $medium_0$ and OD is the component of the wave vector β_1 in $medium_1$. But the light from space ($medium_0$) will couple to the waveguide ($medium_1$) with grating perturbations when the wavevector component OD (or OC , as $OC = OD$) will be equal to the effective wavevector ($\beta_{eff} = \frac{2\pi}{\lambda}n_{eff}$, n_{eff} is the effective index of the grating coupler waveguide; λ being the free space wavelength) of the waveguide with grating perturbations. Generally, $OD < \beta_{eff}$ for the incident angle θ_0 between 0 to 90° angle. A grating coupler of period Λ , adds or subtracts an integral multiple of grating wavevector ($G = \frac{2\pi}{\Lambda}$) to the incoming tangential component of the undiffracted transmitted wavevector. The resultant m_{th} order diffracted guided

wave vector thus can be given by:

$$\beta_m = \beta_1 \sin \theta_1 + mG \quad (2.8)$$

m being the integers. For in-coupling m is positive as it assists the incoming undiffracted transmitted wave vector; for out-coupling m is negative as it desists the incoming effective transmitted wave vector. Thus, when β_m becomes equal to β_{eff} , it is said that the coupling is due to m_{th} order grating diffraction. So, for coupling is due to first order diffraction it holds that:

$$\beta_{eff} = \beta_1 \sin \theta_1 + G \quad (2.9)$$

By using Eq. 2.7, 2.9 and putting the expression for G and β_{eff} , we obtain:

$$\frac{2\pi}{\lambda} n_{eff} = \frac{2\pi}{\lambda} n_0 \sin \theta_0 + \frac{2\pi}{\Lambda} \quad (2.10)$$

Thus, by denoting grating period Λ_{GCi} for the input grating coupler, it can be found as the function of λ , θ_0 , n_0 and n_{eff} as:

$$\Lambda_{GCi} = \frac{\lambda}{n_{eff} - n_0 \sin \theta_0} \quad (2.11)$$

Similarly, out coupling of the guided lightwave from a waveguide to an optical fiber (kept at angle θ_0 with the vertical line) works can be represented by inverting the direction of each wavevector. It can be easily shown by similar analogy as we discussed above that the period of the output grating coupler can be found as:

$$\Lambda_{GCo} = \Lambda_{GCi} = \frac{\lambda}{n_{eff} - n_0 \sin \theta_0} \quad (2.12)$$

In both of the grating coupler (input/output), width and length of the grating coupler are matched to the dimension of the fiber core which is generally $10 \mu\text{m}$ in diameter in order to increase the efficiency of the grating couplers. Other parameters like θ_0 , Λ_{GCi} , Λ_{GCo} , etch depth of grating can also be optimized for certain waveguide dimension in order to increase efficiency of the grating couplers [50].

The integrated devices including grating couplers, waveguide, and DBR gratings, it is possible to define all with same etch depth such that each component can be fabricated simultaneously in a single step lithography. Since we design the shallow-etched (etched up to ~ 100 nm from top) waveguide with device layer thickness of 250 nm to minimize the loss, grating couplers also have to be etched up to ~ 100 nm. For the convenience of coupling light from the optical fiber to chip or vice versa, the optical fiber is inclined to the vertical axis with an angle $\theta_0 = 10^\circ$. With these values, the period of the input and output grating couplers can be found as ~ 610 nm at the operating wavelength of $\lambda = 1550$ nm which gives the maximum coupling efficiency. Since the input/output grating couplers are integrated with the waveguide and DBR devices, its fabrication and spectral characteristic will be discussed in the experimental result and the discussion section of this chapter.

The DBR serves for wavelength filtering purposes. Its theory can be better understood by wavevector analysis as we did for input-output grating couplers previously. The grating structure would work as a wavelength filter by reflecting the certain band of wavelength centered at Bragg wavelength λ_B corresponding to the wavevector β_{eff} , if the grating vector is equal to twice of β_{eff} in magnitude and opposite to the direction of the incoming wave. Thus:

$$G = -2\beta_{eff} \quad (2.13)$$

Also, the m^{th} order diffracted wave vector β_m can be given from the same Eq.2.8. By putting $\theta_0 = 90^\circ$ (as the forward propagating wave inside the waveguide is 90° to the vertical axis) and observing that $\beta_m = -\beta_{eff}$ (as diffracted wavevector should be reflected) and $m = 1$ (for first order of diffraction), we obtain $G = -2\beta_{eff}$ which is the same equation as Eq. 2.13.

In Fig. 2.12 the geometrical representations of the incoming wave vector, grating vector and reflected wave vector are shown as \vec{AB} , \vec{DE} and \vec{CB} respectively. From law of vector addition, $\vec{DE} = \vec{CA} = \vec{CB} - \vec{AB}$. Putting $\vec{DE} = \vec{G}$, $\vec{CB} = \beta_n$ and $\vec{AB} = \beta_k$

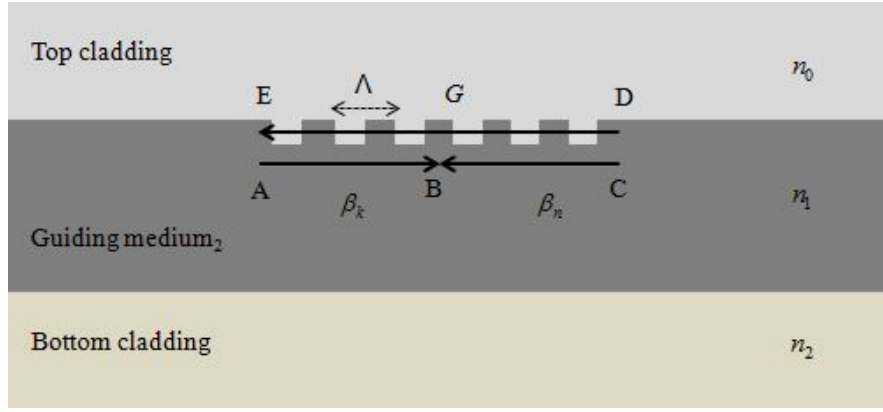


Figure 2.12: Schematic representation of Bragg reflection with wavevector diagram with β_k , β_n and G are the wavevector of k^{th} order forward propagating mode, n^{th} order backward propagating mode and grating wavevector respectively.

such that n^{th} mode is being reflected for k^{th} mode being launched, we obtain:

$$G = \beta_n - \beta_k \quad (2.14)$$

which can be considered as the generalized phase matching equation and is also given by the Bragg's law of diffraction grating. For the DBR grating integrated in a single mode waveguide both the forward propagating as well as the backward propagating mode are fundamental modes only. Thus putting both $n = k = 0$ for fundamental mode in Eq. 2.14, and observing that $\beta_n = -\beta_k$, we obtain

$$G = -2\beta_0 \quad (2.15)$$

where $\beta_0 = \frac{2\pi}{\lambda} n_{eff}^0$ (n_{eff}^0 being the effective index of the fundamental mode). Now, if the grating period of the DBR is Λ , magnitude of the grating vector can be represented as $G = \frac{2\pi}{\Lambda}$ then the phase matched wavelength (also known as Bragg wavelength λ_B) using Eq. 2.15 is given by

$$\lambda_B = 2\Lambda n_{eff}^0 \quad (2.16)$$

2.2.2 Coupling Co-efficient

In a DBR structure, a band of wavelengths around λ_B is back reflected. The peak reflectivity of a DBR at λ_B is defined by coupled mode theory as given in the following equation:

$$R = \tanh^2 \kappa L_g \quad (2.17)$$

Where, κ is the coupling constant as defined by Eq. 2.3 by considering $\kappa_{12} = \kappa_{21} = \kappa$ without any loss of generality in case of a DBR integrated with a single mode waveguide; and L_g is the grating length. The bandwidth or stopband of the DBR structure ($\Delta\lambda_{gap}$) is given by:

$$\Delta\lambda_{gap} = \frac{\kappa\lambda_B^2}{\pi n_{eff}^0(\lambda_B)} \quad (2.18)$$

Thus, both the peak reflectivity and the bandwidth directly depend on the coupling constant κ . Peak reflectivity at λ_B depends on both κ and L_g whereas the stop bandwidth is directly proportional to κ alone. Therefore to achieve high reflectivity and narrow linewidth one should have smaller κ and longer grating length L_g .

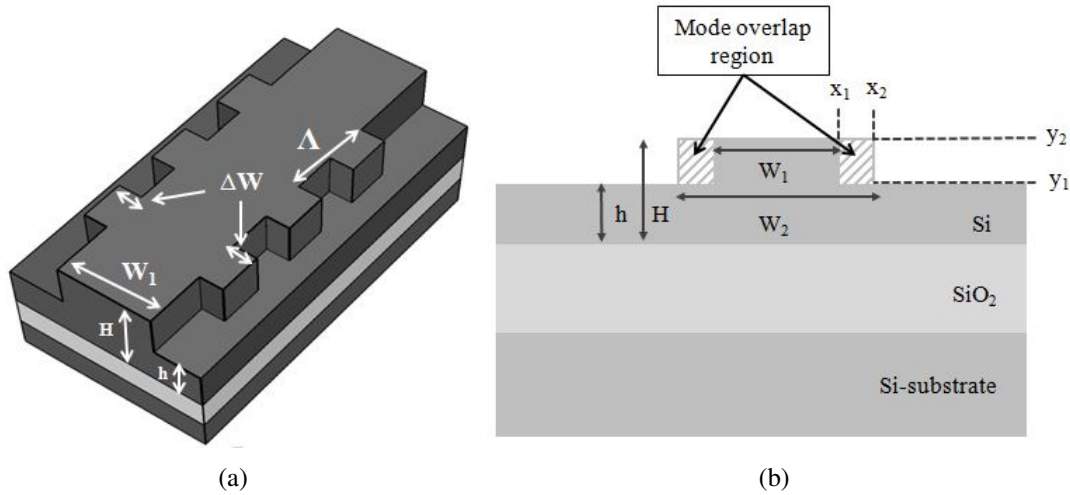


Figure 2.13: (a) 3D scheme of a DBR structure with symmetric waveguide width modulation in SOI along with its design parameters, (b) the corresponding cross-sectional view. The hashed regions indicate the modal overlapping with the grating perturbation.

From the above discussion, it is evident that κ plays a major role in DBR response. For a DBR structure defined by symmetric waveguide width modulation, the value of κ can be calculated numerically. The 3D scheme of symmetric side wall grating in a SOI

rib waveguide is shown in Fig.2.13(a). W_1 and W_2 are the waveguide width without and with grating perturbation respectively. The corresponding cross-sectional view is shown schematically in Fig. 2.13(b). In general, the coupling coefficient between arbitrary m^{th} and n^{th} modes can be obtained directly from coupled mode theory [97] for sinusoidal grating modulation:

$$\kappa_{mn} = 2 \times \frac{n_{si}^2 - n_{air}^2}{\sqrt{n_{eff}^m n_{eff}^n}} \left(\frac{\pi}{\lambda} \right) \int_{x_1}^{x_2} \int_{y_1}^{y_2} \mathcal{E}_m(x, y) \cdot \mathcal{E}_n(x, y) dx dy \quad (2.19)$$

where, the limits of integration for asymmetric side wall grating: (i) $|y_2 - y_1| = H - h$ is the waveguide ridge height and (ii) $|x_2 - x_1| = \Delta W$ is the side-wall modulation width. \mathcal{E}_m and \mathcal{E}_n are the normalized transverse field distributions m_{th} and n_{th} modes, respectively. However, one can find the coupling coefficient due to q^{th} order Fourier coefficient of a rectangular grating by multiplying Eq. 2.19 with q^{th} order Fourier coefficient $1/q\pi$. We consider a single mode waveguide for symmetric DBR integration. For the device layer thickness $H = 220$ nm and 250 nm, the cut-off width for the first order mode is W_1^{cut} (see Fig. 2.5), below which the waveguide will be in single mode region. For the single mode waveguide, the coupling coefficient can be redefined by considering coupling between the two fundamental modes with effect index and the amplitude of electric field distribution n_{eff}^0 and $\mathcal{E}_0(x, y)$ as following:

$$\kappa_{00} = 2 \times \frac{n_{si}^2 - n_{air}^2}{n_{eff}^0} \left(\frac{\pi}{\lambda} \right) \int_{x_1}^{x_2} \int_{y_1}^{y_2} |\mathcal{E}_0(x, y)|^2 dx dy \quad (2.20)$$

For comparing κ_{00} between the DBR device with $H = 220$ nm and 250 nm, the waveguide width (for single mode guidance) were taken as 650 nm which is less than W_1^{cut} for both device layer thickness. Fig. 2.14 shows the κ_{00} versus wavelength plot at two different device layer thickness for two values of ΔW . For smaller ΔW , the evanescent tail of the guided mode for both the device layer thickness (220 nm, 250 nm) remains almost equal resulting into almost equal κ_{00} . The rate of change of κ_{00} with respect to wavelength is in the order of $\sim 1 \times 10^{-5}$ for both the device layer thickness. So the wavelength dependency of the coupling coefficient can be considered negligible within the operating wavelength band of 100 nm (1500 nm $\leq \lambda \leq 1600$ nm).

Fig. 2.15 shows the variation of κ_{00} with respect to grating modulation width $\Delta W =$

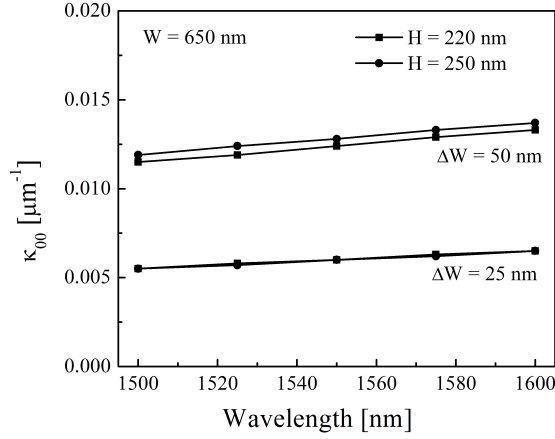


Figure 2.14: Coupling coefficient versus wavelength calculated for single mode waveguide of $W = 650$ nm and $h = 150$ nm for two device layer thickness (220 nm and 250 nm) with ΔW as parameter.

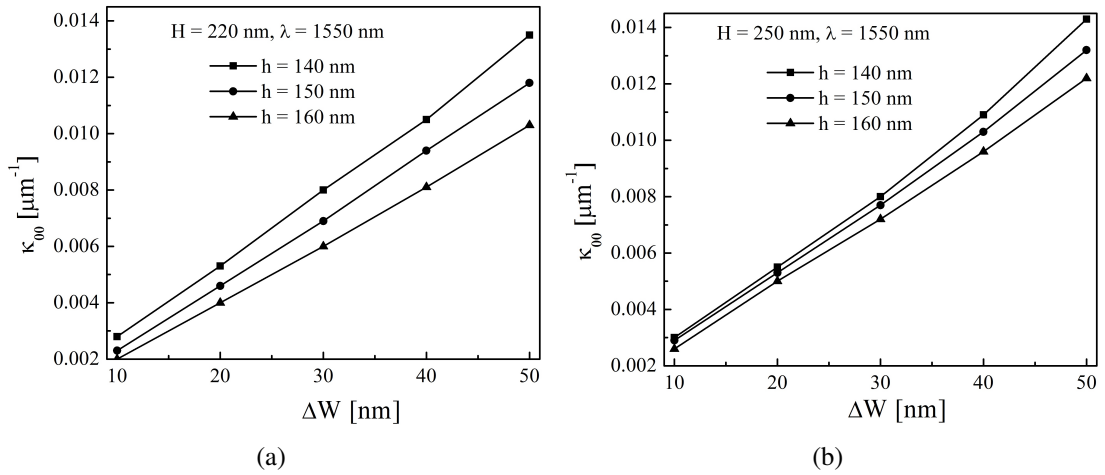


Figure 2.15: Coupling constant versus grating modulation width calculated for single mode waveguide of $W = 650$ nm and h as parameter (a) for $H = 220$ nm, and (b) for $H = 250$ nm. The mode fields were computed at $\lambda = 1550$ nm.

$\frac{1}{2}(W_2 - W_1)$ for two different device layer thickness, $H = 220$ nm and $H = 250$ nm with slab height as parameter calculated at wavelength $\lambda = 1550$ nm using the Eq. 2.19. The normalized transverse field distributions of the fundamental mode (\mathcal{E}_0) was computed for a single mode waveguide of $W = 650$ nm. For coupling constant calculation, the limit x_2 was fixed at the right edge of the width i.e. at 650 nm and the value of limit x_1 was moved from 640 nm to 600 nm in the step of 10 nm. The κ value for $H = 250$ nm is slightly higher than that for $H = 220$ nm. The reason can be explained as a large fraction of a mode is confined near the grating modulation region in case of $H = 250$ nm due to higher core height.

Though we have considered two device layer thicknesses in all the discussions above, now onwards we'll consider only device layer thickness of 250 nm as it was available for experimental demonstration.

2.2.3 DBR: Simulation Results

DBR spectral response can be studied using a couple of analytical equation. These equations are found by solving the coupled mode equations given by Eq. 2.3 for contra-directional coupling at certain boundary conditions. A scheme to represent the DBR transfer characteristic by a transfer matrix is shown in Fig. 2.16. It represents the top view of symmetric side wall DBR in a single mode waveguide. E_{in}^f and E_{in}^b are the forward and backward propagating electric field amplitude at the input of the grating, and E_{out}^f and E_{out}^b are the forward and backward propagating electric field amplitude at the output of the grating. A broad wavelength band of flat intensity light is launched at the input. Due to DBR a band of wavelength centered at phase-matched wavelength (λ_B) is reflected towards input of the DBR while the same wavelength band is absent in the transmitted wave at the output of the DBR. Example of input, reflected and transmitted characteristics are also shown in the figure.

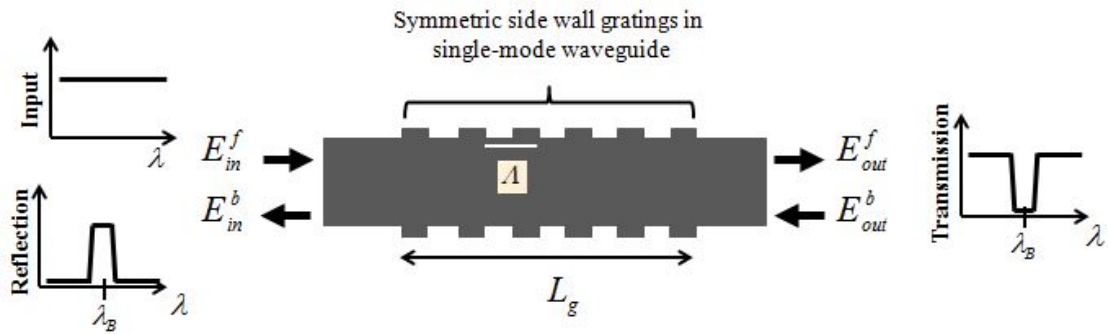


Figure 2.16: Schematic representation of top view of DBR in a single mode waveguide with period Λ and length L_g . E_{in}^f and E_{in}^b are the forward and backward propagating electric field amplitude at the input of the grating, and E_{out}^f and E_{out}^b are the forward and backward propagating electric field amplitude at the output of the grating. Example of input, reflected and transmitted characteristics are also shown.

The electric field amplitude at the output of the DBR (both the forward and backward propagating) are related to the electric field amplitude at the input of the DBR

(both the forward and backward propagating) as:

$$\begin{bmatrix} E_{out}^f \\ E_{out}^b \end{bmatrix} = M \begin{bmatrix} E_{in}^f \\ E_{in}^b \end{bmatrix} \quad (2.21)$$

where, the transfer matrix M is the analytical solution for a uniform grating [51, 90] and is given by:

$$M = \begin{bmatrix} \cosh \Omega L_g - \iota \frac{\Delta\beta/2}{\Omega} \sinh \Omega L_g & -\iota \frac{\kappa}{\Omega} \sinh \Omega L_g \\ \iota \frac{\kappa}{\Omega} \sinh \Omega L_g & \cosh \Omega L_g + \iota \frac{\Delta\beta/2}{\Omega} \sinh \Omega L_g \end{bmatrix} \quad (2.22)$$

where,

$$\Omega = \sqrt{\kappa^2 - (\Delta\beta/2)^2} \quad (2.23)$$

and $\Delta\beta$ is given by Eq. 2.4 for $m = 1$, i.e.

$$\Delta\beta = \frac{4\pi}{\lambda} n_{eff} - \frac{2\pi}{\Lambda} \quad (2.24)$$

The complex effective index n_{eff} is given by:

$$n_{eff} = n_{eff} + i.k \quad (2.25)$$

where k is the imaginary part of the complex effective index accounts for the waveguide propagation loss coefficient (α) as:

$$k = \alpha \frac{\lambda}{40\pi \log(e)} \quad (2.26)$$

Where the α is expressed as dB per unit length of propagation. If the M is represented in its matrix element as:

$$M = \begin{bmatrix} M_{11} & M_{12} \\ M_{21} & M_{22} \end{bmatrix} \quad (2.27)$$

Then, the final transfer matrix as a function of wavelength is represented as:

$$T(\lambda) = \left| M_{11} - \frac{M_{12}M_{21}}{(M_{22})^2} \right| \quad (2.28)$$

We selected the shallowly-etched single mode waveguide using the Fig. 2.4 with smaller grating modulation and longer grating length for a DBR simulation using the transfer matrix method we discussed above.

Single mode waveguide dimension was chosen such for the DBR simulation to obtain Bragg wavelength at $\lambda = 1550$ nm. In order to achieve high grating reflectivity with low waveguide loss the waveguide and grating parameters are chosen for device simulation are as: $\{W, H, h\} = \{560 \text{ nm}, 250 \text{ nm}, 150 \text{ nm}\}$ and $\{\Lambda, \Delta W, L_g\} = \{282 \text{ nm}, 50 \text{ nm}, 500 \mu\text{m}\}$, respectively. The coupling constant corresponding to ΔW value of 50 nm using Fig. 2.15 is $0.0132 \mu\text{m}$. A typical waveguide loss of 3 dB/cm is introduced in the MATLAB code (because we observed the average waveguide propagation loss for the photonic wire waveguide is ~ 3 dB/cm). With these parameters, the transfer matrix was implemented using a MATLAB code to generate the transmission and reflection characteristics of the DBR with the help of Eq. 2.28. The resultant transmission and reflection characteristics are shown in Fig. 2.17. Very high reflectivity ($>$

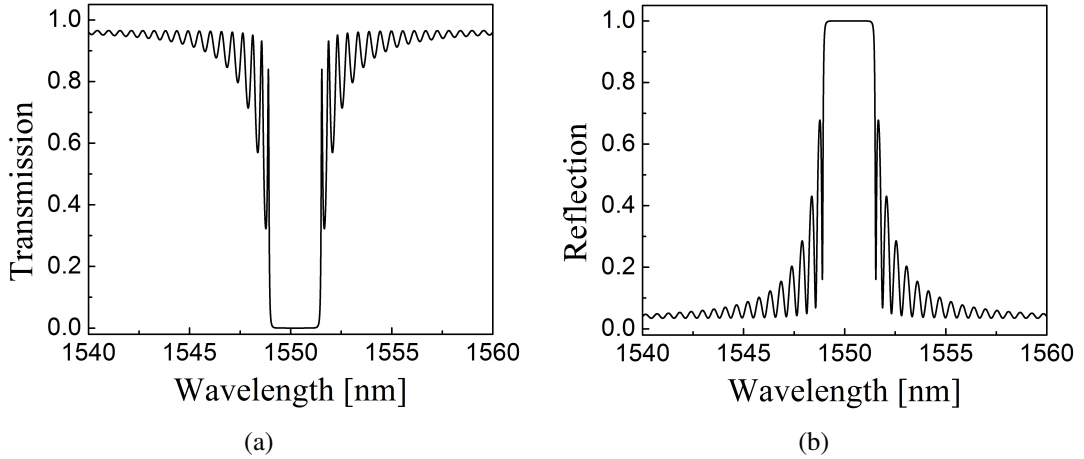


Figure 2.17: (a) Transmission and (b) reflection spectrum of the DBR grating integrated in single mode SOI waveguide with W , H , h as 560 nm, 250 nm, 150 nm, respectively and Λ , ΔW , L_g as 282 nm, 50 nm, $500 \mu\text{m}$, respectively. It is plotted using transfer matrix method for DBR.

99 %) is observed. The highest reflectivity occurs at the Bragg's wavelength $\lambda_B \sim 1550$

nm. The 3 dB bandwidth for both the transmission and reflection spectrum is about 7 nm.

The wavelength characteristic of the grating has been engineered in many ways in the literature. Some of the demanding features of the grating characteristic based on the variety of applications are narrower or broader passband, wider stopband, side lobe intensity reduction, comb generation etc. In the following section, we have studied the narrow passband filter using phase-shifted grating.

2.2.4 $\lambda/4$ Phase-Shifted DBR Cavity

Integrated gratings with $\lambda/4$ phase-shifted cavity in Silicon-On-Insulator based single mode waveguide has been demonstrated experimentally. A resonance peak of 20 pm (3 dB bandwidth) with a quality factor $\sim 8 \times 10^4$ was achieved with the longer grating length of a sub-micron period, shallowly etched rib waveguide.

Integrated DBR grating has been studied earlier for implementing various optical functions such as filtering, modulating, de-multiplexing and sensing optical signals for its large FSR, precise phase and amplitude response and small footprint in comparison to other photonic devices such as ring resonator and arrayed waveguide [81, 77]. Applications such as optical wavelength switching and sensing is implemented using $\frac{\lambda}{4}$ phase shifted DBR cavity [81, 91, 52]. So far reported Q-factor of Fabry-Perot DBR cavities are 2.6×10^3 [92], 1.3×10^4 [52] with compact footprint. Zou et. al. [91] have reported Q-factor as high as 1×10^5 but at the cost of larger footprint due to spiral Bragg grating structure. Also, the bend loss is introduced in the waveguide due to the spiral structure. Q-factor generally degrades due to (i) low mirror reflectivity, (ii) high loss at reflecting surfaces and (iii) small volume cavity. Unfortunately, $\frac{\lambda}{4}$ phase shifted cavity length in the sub-micron period grating is in nanometer dimension which prohibits it to become high volume cavity. However, high Q-factor in such cavity devices can be achieved by fabricating low loss DBR with high reflectivity. Shallowly etched waveguide with small grating modulation fabricated using e-beam lithography helps reducing loss, while longer grating length would help increasing reflectivity [98].

In this chapter, we demonstrate a high-quality factor integrated optical $\frac{\lambda}{4}$ phase shifted

cavity in silicon-on-insulator (SOI). The 3D scheme of the proposed device is shown in Fig. 2.18. It comprises of a rib waveguide having a width W_1 , sidewall gratings of

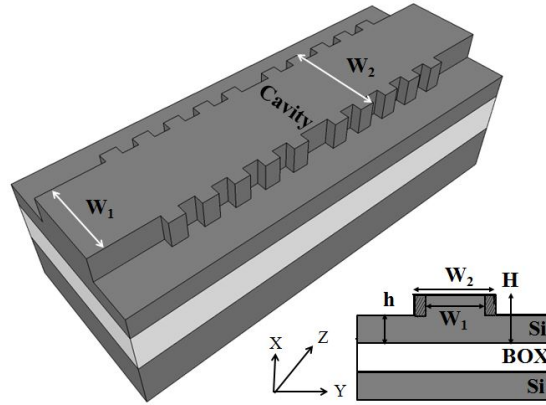


Figure 2.18: (a) 3D schematic of device with $\lambda/4$ phase-shifted cavity. In cross sectional view, W_1 , W_2 , H , h are waveguide width in input output, waveguide width at grating region, core height and slab height respectively.

modulation width $\frac{1}{2}(W_2 - W_1)$ at each side wall of the waveguide, and a quarter wave cavity at half the distance of grating length. The cross-sectional view of the device (see Fig. 2.18 lower right corner) shows silicon at the top and bottom layers and buried oxide (BOX) at the middle layer. The waveguide width W_1 , W_2 , slab height h and core height H are selected such as it allows single mode (transverse electric only) confinement in the waveguide and grating sections at the wavelength ranging from 1550 nm to 1650 nm. For a $\frac{\lambda}{4}$ phase shifted DBR cavity with single mode waveguide, the resonance will occur exactly at the Bragg wavelength, i.e., $\lambda_r = \lambda_B = 2\Lambda n_{eff}^0$ due to Fabry-Perot resonance. The DBR cavity works as a resonance medium and the DBR behave as reflecting mirror with very high reflectivity.

The DBR cavity (of cavity length L_c and grating length L_g each side of the cavity) can be modeled using the transfer matrix by multiplying the three transfer matrices as M (for the DBR in left side of cavity), G (for cavity) and M (for the DBR in right side of cavity) as:

$$M_{cavity} = MGM \quad (2.29)$$

where, M is given by Eq. 2.22 and G is the transfer matrix for the cavity and is defined

as:

$$G = \begin{bmatrix} \gamma & 0 \\ 0 & \gamma^{-1} \end{bmatrix} \quad (2.30)$$

where, γ accounts for the phase introduced by the cavity and is given by:

$$\gamma = \exp(i \frac{2\pi}{\lambda} n_{eff}(\lambda) L_c) \quad (2.31)$$

If the M_{cavity} is represented in its matrix element as

$$M_{cavity} = \begin{bmatrix} M_{c-11} & M_{c-12} \\ M_{c-21} & M_{c-22} \end{bmatrix} \quad (2.32)$$

then, the final transfer function varying as a function of wavelength is represented as:

$$T(\lambda) = |M_{c-11} - \frac{M_{c-12}M_{c-21}}{M_{c-22}^2}| \quad (2.33)$$

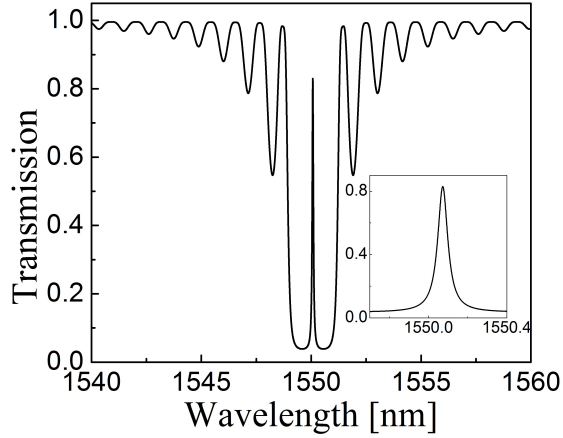


Figure 2.19: Transmission spectrum of a DBR cavity with symmetric side-wall grating integrated in a single mode SOI waveguide with W , H , h as 560 nm, 250 nm, 150 nm, respectively and Λ , ΔW , L_g as 282 nm, 50 nm, 250 μm at each side of a BGR cavity of length 141 nm, respectively. It is plotted using transfer matrix method for DBR cavity. (inset: the enlarged view of the resonance peak at $\lambda_r \sim 1550$ nm).

For theoretical demonstration, the DBR cavity device was studied with transfer matrix method using the same parameters as we used for DBR simulation and with the

help of Eq. 2.33 except for the grating cavity of length 141 nm (= 1/2 of the Λ). The grating length, each side of the cavity was taken as 250 μm . The transmission spectrum of the DBR cavity is shown in Fig. 2.19. The inset figure shows the enlarged view of resonance peak with an estimated Q-value of $\sim 10^5$ at $\lambda_r \sim 1550$ nm.

2.3 Experimental Results and Discussion

The optical grade SOI substrate with a device layer thickness of 250 nm, buried oxide layer thickness of 3 μm , and handle wafer thickness of 500 μm was chosen for fabrication of the waveguide, grating coupler, DBR grating and DBR grating cavity devices. 12 $\mu\text{m} \times 12 \mu\text{m}$ grating coupler with period $\Lambda_{GCi} = \Lambda_{GCo} = 610$ nm were integrated at both the end of a 5-mm-long single-mode rib waveguides ($W = 560$ nm, $H = 250$ nm, and $h = 150$ nm). The DBR grating and DBR grating cavity are defined in the middle of the waveguide with grating period $\Lambda = 290$ nm, grating modulation width $\Delta W = 50$ nm at both of the side walls of the single mode waveguide. The value of the grating length L_g for a conventional DBR was considered as 500 μm , while that for a phase-shifted DBR cavity was considered as 250 μm at each side of the cavity. The cavity length was considered as half the value of grating period, i.e. 145 nm.

Fig. 2.20 shows the schematic representation of device fabrication process steps in a SOI waveguide. The sample for device fabrication was cleaved out of a SOI wafer in the size of $\sim 2 \text{ cm} \times 2 \text{ cm}$. Then the sample was cleaned to remove any trace of organic or inorganic impurities. The processes and corresponding parameters for wafer cleaning are given in the Table 2.2. The schematic of cleaned sample ready to start device patterning is shown in Fig. 2.20 (a). The mask for the DBR, DBR cavity

Table 2.2: Wafer cleaning

Processes	Parameters
Boiling in TCE	2 min at $\sim 50^\circ \text{C}$
Boiling in Acetone	2 min at $\sim 50^\circ \text{C}$ followed by ringe in DI water
Piranha dip	15 \sim 18 min in $H_2SO_4 : H_2O_2 :: 1:3$ (till bubbles vanish)
HF dip	30 sec in HF:DI water::1:10

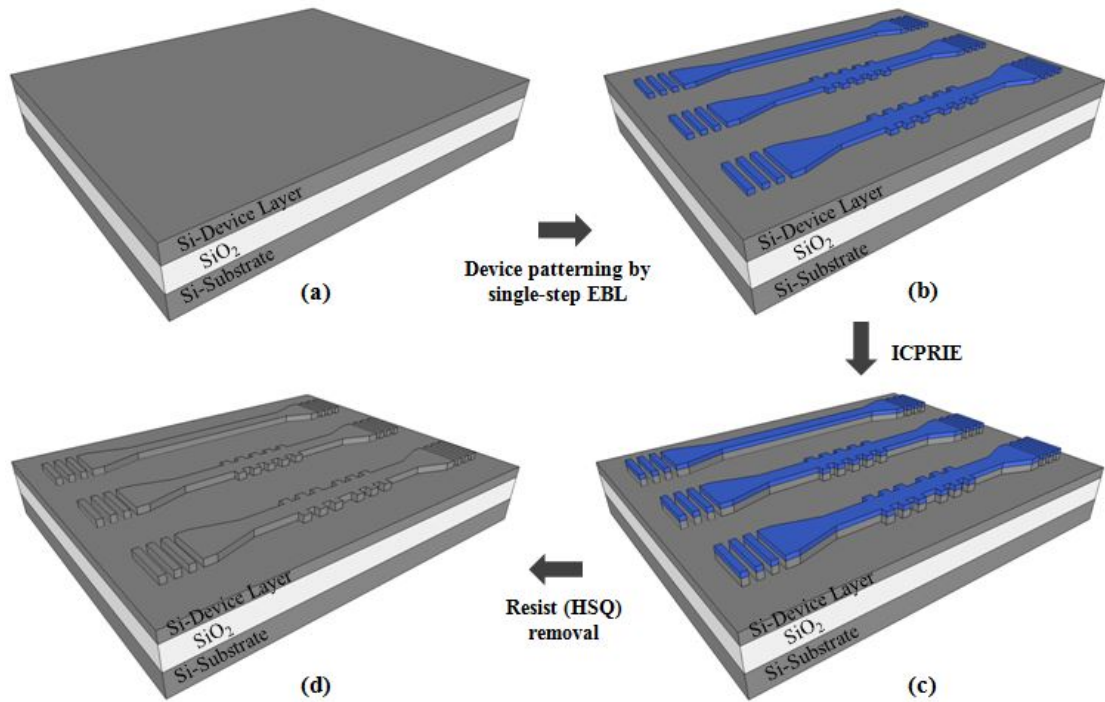


Figure 2.20: Schematic of 3D wafer containing waveguide, DBR grating and DBR grating cavity with input/output grating coupler at each step of fabrication process flow: (a) Starting SOI wafer, (b) HSQ masked wafer (mask is shown in blue colour), (c) Etched wafer using ICPRIE system (with HSQ mask covering top surface of devices) and (d) Final wafer with devices; arrow direction shows the intermediate process between the two connecting wafer stages.

and straight waveguide were patterned with input/output grating coupler with negative tone resist HSQ using e-beam lithography. The patterned mask was dry etched using ICPRIE system. Finally the remaining HSQ from the masked region was removed from the sample to obtain the final fabricated device.

2.3.1 Mask Layout

The mask of the waveguide, grating coupler, DBR grating and DBR grating cavity devices were designed using Raith NANOSUITE software to create GDS-II file. The GDS-II file was loaded to "Raith 152 Direct Write" software which controls electron beam patterning system as well as gives scanning electron microscope (SEM) imaging system. The layout of the mask geometry of DBR and waveguide is shown in Fig. 2.21(a). The design area is $5.5 \text{ mm} \times 2.5 \text{ mm}$ (the figure is not to scale). The labels

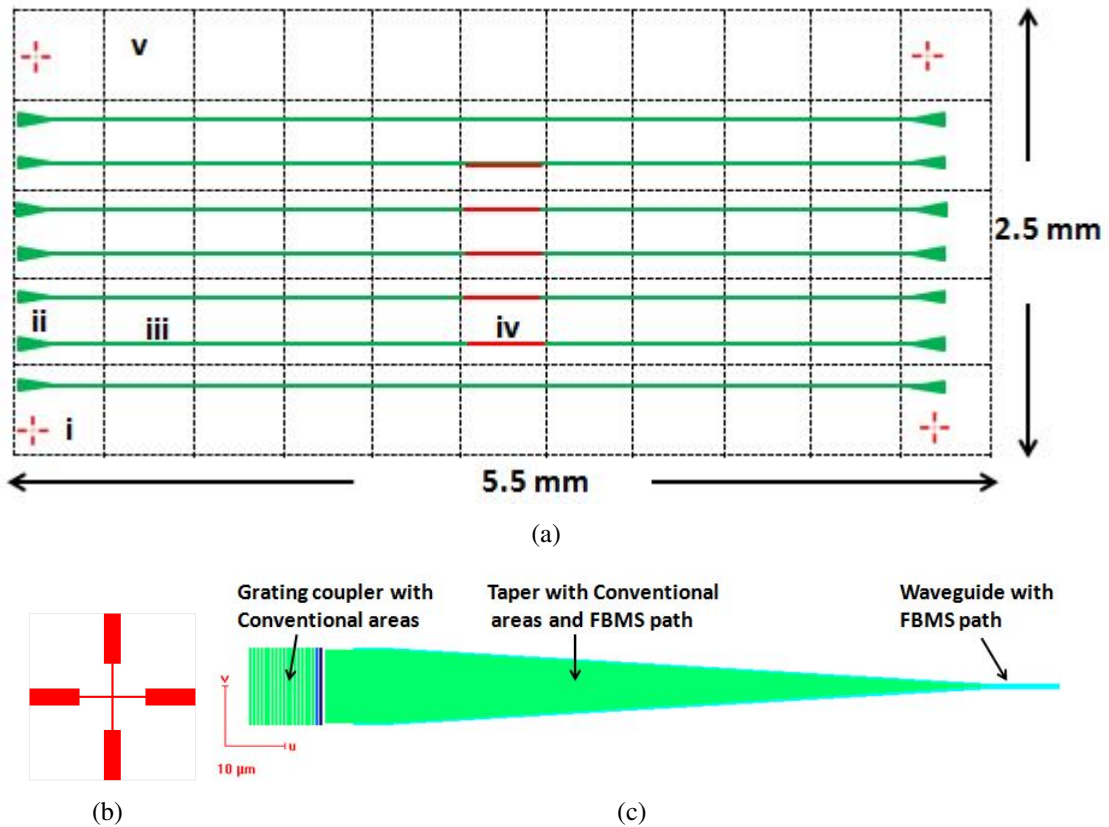


Figure 2.21: Mask layout (designed using Raith NANOSUITE) of (a) DBR devices, labels indicate i. alignment marker, ii. grating coupler, iii. FBMS path as waveguide, iv. DBR and v. write field shown by dotted square; (b) alignment marker and (c) taper connecting grating coupler to waveguide, conventional arms, and FBMS path are shown by arrow.

in the Roman letter indicate i. alignment marker, ii. grating coupler, iii. FBMS path as waveguide, iv. DBR and v. write field shown by dotted square. There are five DBR devices integrated with a waveguide, two straight waveguides with grating coupler connected at input/output of the waveguide, and two alignment markers. Alignment markers are required to carry out next step lithography for alignment purpose. The enlarged view of the alignment marker is shown in Fig. 2.21(b). The cross-hair structure of the alignment marker helps fine alignment to the other mask but with the same alignment marker. Each waveguide is accessed by the input/output grating coupler to facilitate experimental measurement. Grating coupler dimension matches to that of an optical fiber. Thus the grating coupler is tapered down up to ~ 660 nm in the mask. Fig. 2.21(c) shows the magnified view of the mask layout of the grating coupler with conventional areas, the taper section with a conventional area as well as with FBMS path and the waveguide with conventional areas.

2.3.2 Stitch Field Error Correction

Stitch field error is the unwanted error caused by stitching two patterned structures. In electron beam lithography, a larger conventional area is patterned by writing small areas which are defined by the write field of lithography and then by stitching all of them together. If the write field of the patterning system passes through the conventional geometry in the mask layout, it creates stitch field error. For example, Fig. 2.22(a) shows the stitch field passing through the conventional periodic rectangular-shaped geometry of DBR mask (in red color). The green color geometry shows the FBMS path which

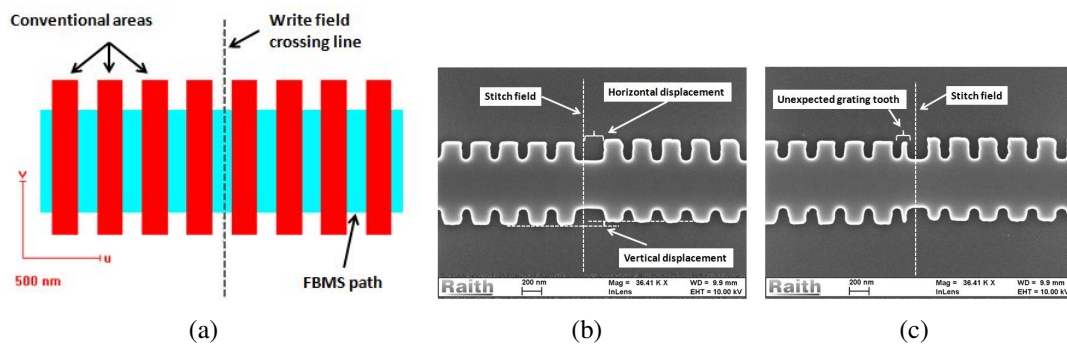


Figure 2.22: (a) Mask layout of DBR with conventional areas, waveguide with FBMS path and write field crossing line, (b) SEM images of DBR device showing stitch field error (horizontal and vertical displacement) at write field crossing line, and (c) SEM images of DBR device showing stitch field induced unwanted grating tooth at write field crossing line.

is stitch free. Once we pattern such a mask, the stitch field error is being reflected as the unwanted shift in both the vertical and horizontal direction. Fig. 2.22(b) shows the SEM image of the patterned SOI sample with the mask layout as shown in Fig. 2.22(a). The horizontal and vertical shifts between the left and right DBR is observable. This is undesirable as the cavity between the DBR device can excite the unwanted Fabry-Perot resonance. The nature of the write field error is observed to be random. The same write field error is reflected in Fig. 2.22(c) as the unwanted grating tooth of a very small pitch. The stitch field error can be mitigated by either selecting FBMS path for longer length waveguide or by selecting the size of the write field larger than that of conventional patterning mask geometry. For our DBR fabrication of grating length $500 \mu\text{m}$, we have thus used e-beam write-field size of $500 \mu\text{m}$, accelerating voltage of 20 kV, aperture size $10 \mu\text{m}$ in e-beam system "Raith 150 Two".

2.3.3 Proximity Error Correction

Proximity error is the spreading out of the patterning dose in the close proximity geometry. Patterning dose is the amount of charge impinging the unit area of the mask geometry to be patterned and its unit is $\mu\text{C}/\text{cm}^2$. This occurs generally if (i) the small geometries in the mask are close enough, (ii) there is overdose defined for patterning and (iii) smaller area structure is in the vicinity of larger area structure although the dose for both is same. It is a type of diffusion of bombarded charge from high dose pattern to low dose pattern. The observation of the proximity error and their systematic removal is shown in the following example in three steps.

Step 1: we patterned the mask of a grating coupler (the mask is shown in the Fig. 2.23(a); left side areas are grating structures and right side area is the taper section surrounded from FBMS path) containing different area structures. The corresponding SEM image of the patterned structure using e-beam lithography with area dose $300 \mu\text{C}/\text{cm}^2$ and FBMS dose of $450 \mu\text{C}/\text{cm}^2$ is shown in Fig. 2.23(b). The dose spreads out from right side to the left side hence blocking the small openings of the grating structures.

Step 2: However, this proximity error can be reduced by shifting the highly dosed FBMS patterns away from the grating structures but keeping the dose factors unchanged. In Fig. 2.23(c), the FBMS area (blue colour border of the taper region) is shifted $5 \mu\text{m}$ towards right. The effect of keeping high dose area/path away from small-pitched grating can be seen in Fig. 2.23(d) - the SEM image of the corresponding mask as in Fig. 2.23(c). Reduction of proximity error is visible clearly.

Step 3: However, there is still some trace of the proximity error in the grating structures near to the tapered edge. To remove this fully, the dose factor of two grating pitch near the tapered edge is slowly reduced from 3.0 to 2.0 to $1.2 \mu\text{C}/\text{cm}^2$ (see Fig. 2.23(e) for the mask, the light blue and dark blue color shows the successively reduced dose). The SEM image of the corresponding patterned mask with the same dose as in Step 1 is shown in Fig. 2.23(f). It can be observed that the proximity error has gone completely from the patterned structure. Thus, the attention must be paid to remove the proximity error regarding the relative doses, structure size, a gap between the structures etc. For

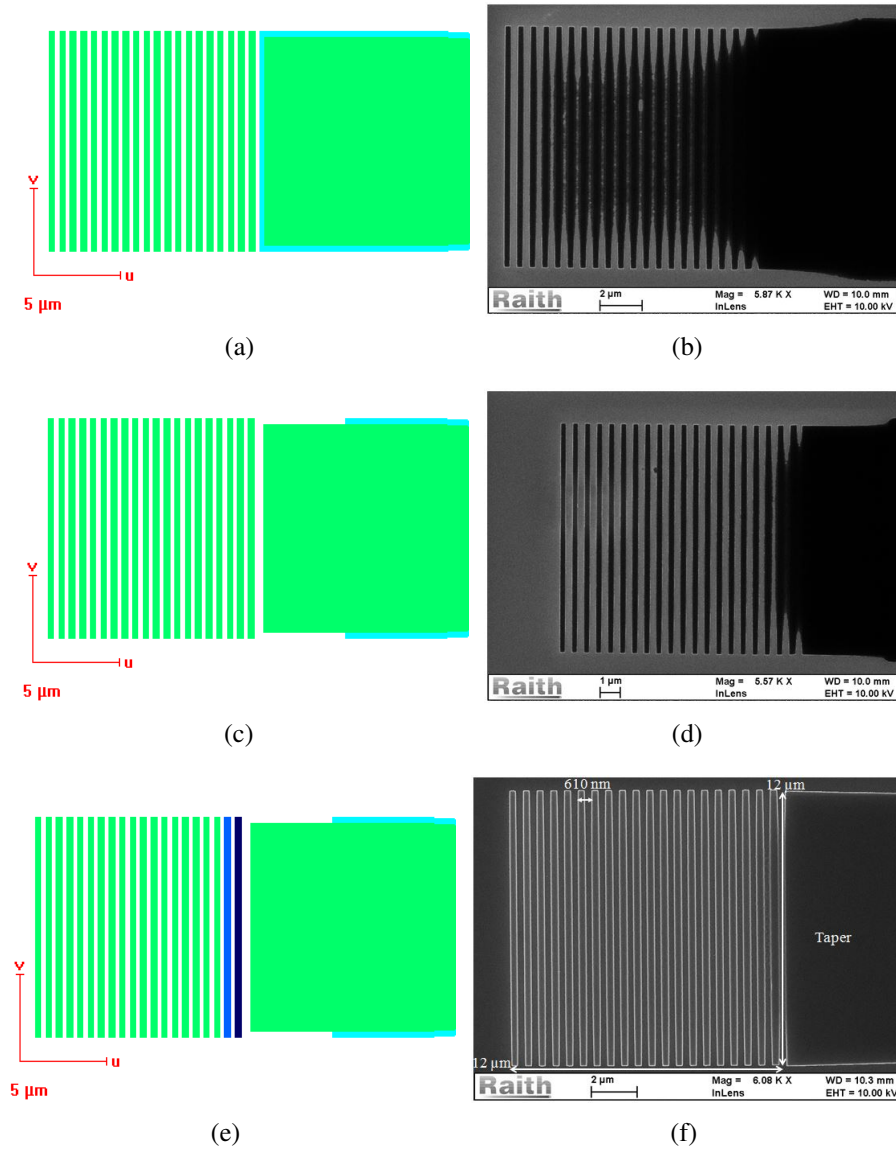
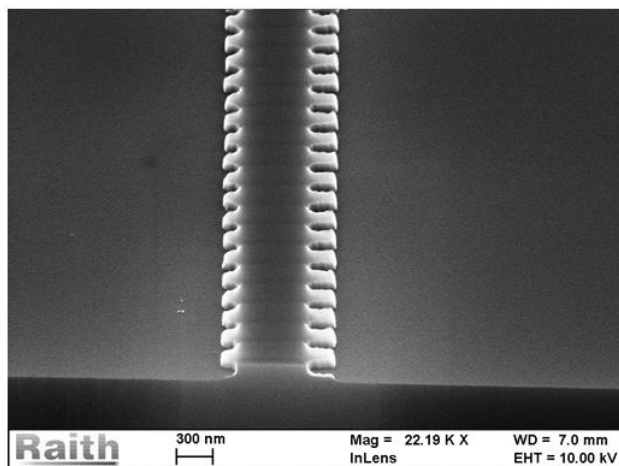


Figure 2.23: SEM images of input grating coupler showing proximity error (a) due to FBMS path kept near to conventional path, (b) due to FBMS path kept away to conventional path and (c) due to FBMS path kept away to conventional path and reduced conventional path dose.

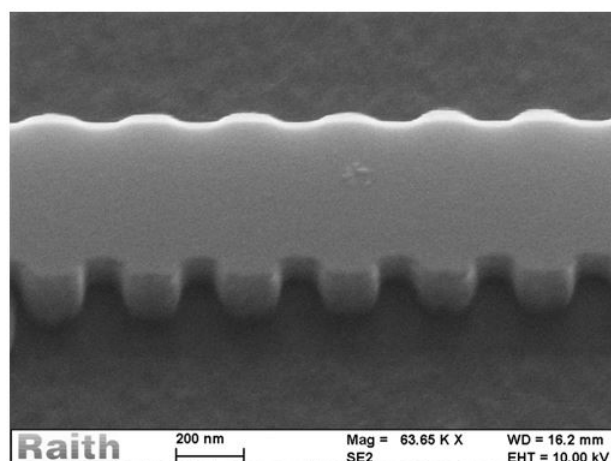
the device fabrication we have used conventional geometries to define all gratings and FBMS path to define long waveguide with conventional area dose of $\sim 300 \mu\text{C}/\text{cm}^2$ and FBMS area dose of $\sim 450 \mu\text{C}/\text{cm}^2$ with an accelerating voltage of 20 kV at aperture size of $10 \mu\text{m}$.

A grating period is an important parameter which decides the value of the Bragg wavelength. A small change in the grating period can shift the Bragg wavelength significantly. Ideally, there should not be any period variation while patterning the grating

using e-beam lithography, however, its pitch or duty ratio can vary as it depends upon the resist, dose, patterning time, development time and dry etching methods. There is consistency in the grating period between the defined and measured values.



(a)



(b)

Figure 2.24: SEM image of an integrated DBR waveguide (a) cross sectional view and (b) side view. The image was taken at 45 degree inclination of the sample with horizontal. The etch depth is ~ 100 nm on a device layer thickness of 250 nm.

The cross-section of the grating was imaged to measure the etch depth of the waveguide and grating for an optimized Fluorine based dry etch recipe. The SEM image of the grating cross section is shown in the Fig. 2.24(a). 100 nm etch depth was measured for the device layer thickness of 250 nm after etching for 11 seconds. The etching recipe will be discussed in the following section. The unequal grating modulation depth on each side is due to the shift of the grating structures in e-beam lithography. The random

shift and sidewall roughness of the grating can be made better by gaining more and more experience and skill in patterning. However, some error is inherently machine dependent. As for example, we pattern the mixture of a conventional area (used for fins of the grating) and FBMS path (used for a waveguide of longer length) which is being patterned by a different method by the e-beam machine. The patterning time, settling time and stitching time, dose, etc. vary accordingly. For a longer waveguide with a grating structure, we pattern FBMS path for longer waveguide first then the conventional grating structures afterward. Since the patterning electron beam system and the stage holding the sample move for a long time, a small inherent shift of ± 10 nm were observed. Fig. 2.24(b) shows the SEM image of side view of the DBR inclined at 45-degree angle with horizontal. The grating modulation seems to be unequal because it is a perspective view of a 3D structure. The etch depth was measured to be ~ 100 nm for the device layer thickness of 250 nm. We solved each issue related to fabrication one by one with the best consideration. We repeated the fabrication to analyze the consistency and repeatability of the device. Finally, the optimized device fabrication process parameter is discussed in the following section.

2.3.4 Device Fabrication : Optimized Process Parameters

1. Spin coating of e-beam resist (HSQ):

The cleaned sample was prebaked at temperature 180° C for 3 min to remove moisture from the silicon surface. Then e-beam negative-tone resist Hydrogen Silsesquioxane (HSQ XR1541) were spin-coated on the top silicon surface in two steps: step1:- speed = 100 rpm, acceleration = 1500rpm/sec, time = 10 sec, step2:- speed = 3000 rpm, acceleration = 1500 rpm/sec, time 40 sec. The HSQ resist thickness measured to be ~ 100 -150 nm which is in accordance with the database of the HSQ.

2. Mask transfer: electron beam lithography

HSQ coated silicon sample was then prebaked at 200° C for making uniformity of coated surface, then the sample was loaded inside the load lock and carried inside the electron gun chamber with the help of computer command. The sample was patterned by electron beam writing (Raith 150 TWO system) using both the conventional patterning and the fixed beam moving stage (FBMS) patterning technique for removing any unwanted stitching error with the patterning parameters as FBMS area dose: $100 \mu\text{C}/\text{cm}^2$, area dose: $90 \mu\text{C}/\text{cm}^2$ accelerating Voltage: 20 kV, Aperture : $10 \mu\text{m}$, working distance: 10 mm for calculated patterning time ~ 8 hrs.

3. Development of unexposed resist

To remove the unexposed region from the sample the exposed sample was developed for 6 min. in MF-319, 30 sec. in DI water and 15 sec. in IPA and then hard Bake at 300° C. The schematic of the sample with HSQ-mask is shown in Fig. 2.20 (b).

4. Dry etching of silicon

The exposed and hard baked sample was etched up to depth of ~ 100 nm by using inductively coupled plasma reactive ion etching (ICPRIE) system (Oxford Plasmalab System 100) with the etching parameters as gas flow rate- $SF_6 : CHF_3 :: 5$ sccm : 18 sccm, chamber pressure- 15 mT, ICP power- 1000 W, forward power - 30 W and operating temperature - 20° C to obtain nearly vertical side-walls and an acceptable surface roughness. The schematic of an etched sample is shown in Fig. 2.20 (c).

2.3.5 Characterization Results

Waveguides, side-wall gratings, and grating couplers were defined simultaneously with single-step e-beam lithography using negative-tone resist (HSQ) and subsequent inductively coupled reactive ion etching (ICP RIE) to obtain a slab thickness of $h = 150$ nm. Both of the input and output grating couplers were interfaced to waveguide with an adiabatic taper of length equal to $100 \mu\text{m}$ connecting grating coupler of width $12 \mu\text{m}$ to rib waveguide of width 560 nm. Fig. 2.25(a) and 2.25(b) shows the SEM images of input grating coupler and corresponding taper interfaced with waveguide respectively.

Also Fig. 2.25(c) and 2.25(d) shows the SEM images of taper interfaced with the waveguide and corresponding output grating coupler respectively. Since the total length of the fabricated device is ~ 5 mm, the SEM image of whole structure will not be visible clearly. However, connecting the figures 2.25 (a), (b), (c) and (d) in a straight line will give the idea of the whole device. Fig. 2.26 shows the enlarged view of SEM image of the grating coupler. The period of the grating coupler was measured to be 610 nm which is exactly equal to the value we defined in the mask. Also, we achieved the ~ 50 % duty ratio in the grating.

For the fabrication of DBR and DBR cavity to obtain high reflectivity and high-quality factor, the device parameters were derived from the analytical modeling for the DBR devices as in the DBR Section. However, the period of the grating was changed from 282 nm to 290 nm to observe the effect of grating period on Bragg wavelength.

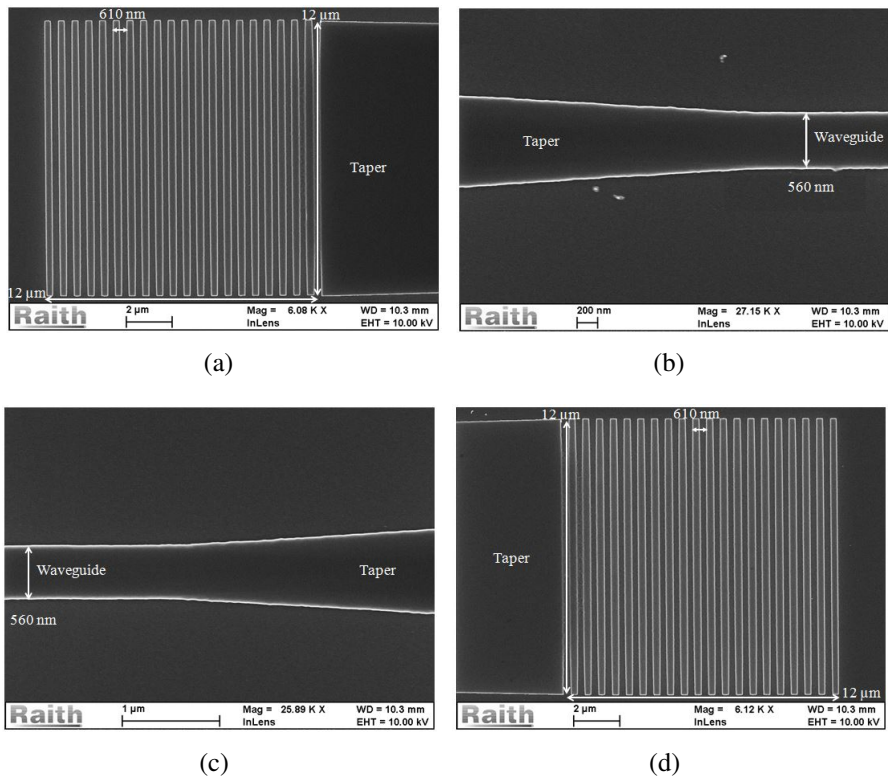


Figure 2.25: SEM images of (a) input grating coupler, (b) tapered part of input grating coupler, (c) out grating coupler and (d) tapered part of output grating coupler

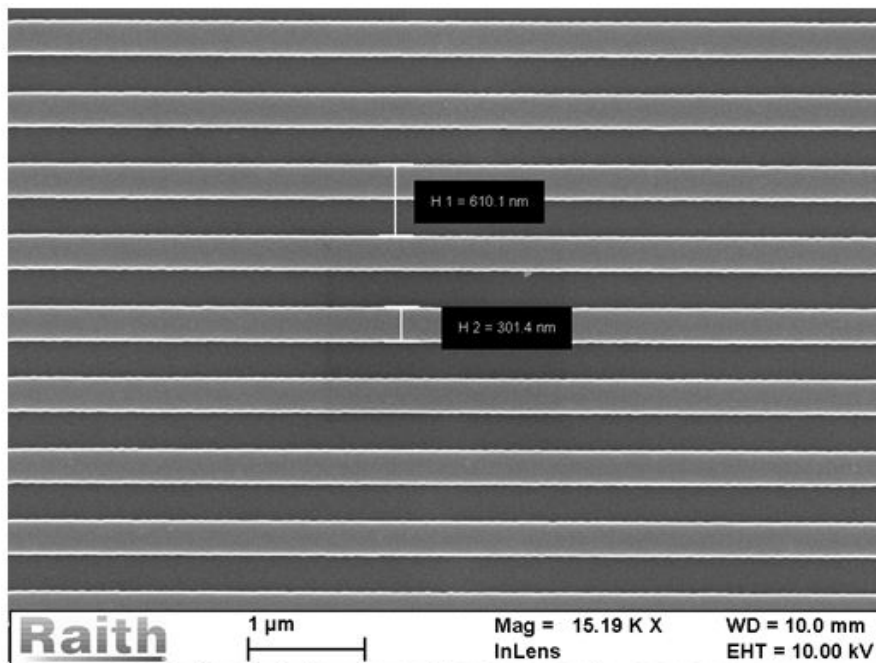


Figure 2.26: SEM image of the grating coupler showing duty ratio of $\sim 50\%$ with grating period - 610 nm.

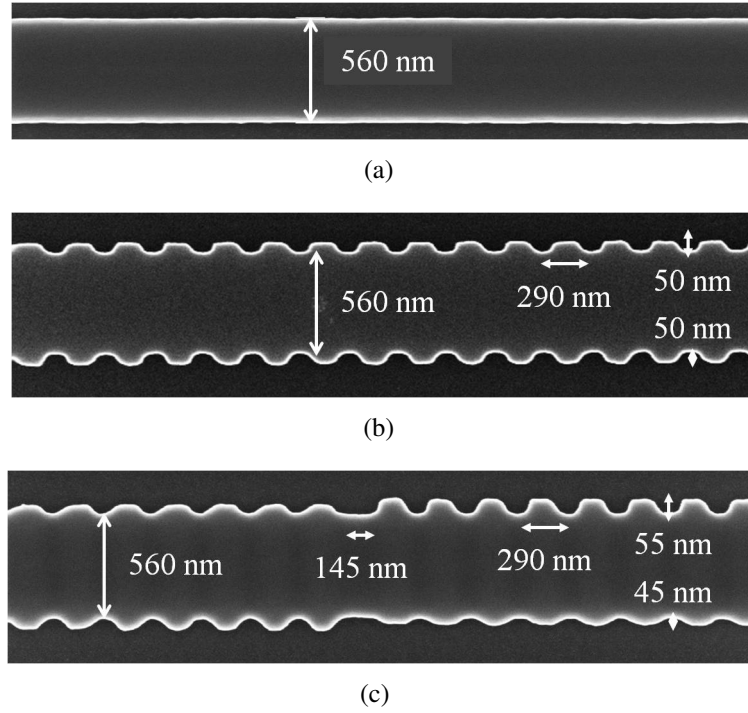


Figure 2.27: SEM images of the fabricated devices in a single mode SOI waveguide: (a) straight waveguide, (b) DBR grating and (c) phase shifted grating.

Table 2.3: Optimized parameters for waveguide and grating fabrication

Waveguide Parameters			Grating Parameters			
W [nm]	H [nm]	h [nm]	Λ [nm]	ΔW [nm]	L_g [μm]	λ_B [nm]
560	250	150	290	50	500	1550

The finally selected waveguide and DBR device parameters are tabulated in Table 2.3. For DBR cavity, the quarter-wave phase-shifted cavity length was taken as 145 nm for fabrication.

The SEM images of straight waveguide, DBR grating and phase shifted grating is shown in Fig. 2.27. Although, the grating modulation was defined in rectangular shape after fabrication edge rounding took place. This is caused mainly due to use of higher write field of the electron beam lithography system in order to pattern longer grating length. Longer grating length is desirable to increase grating reflectivity. Although, grating reflectivity can be increased by increasing κ or ΔW (from Eq. 2.17), it may introduce waveguide loss due to device fabrication imperfection (larger value of ΔW introduces more scattering loss, to minimize waveguide loss due to surface roughness,

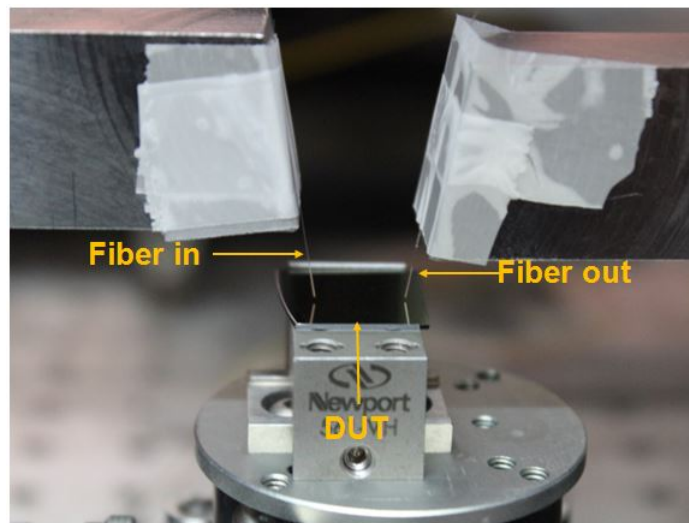
a shallowly-etched waveguide and smaller grating modulation width are preferred).

On the other hand, fabrication of sub-wavelength period grating of longer length is challenging in case the grating is patterned using electron beam lithography system. Grating pitch in the order of some hundred nm shall be patterned at a high accelerating voltage of an electron beam with smaller write field for obtaining better resolution and less surface roughness. But the smaller write field would cause stitch field error while writing longer grating length (longer than write field). One way to get rid of stitch field error is to use fixed beam moving stage of the patterning system. But unfortunately, this process is slow enough to write a large number of discrete component (as for example, the grating length of 1mm with the grating period of 300 nm would result in 3333 grating components). However, the longer length DBR can be designed in the spiral way of the small radius would solve the stitch field error as well as can maintain surface uniformity by choosing smaller write field but at the cost of loss introduced due to waveguide bending and larger footprint (due to spiral structure). The example of DBR integrated into the spiral waveguide to increase the overall grating length is given in [91]. So there is a trade-off between the stitch-free fabrication and device uniformity. Higher write field is required to pattern longer device containing many components is shorter time duration (within some hours) to get rid of the stitch-field error. The fixed-beam moving stage (FBMS) technique of patterning is the alternative to get stitch-free patterning but at the cost of increased time of patterning. In our case, the number of grating components (which can be calculated by dividing grating length L_g from grating period = $500 \mu\text{m} / 0.29 \mu\text{m} = 1724$) is too large to be written using FBMS technique. So we used write-field of size $500 \mu\text{m} \times 500 \mu\text{m}$ to pattern the grating of length of $L_g = 500 \mu\text{m}$. There is the process of write-field alignment, where we need to teach an algorithm to the patterning software in order to reduce error in step-size of electron gun head movement. Smaller the size of write-field more the accuracy in step-size can be achieved, however, it also depends on a manual alignment which can differ person to person. And higher accuracy in step-size determines better resolution. Since, the patterning at a single point is circular in shape, lower resolution due to use of higher write-field causes edge rounding at corners of the structure.

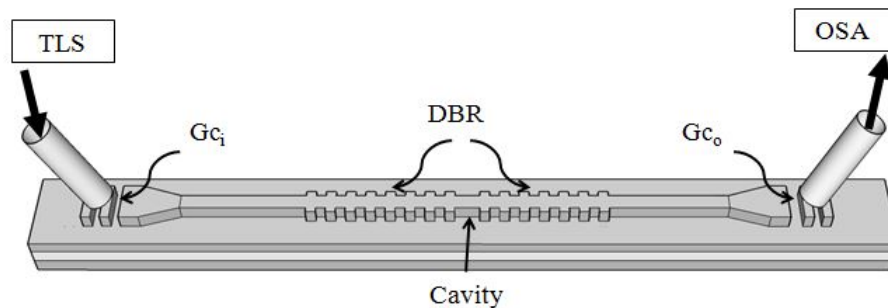
Period of the grating in a fabricated device remains unchanged irrespective of the

write field. Some deviation in the actual period may occur due to bad alignment practices, but it will be of random nature giving the zero standard deviation in the grating period. Hence the Bragg wavelength can be fixed reliably which solely depend on grating period unless there is no variation in waveguide parameters like slab height and core width.

The fabricated devices were characterized using the experimental setup as shown schematically in Fig. 2.28(b). A high-resolution optical spectrum analyzer (OSA)



(a)



(b)

Figure 2.28: (a) A photograph of the characterization setup showing input/output fiber holder and device under test (DUT) and (b) Scheme of the experimental set-up used for device characterizations, $Gc_{i/o}$ - grating input/output couplers, TLS - tunable laser source ($1520 \text{ nm} \leq \lambda_L \leq 1620 \text{ nm}$, $P_L = 250 \mu\text{W}$), OSA - optical spectrum analyzer, DBR - distributed Bragg reflector. TLS is accessed from the in-built OSA system (Apex 2043B).

with an in-built tunable laser source (TLS) manufactured by Apex Technologies (Apex 2043B) was used for characterizations. The fiber-optic TLS output ($1560 \text{ nm} < \lambda_L <$

1620 nm, Power - 250 μ W) is fed directly to input grating coupler (GC_i) and the transmitted light through the output grating coupler (GC_o) is collected by another single-mode fiber for measurement using OSA with a resolution bandwidth of 0.8 pm. Since the waveguides were designed to support only TE-like guided modes, all the measurements to be discussed here are corresponding to the excitation of TE-like guided modes.

The transmission spectra of straight waveguide (six devices D_1 to D_6) interfaced with input/output grating couplers are shown in Fig. 2.29. Since the grating coupler

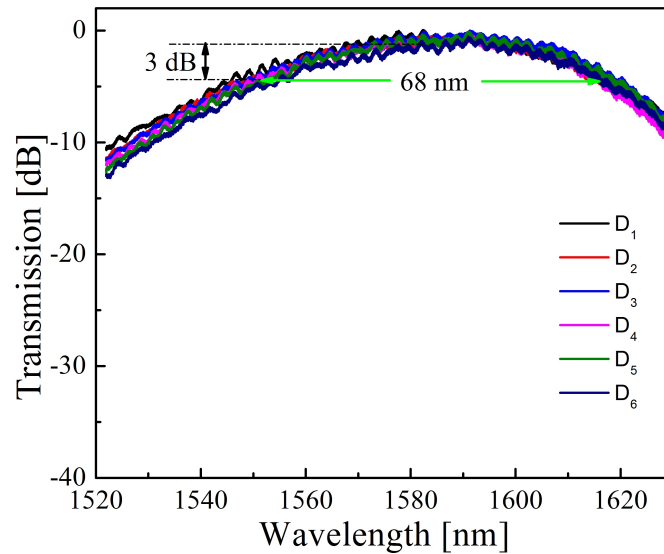


Figure 2.29: Schematic representation of fabrication process flow of the three devices (straight waveguide, DBR grating and DBR grating cavity) in SOI with input/output grating coupler: (a) starting SOI wafer, (b) Devices patterned with e-beam resist HSQ, (c) Devices after dry etching of patterned devices and (d)

response is wavelength dependent, the 3 dB bandwidth of input/output grating couplers was measured to be \sim 68 nm. This bandwidth can be further increased by considering proper design parameters, for instance, both the grating length and grating modulation depth of the grating coupler can be increased. Longer grating length will introduce more loss so, increasing the grating length is not desirable. Also, if the increased grating modulation depth is not the same as the waveguide etch-depth, then two-step e-beam lithography will be required to define both etch depth separately. In our case, both the waveguide etch-depth as well as grating modulation depth were optimally selected same, so that only single-step e-beam lithography can pattern both together. Since DBR and DBR cavity devices have their bandwidth within some nm (as we simulated), the 3

dB bandwidth (~ 68 nm) of input/output grating couplers is large enough to characterize these devices.

Fig. 2.30 shows the transmission characteristic of the device (the corresponding SEM image is shown in Fig. 2.27(b)). The bandwidth of the filter was measured to be

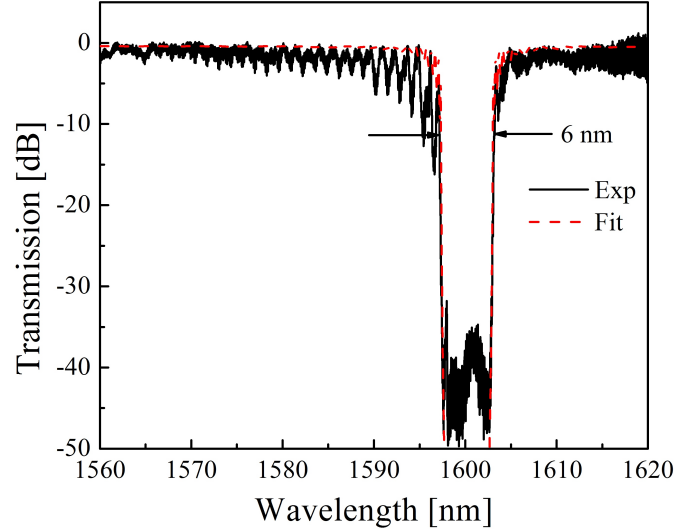


Figure 2.30: Transmission spectra of the DBR grating with waveguide parameters: $W = 560$ nm, $H = 250$ nm, $h = 150$ nm; grating parameters: $\Lambda = 290$ nm, $\Delta W = 50$ nm at both the side walls of the waveguide.

~ 6 nm centered at the Bragg wavelength $\lambda_B = 1601$ nm with the reflectivity of 38 dB. Such a high reflection resulted mainly due to longer grating length as stated in theory. It is observable from Fig. 2.30 that there is more ripples at a wavelength lower than the Bragg wavelength λ_B in comparison to that at the wavelength higher than the λ_B . The reason can be attributed to the more refractive index mismatch at a lower wavelength than compared to that at a higher wavelength. Since effective index (for a given waveguide parameters) reduces as the wavelength increases, therefore causing more index matching between the grating and waveguide interfaces at higher wavelengths, and lesser index matching between the grating and waveguide interfaces at lower wavelengths. Since it is known that for higher index mismatches at the interfaces, there occur ripples in the transmission due to Fabry-Perot cavity resonances. To extract the coupling constant and grating loss of the fabricated device, the device was modeled with analytical equations for contra-directional coupling with the device parameters as in table 2.3. A MATLAB plot using transfer matrix for the analytical equation fits at $\kappa = 0.0125 / \mu\text{m}$, loss $\alpha = 8$ dB/cm (see Fig. 2.30 MATLAB fitting plot in red colour).

This extracted κ value nearly matches with theoretically calculated value of κ ($= 0.0132 / \mu\text{m}$).

Fig. 2.31 shows the transmission characteristic of the DBR cavity device. The corresponding SEM image of the device is shown in Fig. 2.27(c). A very sharp resonance peak in transmission is observed with 3 dB bandwidth of ~ 20 pm and quality factor of 8×10^4 . Resonance peak is 11 dB below the out-of-band transmission with a peak

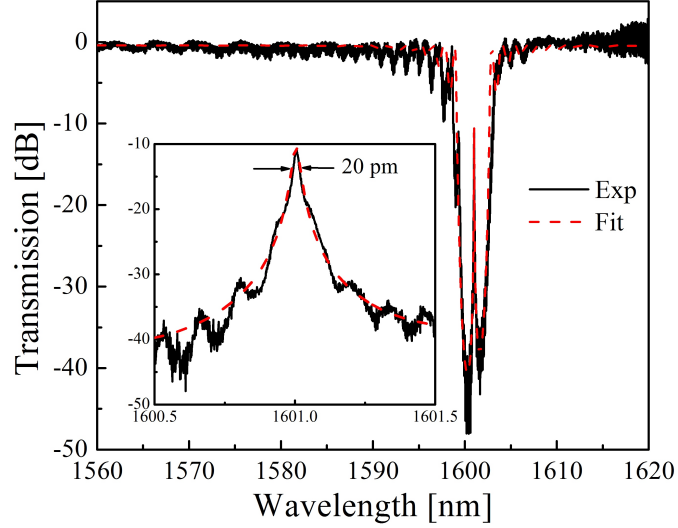


Figure 2.31: Transmission spectra of the DBR grating cavity with waveguide parameters: $W = 560$ nm, $H = 250$ nm, $h = 150$ nm; grating parameters: $\Lambda = 290$ nm, $\Delta W = 50$ nm at both the side walls of the waveguide with cavity length $L_c = 145$ nm.

height of ~ 20 dB from the reflection band. The peak height can be further increased by reducing grating losses due to sidewall roughness incurred in fabrication processes. Here also, a MATLAB plot using transfer matrix method fits for $\kappa = 0.013 / \mu\text{m}$, loss $\alpha = 8$ dB/cm, with other parameters being same as for fabricated device ($W_1 = 560$ nm, $\Delta W = 50$ nm). The extracted value of κ ($0.013 / \mu\text{m}$) nearly matches with theoretically calculated value of κ ($= 0.0132 / \mu\text{m}$) for $\Delta W = 50$ nm.

The Bragg wavelength detuning based on device parameters was addressed in Section 2.2.1. Theoretically, for the grating period $\Lambda = 282$ nm, the Bragg wavelength results at $\lambda_B = 1550$ nm for the given waveguide parameters. Therefore, by considering the λ_B detuning is linearly dependent on Λ with the slope $\frac{d\lambda_B}{d\Lambda} = 5.5$, the λ_B for $\Lambda = 290$ nm should result at 1598 nm. We observe experimentally, that the λ_B for $\Lambda = 290$ nm is ~ 1600 nm. This small mismatch can be attributed to fabrication anomaly as there is

not a one-to-one matching between the waveguide width and slab height defined in the mask and etch recipe, and the waveguide width and slab height measured after fabrication. Also, the variation of effective index with respect to slab height is more prominent than variation in other parameters as discussed in the following Section. Thus, the λ_B at 1600 nm with $\Lambda = 290$ nm is consistent with the theory as discussed in the previous section.

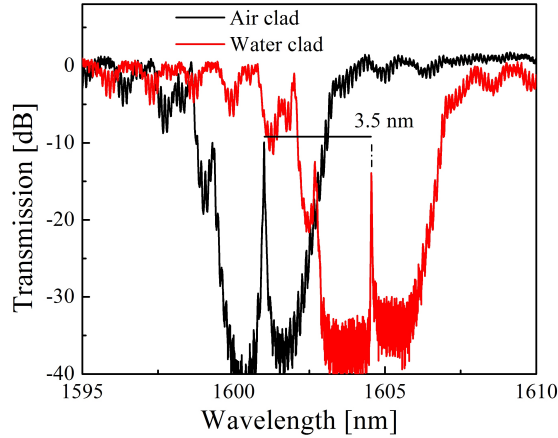


Figure 2.32: Transmission spectra of a DBR grating cavity with top cladding as air (in black colour) and water (in red colour).

The sharp resonance peak with very high-quality factor can be useful in spectroscopic applications such as refractive index sensing, bio-molecule detection etc. To see the effect of top cladding in the transmission, the DBR cavity device as in Fig. 4.8(a) were characterized with de-ionized water as top cladding. The resultant transmission characteristic is shown in Fig. 2.32. A shift of 3.5 nm in the resonance peak was measured from the graph.

2.4 Fabrication Tolerance

The rate of change of effective indices with respect to waveguide width and slab height can be represented as $\frac{d(n_{eff}^{0m})}{dW}$ and $\frac{d(n_{eff}^{0m})}{dh}$ respectively which varies as a function of both W and h . For waveguide width $W = 760$ nm, slab height $h = 150$ nm, rib height $H = 250$ nm, table 2.4 shows the rate of change of effective indices with respect to waveguide width and slab height.

Wafer bow and warp can generally deviate slab height while fabrication processes

Table 2.4: Slope of effective index versus W, h curves at W = 760 nm, H = 250 nm and h = 150 nm

Mode index m	Slope w.r.t. W at h = 150 nm $\frac{dn_{eff}^{0m}}{dW}$ [nm ⁻¹]	Slope w.r.t. h at W = 760 nm $\frac{dn_{eff}^{0m}}{dh}$ [nm ⁻¹]	Slope ratio $(\frac{dn_{eff}^{0m}}{dh}) / (\frac{dn_{eff}^{0m}}{dW})$
0	2.2×10^{-4}	4.69×10^{-4}	2.13
1	11.35×10^{-4}	36.92×10^{-4}	3.25

like patterning and etching may also produce variation in waveguide width and etch depth. Thus device to device non-uniformity in the waveguide dimension (although fabricated on the same wafer by following same process steps) brings variation in the spectral and spatial characteristics of the devices. Special characteristics like mode index, mode profile and coupling coefficients may vary from device to device. Spectral characteristics like resonance wavelength reflected or transmitted may also vary from device to device. Thus, the λ_B can be detuned by varying grating period Λ and effective index of the guided mode. Using Fig. 3.7, we estimate the values of $\frac{d\lambda_B}{dW}$ and $\frac{d\lambda_B}{d\Lambda}$ as 0.25 nm/nm and 5.5 nm/nm, respectively. Bragg wavelength tuning is more convenient by controlling grating period. The proposed device structures are discussed first analytically with the help of coupled mode theory (small perturbation). They are then validated with a set of optimized parameters by FDTD simulations. Finally, The device were fabricated and characterized. Unfortunately, the measured device parameters (width & height, duty cycle etc.) deviates from that of the design parameters. And they can not be measured accurately in nanometer scale to compare with simulation results. These are the source of discrepancy in the wavelength characteristics of the simulated and fabricated structures.

2.5 Summary

Sub-micron dimension waveguide in SOI was presented in the light of effective indices and polarization of the guided mode(s) in order to study the effect of waveguide parameters on guided mode(s). The waveguide dispersion was studied mainly because of the DBR device are highly dispersive around the phase-matched wavelength. The DBR

devices were fabricated using the standard process developed in our laboratory. During fabrication, using e-beam lithography system, we found stitching error for a longer grating length which was mitigated using longer write field. Proximity error was another problem in patterning mixture of FBMS path and conventional geometries which was removed by proper design and dose selection. Integrated DBR and DBR cavity devices were demonstrated in a single mode SOI waveguide of 250 nm device layer thickness. Input-output grating couplers were integrated at both the ends of the waveguide in a single-step of e-beam patterning. The 3dB bandwidth of the grating coupler was found to be ~ 68 nm. The reflectivity of the DBR filter device was measured to be ~ 38 nm with the grating length of $500 \mu\text{m}$. A quarter-wave phase-shifted DBR cavity was designed with a shallowly etched waveguide, small grating modulation depth and longer grating length with submicron size grating period. The Q-factor of the fabricated DBR cavity device with the optimized parameter is measured to be as high as 8×10^4 . The overall footprint of the device is small.

Our work can be compared With the help of the results published for DBR cavity devices in the sense of some figure of merits like (i) device footprint and (ii) Q-factor, and in the sense of the device design parameters. The comparison table is shown in the Table 2.5.

Table 2.5: Figure of merit comparisons of DBR cavity with earlier reported works.

Parameters	Ref. [81]	Ref. [52]	Ref. [91]	Present work
L_g	155 μm	20 μm	2000 μm	500 μm
Loss	45 dB/cm	6.5 dB/cm	7 dB/cm	8 dB/cm
Footprint	155 μm^2	20 μm^2	20700 μm^2	250 μm^2
Q-factor	6×10^3	1.3×10^4	1×10^5	0.8×10^5

High Q-factor and small footprint are the major figures of merit for the DBR cavity devices. As we discussed earlier, Q-factor can be maximized primarily by increasing grating reflectivity and in reducing grating losses. For this, the desired quality of device parameters are smaller etch-depth, small grating modulation depth ΔW , longer grating length L_g and lower grating losses. In the table, the best desirable values of the parameters are shown in blue color, while the worst desirable values are shown in red color. In our present work, the value of ΔW of 50 nm is the minimum and the Q-factor of $0.8 \times$

10^5 is comparable to the best-published result. The footprint of our presented devices is far smaller than that of "Zou et. al.". Also one can notice that there is not a single undesirable value of any parameters.

CHAPTER 3

Rectangular-Edge Filter

In previous Chapter, DBR and phase shifted DBR cavity integrated in single mode SOI rib waveguide with symmetric waveguide width modulation were studied in support of the phase matching condition and the coupling coefficient between the fundamental TE modes to analyze their spectral characteristics. In this chapter, we extend the study of phase matching condition and the coupling coefficient to not only between fundamental-to-fundamental guided mode but also between fundamental-to-first order guided mode by integrating a DBR structure using asymmetric waveguide width modulation. This results into an expected rectangular edge filter characteristics as described in Chapter 1. The device is described first by semi-analytical coupled mode theory and then validated with FDTD simulation and experimental results.

Although, many DBR designs based on different applications have been reported as we discussed in the motivation section of Chapter 1, there is no similar work presented in the literature of DBR till date to the best of our knowledge as we are presenting in this chapter. The novel device is implemented by integrating side wall grating of sub-wavelength period ($\Lambda = 290$ nm) and of length ($L_g = 500$ μm) in a multimode SOI rib waveguide. The device is designed such that spectral characteristic of the DBR filter falls within optical C and L-band (1530 nm $\leq \lambda \leq 1625$ nm). The device is accessed by input/output single-mode waveguides via input/output taper waveguides. The device exhibits well-defined wavelength edge (λ_{edge}) which is rectangular in shape. so that, it is termed as rectangular-edge filter (REF). Such rectangular edge of the filter will find useful applications in designing compact intensity modulator. The working principle can be referred to the ring-resonator based intensity modulators [39]. The active modulator based on the principle of electro-optic absorption with very high extinction ratio can also be implemented using the REF device. In entangled photon generation, the pump signal can be filtered out effectively by using such a REF device. The RF photonics filters such as bandpass filter, notch filter used for RADAR signal processing

can also be implemented by offering no signal delay by virtue of the device characteristic [99]. The device characteristics with higher edge-slope can find versatile application such as integrated optical lab-on-chip for on-chip signal processing and routing purpose [100]. Like a high Q DBR cavity, the high roll-off of the filter edge would find applications in spectroscopy [101]. The smallest feature size of the device is about 145 nm which is well below the diffraction limits of the normal photolithography laser system. Thus we prefer an electron beam lithography system for the device fabrication. The grating couplers, input/output waveguides, grating waveguide and input/output taper waveguides were simultaneously defined in a single mask layout and were fabricated in a single step electron beam exposure. The device was etched uniformly up to ~ 100 nm from the top using inductively coupled plasma reactive ion etching system after e-beam exposure. The fabricated device was characterized using grating coupling characterization setup. The source wavelength in the range of 1520 nm to 1630 nm was launched using inbuilt laser source of an optical spectrum analyzer. The collected transmission wavelength was analyzed again by an optical spectrum analyzer. All the devices exhibit two Bragg wavelengths with discrete (non-overlapped) stopbands arises due to coupling among confined mode(s). It also exhibits other Bragg wavelengths also with continuous (overlapped) stopbands arises due to coupling among confined fundamental mode and unconfined slab mode(s).

The characterization and measurement results show that the the devices have a sharp step-like rising filter edge with the passband to stopband extinction ratio of > 40 dB. The steeper edge of the filter has a slope of 118 dB/nm at the edge wavelength of $\lambda_{edge} \sim 1560$ nm. A wide passband of width ~ 40 nm is observed to the right side the filter edge. The wide passband is terminated by the stopband at the Bragg wavelength $\lambda_B^{00} \sim 1600$ nm arising due to first order mode coupling. Also, a wide stopband of width > 40 nm is observed to the left side of the filter edge. The device characterization is limited within the wavelength range of $1520 \text{ nm} \leq \lambda \leq 1620 \text{ nm}$ due to measurement limit of spectrum analyzer. Wavelength tunability of the REF device spectrum is also studied with respect to cladding material of different refractive index. We measured the sensitivity of the device to change in cladding material as ~ 18 nm/RIU. For a handheld power-meter of minimum detectable power of 1 dB, can record a minimum change in refractive index of the cladding material of 5.3×10^{-4} RIU near cladding index of

1.318 (DI water).

3.1 Design and Theoretical Analysis

The 3D schematic of the proposed device is shown in Fig. 3.1(a). The device is defined in SOI. There are two identical input and output waveguide designed to support fundamental mode only. The waveguide at the middle of the device is integrated with side-

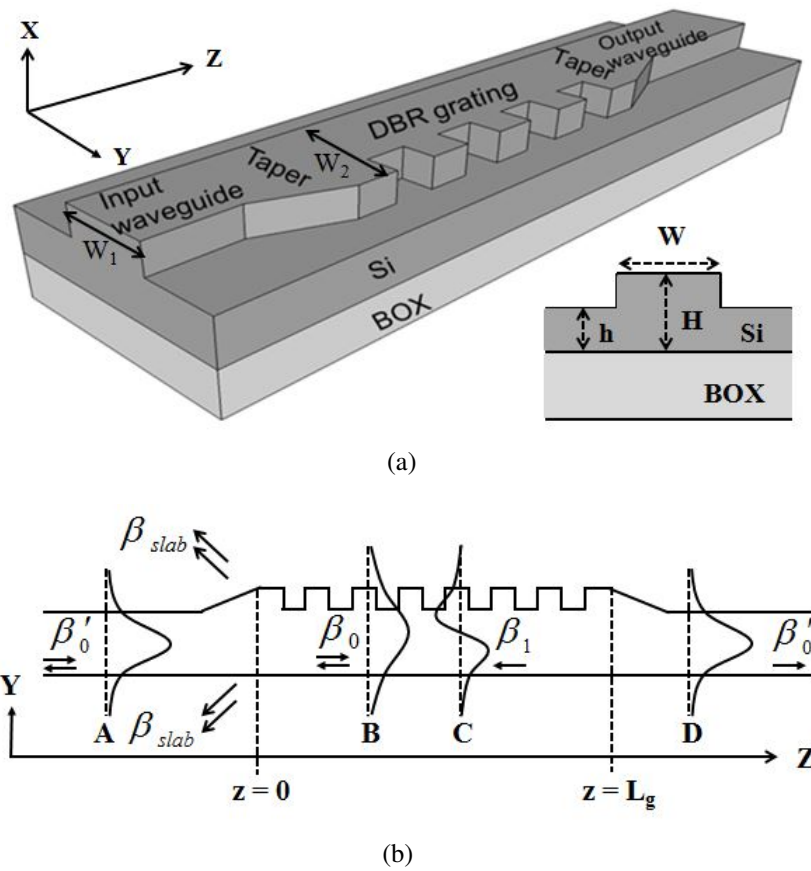


Figure 3.1: Schematic representation of the proposed REF device: (a) 3D schematic view of the proposed device and generic cross-sectional view of the SOI rib waveguide with design parameters W , H and h ; BOX - buried oxide. The handle silicon layer (typical thickness of $\sim 500 \mu\text{m}$) has not been shown below the BOX layer (typical thickness $1\text{-}3 \mu\text{m}$) in the scheme; (b) top view showing grating in one of the side-walls; A, B, C and D represent typical guided mode field distributions; β'_0 , β_0 , β_1 and β_{slab} are the propagation constants (arrow heads represent the direction of propagation);

wall grating of sub-wavelength period is designed to support two lower order modes - the fundamental and the first order mode. The middle waveguide with DBR is at

one of the side wall is interfaced to the input and output waveguide via identical input and output taper section respectively. The input and output waveguides are interfaced with input and output grating couplers to facilitate optical measurements. However input/output grating coupler is not being shown in the device scheme. The cross-sectional geometry of the device is defined by the waveguide width W , device height H and slab height h . The waveguide widths in the input/output waveguide and in the side wall grating waveguide are W_1 and W_2 respectively. Waveguides are further assumed to support only the TE-like modes. Fig. 3.1(b) represents the top view of the REF device showing the wavevectors along with direction and the confined mode field profiles in different region of the device. In the scheme (top view), at cross sections A and D in the input and output single mode waveguide respectively, the fundamental guided mode with propagation constant β'_0 is excited from the input side (left-side). When it enters the input taper waveguide, the mode expands adiabatically into a forward propagating fundamental mode with propagation constant β_0 in the grating region. The taper length can be selected to convert the mode adiabatically without losing the modal power to excite any other mode(s). The taper length for adiabatic mode transition is decided by FDTD simulation of the taper. It is discussed in the simulation section later.

The DBR integrated in the multimode waveguide helps to reflect phase matched wavelength in the form of both the modes - the fundamental mode and the first order mode. Since the refractive indices of both the mode differs, the phase matched wavelength would also differ. Thus, the forward propagating fundamental mode at some phase matched wavelength say λ_B^{00} couples to the backward propagating fundamental mode as well as the forward propagating fundamental mode at some phase matched wavelength say λ_B^{01} couples to the backward propagating first order mode (see Fig. 3.2, three different coupling resulting into different wavelength bands are shown). λ_B^{01} would depend on the refractive indices of both the modes alike λ_B^{00} which solely depends on the refractive index of the fundamental mode in all conventional grating devices. Since effective refractive index of first order mode is less than that of the fundamental mode, it can be obviously shown that $\lambda_B^{01} < \lambda_B^{00}$. Coupling constant plays a major role in deciding the amount of survival of the phase matched wavelength in the backward direction. We would receive zero reflection intensity if the coupling constant is zero for the phase matched wavelength. The coupling constant is symmetric function of the

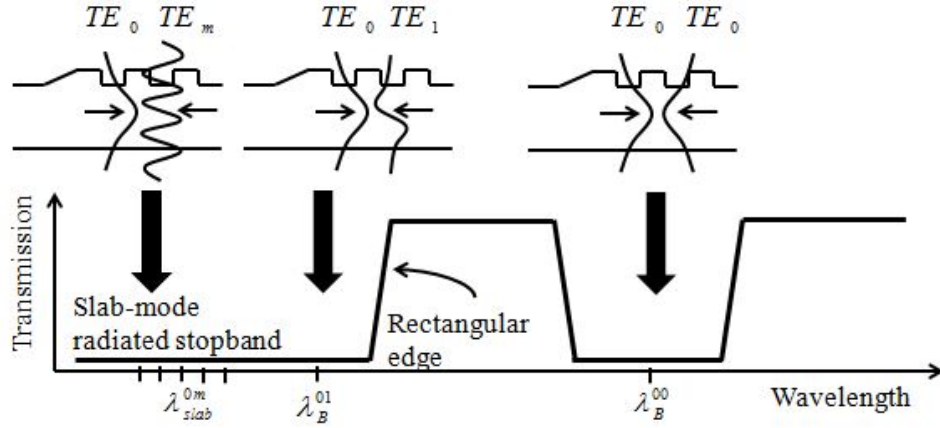


Figure 3.2: Expected wavelength spectrum of a REF device. The stopbands are shown to be resulting due to coupling between different mode pairs. They are centered at phase matched wavelengths: λ_B^{00} , λ_B^{01} and λ_{slab}^m ($m > 1$)

transverse direction of the waveguide. So depending on the symmetricity of transverse guided mode(s) and symmetricity of the grating modulation with respect to waveguide transverse direction, the coupling constant can be zero or non-zero. The grating kept at only one of the side walls of the waveguide confirms non-zero coupling constant for both the backward propagating modes, while the grating kept at both the side walls of the waveguide ensures zero coupling constant for the first order backward propagating mode (or any asymmetric backward propagating mode. When the first order mode propagating in the backward direction reaches input/output waveguide, it is being reflected into the slab as the input/output waveguides were designed to support the fundamental mode only. From the above discussion, it can now be ensured that the phase matched wavelength λ_B^{01} will be missing from the transmission spectrum at the output as it is reflected in the grating region but will not be able to reach in the input waveguide. At the same time, the phase matched wavelength λ_B^{00} will be missing from the transmission spectrum at the output as it is reflected in the grating region and will also appear in the input waveguide. Coupling constant being non-zero for all the mode profiles in the proposed device, higher order non-confined modes propagating in the backward direction would also couple to the forward propagating fundamental mode at the wavelengths smaller than λ_B^{01} . Stopbands around these wavelength would overlap providing a wider stopband to the left side of the λ_B^{01} (see Fig. 3.2). Thus, λ_B^{01} would behave as edge wavelength λ_{edge} of the REF device. The device would behave as high wavelength pass filter for the wavelength $\lambda_B^{01} < \lambda < \lambda_B^{00}$ while it would behave as low wavelength

pass filter for the wavelength $\lambda < \lambda_B^{01}$. With this qualitative discussion, we present here the theoretical analysis and simulation results of a REF device with rectangular edge responding around λ_B^{01} in optical C-band. and the and the DBR response around λ_B^{00} for conventional phase matching condition in the L-band ($\lambda_B^{00} \sim 1600$ nm). It must be noted that we have not considered the possible excitations of forward propagating higher order modes in the forward direction in grating region because of two reasons as (i) the adiabatic taper placed before the DBR would not excite any higher order mode(s) and (ii) if the some fraction of the input fundamental mode intensity gets converted to the higher order mode(s), it would phase match at some wavelength far away outside the optical L band.

3.1.1 Numerical Evaluation of Bragg Wavelength

From the above discussion, it is obvious that (a) the phase matching conditions and (b) non-zero coupling constants to backward propagating fundamental and first order modes are the important parameters to be paid attention during the DBR device design. They are addressed here with help of semi analytical method - that is some part is discussed with analytical equations and some part are discussed with the help of numerical mode simulation results. Later, the results were validated with the help of FDTD simulations using "Lumerical 3D FDTD" software.

The Bragg phase-matching condition, in general is given by:

$$\beta_0 - (-\beta_m) = \frac{2\pi}{\Lambda} \quad (3.1)$$

where $\beta_0 = \frac{2\pi}{\lambda} n_{eff}^0$, $\beta_m = \frac{2\pi}{\lambda} n_{eff}^m$ with n_{eff}^0 is effective index of forward propagating 0^{th} order mode (fundamental mode). n_{eff}^m is the effective indices of the backward propagating m^{th} order mode. For the waveguide supporting two guided modes only, the higher order modes (for $m > 1$) become leaky modes or slab modes which propagates in backward direction in the slab region. Now, corresponding to the integer value of $m = 0$ and 1, the backward propagating phase-matched wavelengths represented by λ_B^{00} and λ_B^{01} respectively can be obtained using Eq. 3.1:

$$\lambda_B^{00} = 2\Lambda n_{eff}^{00} \quad (3.2)$$

and

$$\lambda_B^{01} = \Lambda(n_{eff}^{00} + n_{eff}^{01}) \quad (3.3)$$

where n_{eff}^{0m} is the effective index of m_{th} mode. It is very important to describe here now that Bragg wavelengths given by Eq. 3.2 and 3.3 must be calculated iteratively as the effective indices appearing in the right side of the equation are the wavelength dependent. It would give false values of Bragg wavelength if these are calculated by substituting the values of effective indices computed for any waveguide dimension at any wavelength. So the actual Bragg wavelengths must be those which when are calculated at those refractive indices which are computed at those Bragg wavelengths. That is n_{eff}^{00} must be obtained at λ_B^{00} while n_{eff}^{01} must be obtained at λ_B^{01} . The corrected Bragg equation can be given as:

$$\lambda_B^{00}(updated) = 2\Lambda n_{eff}^{00}(\lambda_B^{00}) \quad (3.4)$$

$$\lambda_B^{01}(updated) = \Lambda(n_{eff}^{00}(\lambda_B^{01}) + n_{eff}^{01}(\lambda_B^{01})) \quad (3.5)$$

where $n_{eff}^{00}(\lambda_B^{00})$ and $n_{eff}^{00}(\lambda_B^{01})$ are the effective refractive indices of the fundamental guided mode at the wavelengths λ_B^{00} and λ_B^{01} , respectively; and $n_{eff}^{01}(\lambda_B^{01})$ is the effective index of the first order guided mode at wavelength λ_B^{01} . Since both the Bragg wavelength and effective indices are interdependent, one need to solve these equations in iterative manner to converge its values at some constant number. One can compute the effective indices at some reference wavelength as initial value and then Bragg wavelength has to be updated using Eq. 3.4 and 3.5. Now, effective indices must be updated at new Bragg wavelengths. Again Bragg wavelengths has to be updated using new effective indices and so on. After some iterations, converged values of both the effective indices and Bragg wavelengths can be considered as their actual values. The Fig.3.3 shows the flowchart to compute Bragg wavelengths and corresponding refractive indices iteratively for a given waveguide.

To start the iteration we compute n_{eff}^{0m} (for $m = 0, 1, 2$) as a function of waveguide width at a given reference wavelength $\lambda_r = 1550$ nm and slab height h as a parameter

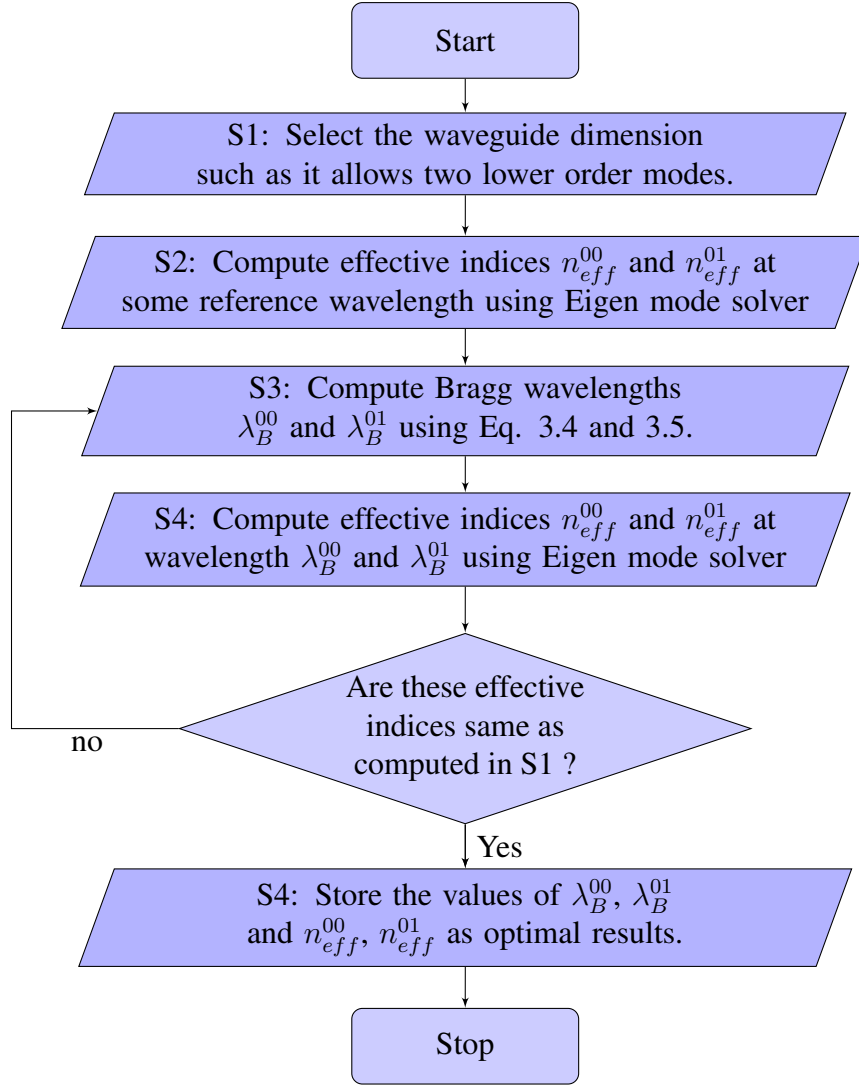


Figure 3.3: Flowchart: Iterative flowchart to compute Bragg wavelengths and effective indices

(using Lumerical mode solver). This has been already shown in Chapter 2, Section 2.1. With the help of Fig. 2.4, we select a waveguide width W such that it supports only two lower order guided modes (at λ_r) and corresponding $n_{eff}^{0m}(\lambda_r)$ (for $m = 0, 1$). For wavelength dependency of refractive indices, we again used Lumerical mode solver which is shown in Fig. 3.4(a). Then we compute the values of λ_B^{0m} ($m = 0, 1$) using these $n_{eff}^{0m}(\lambda_r)$. Now, we update the value of n_{eff}^{00} at λ_B^{00} and λ_B^{01} while n_{eff}^{01} at λ_B^{01} with the help of Fig. 3.4(a). Then we update λ_B^{0m} and so on until they are converged to constant values. This figure (Fig. 3.4(a)) can be used as look up figure to compute effective indices at different wavelength and at different waveguide widths. There exist cut-off $\lambda_{cut-off}$ wavelengths for each waveguide width W above which the

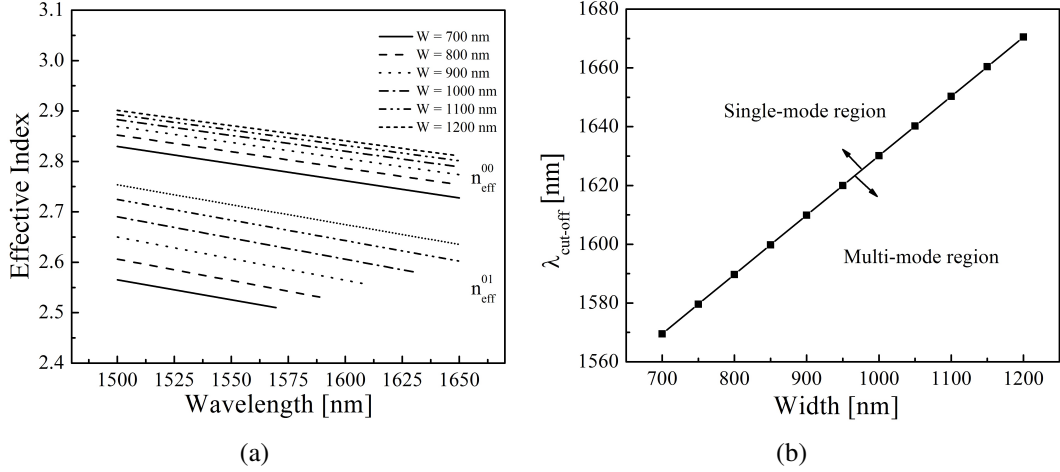


Figure 3.4: (a) Effective refractive indices versus wavelength; waveguide width being a parameter; (b) plot of the cut-off wavelength versus waveguide width

only single mode excitation is allowed. For instance, waveguide of $W = 700$ nm has the $\lambda_{cut-off} = 1570$ nm (see Fig. 3.4(b)). The Bragg wavelengths were iterated till it stopped fluctuating and settled at constant values for the value of grating period $\Lambda = 290$ nm and for the waveguide height $H = 250$ nm, slab height $h = 150$ nm and waveguide width being selected in multimode region. A plot for the Bragg wavelengths versus number of iteration at different waveguide widths is shown in Fig. 3.5. It is clear from figure that the Bragg wavelengths settle after 6^{th} iterations. This iteration process was

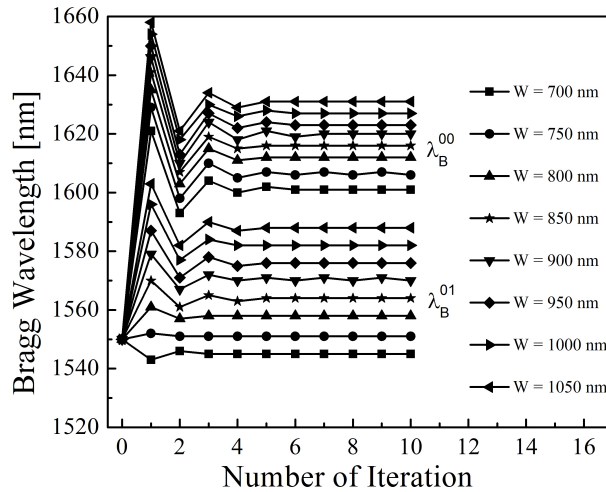


Figure 3.5: Bragg wavelength convergence in iterative manner at $\Lambda = 290$ nm; waveguide width being the parameter. At $\sim 6^{th}$ iteration, Bragg wavelengths start converging. The effective indices were calculated for $H = 250$ nm and $h = 150$ nm.

repeated for the several values of grating period starting from $\Lambda = 282$ nm to $\Lambda = 292$

nm in the step of 2 nm at different waveguide widths within the multimode limit for the waveguide with device height $H = 250$ nm and slab height $h = 150$ nm. A plot of finally settled value of λ_B 's as a function of waveguide width W is shown in Fig. 3.6 Thus for the given device dimension (waveguide and grating dimensions) one can

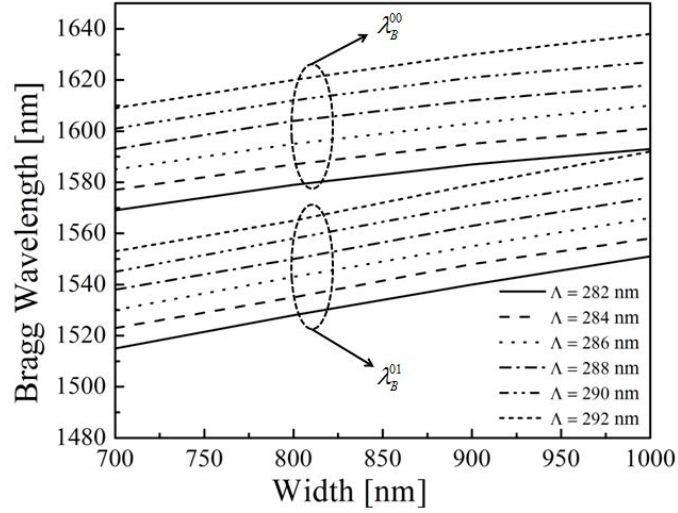


Figure 3.6: Bragg wavelengths (λ_B^{00} , λ_B^{01}) obtained from iterative computation versus waveguide width for different grating periods. The effective indices were calculated for $W = 560$ nm, $H = 250$ nm and $h = 150$ nm.

predict the values of Bragg wavelengths.

3.1.2 REF Device Parameters Optimization

After defining device geometry and discussing about analytical estimations of Bragg wavelength for a grating assisted multimode waveguide, now it is important to select proper device parameters such as waveguide width, slab height, grating period and grating modulation width for a given device layer of $H = 250$ nm SOI substrate within the operating wavelength range $1500 \text{ nm} < \lambda < 1620 \text{ nm}$. Other constraints of optimization are rectangular edge filter device with sharp edge, flat top, high extinction ratio, controllable passband width and minimum waveguide and grating losses.

I. Waveguide width and slab height selection

We have already presented the variation of effective indices of a waveguide with respect to the waveguide parameters in chapter 2. We concluded that no TM mode is guiding for slab height more than or equal to 150 nm in a SOI rib waveguide of device layer

thickness 250 nm. Here, we re-plot effective indices of the guided modes as a function of waveguide width W with slab height h as parameters as shown in Fig. 3.7. There

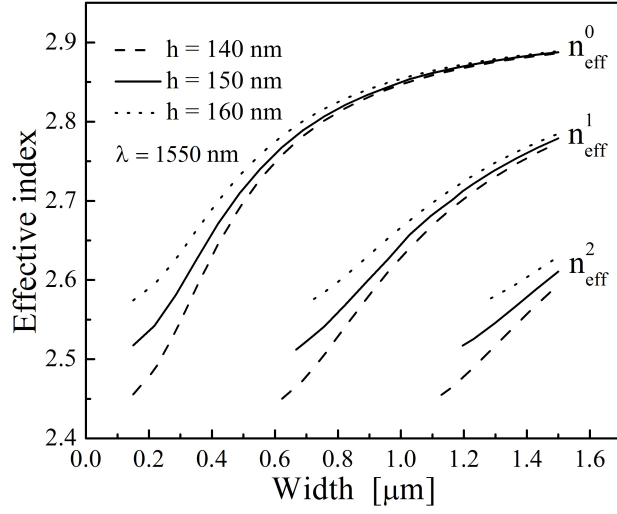


Figure 3.7: Effective indices of the guided modes vs waveguide width (supporting only TE-like guided modes) calculated for a fixed device layer thickness of $H = 250$ nm and slab height as parameter.

exist a cut-off width (W_m^{cut}) for each mode for a given slab height below which only m_{th} and lower than m_{th} order mode(s) guide as confined mode. Table 3.1 gives the value W_m^{cut} for $m = 1$ and 2 at three slab heights. The effective index plot is used for selecting waveguide parameters for designing waveguide of desired number of modes. For example, one can select $W_1 < 650$ nm for the input and output waveguides and $W_2 = W_1 + \Delta W$ between 660 nm and 1000 nm for the waveguide width in the side wall grating region (see Fig. 3.1). As n_{eff}^m varies with W and λ_B^{0m} is the function of n_{eff}^m , so the λ_B^{0m} will vary with W . So the variation of λ_B^{00} and λ_B^{01} as a function of waveguide width ($700 \text{ nm} < W_2 < 1000 \text{ nm}$) has been already shown in Fig. 3.6, keeping grating period Λ as parameters.

Lower value of waveguide width would excite TM mode which in turn would encounter waveguide birefringence. Also higher value of waveguide width are more likely to excite higher order mode(s) as evident from figure 3.7 that for $W > 700$ nm, first order mode also starts guiding. Thus we choose the moderate value $W_1 = 560$ nm for input and output access waveguides width for the proposed design. Another reason of selecting $W_1 = 560$ nm is the smooth transition of effective index of fundamental mode from a single mode waveguide width to a multimode waveguide width. The smooth

transition of effective index of fundamental mode can be seen in the Fig. 3.7 near $W = 600 \text{ nm} - 800 \text{ nm}$ as the slope of the n_{eff} plot reduces within the range. It is observed that effective index of a guided mode increases faster for lower values of W and then saturates at higher values. Thus, for a given value of $h = 150 \text{ nm}$ and $H = 250 \text{ nm}$, we can confirm for a fundamental mode in the input waveguide of width $W_1 \sim 560 \text{ nm}$ propagating in the forward direction would transform smoothly into a forward propagating fundamental mode when it reaches in the grating integrated multi-mode waveguide of width $W_2 = 760 \text{ nm}$.

Table 3.1: Cut-off width of the waveguide for higher order modes calculated for three different values of slab heights h , assuming $H = 250 \text{ nm}$.

Parameters	$h = 140 \text{ nm}$	$h = 150 \text{ nm}$	$h = 160 \text{ nm}$
$W_1^{cut} \text{ [nm]}$	620	665	725
$W_2^{cut} \text{ [nm]}$	1110	1175	1280

Slab height h is defined by dry etching of the device from top side. Higher the etching depth lower will be the h . Very low value of h makes n_{eff}^{00} more sloppy in fundamental mode guidance region which will hamper smooth transition of mode as we discussed earlier. On the other hand, higher value of h would result from shallow etched waveguide in which maximum mode power confinement will be shifted towards slab region. Another reason is that we can not prefer lower etch depth as the etch rate becomes nonuniform in small etch time (plasma formation is not uniform for smaller etching time). That is, obtaining uniform etch rate for shallow etch waveguide is challenging. Thus we again select a value of slab height which is little more than the moderate value, that is $h = 150 \text{ nm}$, keeping in mind that shallow etching would result into lower losses in waveguide and grating regions.

II. Grating period and modulation depth selection

Grating period selection criteria depends upon choice that where the Bragg wavelength. As international telecommunication union (ITU) channels are within optical C and L band, we choose $\lambda_B^{00} \sim 1600 \text{ nm}$ and $\lambda_B^{01} \sim 1550 \text{ nm}$. Thus the required grating period calculated using Eq. 3.2, 3.3, and with the help of look up Fig. 3.4(a) is $\sim 290 \text{ nm}$ for the waveguide width $W = 700 \text{ nm}$. It is now evident that by a proper choice of

waveguide parameters (W_2 , H , and h) and grating period (Λ), we can select the desired value of λ_B^{01} in C-band, while keeping λ_B^{00} at a safe distance in L-band or beyond. However, the Bragg wavelengths are found to be highly sensitive to device dimensions. We will discuss the effect of parameter detuning on the spectral characteristic of the DBR devices later in this Chapter.

We have introduced the general expression of the coupling constant in Eq. 2.19 in Chapter 2. In this chapter, since forward propagating fundamental mode couples to the backward propagating fundamental as well as first order mode, the the expression for the coupling constant (due to first order Fourier coefficient of periodic grating modulation) can be rewritten as

$$\kappa_{0m} = \frac{n_{si}^2 - n_{air}^2}{\sqrt{n_{eff}^0 n_{eff}^m}} \left(\frac{1}{\lambda} \right) \int_{x_1}^{x_2} \int_{y_1}^{y_2} \mathcal{E}_0(x, y) \cdot \mathcal{E}_m(x, y) dx dy \quad (3.6)$$

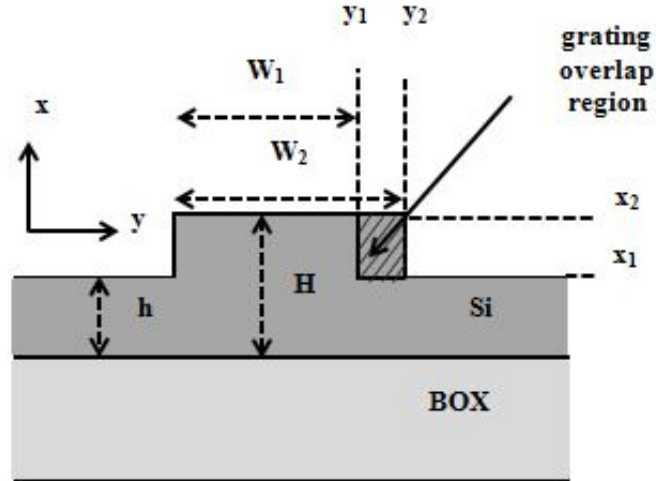


Figure 3.8: Cross section of a SOI rib waveguide with side wall grating at one side (hashed line shows the grating overlap region). The device parameters are defined as: device later thickness H , slab height h and waveguide width W_1 and W_2 with and without grating perturbations respectively.

where limits of integration x_1 , x_2 and y_1 , y_2 are the coordinates in the grating modulation region as shown in Fig. 3.8, \mathcal{E}_0 and \mathcal{E}_m are the normalized transverse field distributions of the 0_{th} order forward propagating mode and m_{th} order backward propagating mode, respectively. We observe that the horizontal span of the limit of integration, that is $|x_2 - x_1|$ is equal to $H - h$ which is actually the waveguide ridge height above the slab or the etch depth of the waveguide and side wall grating. Similarly, the vertical

span of the limit of integration, that is $|y_2 - y_1|$ is equal to ΔW which is actually the side-wall modulation width.

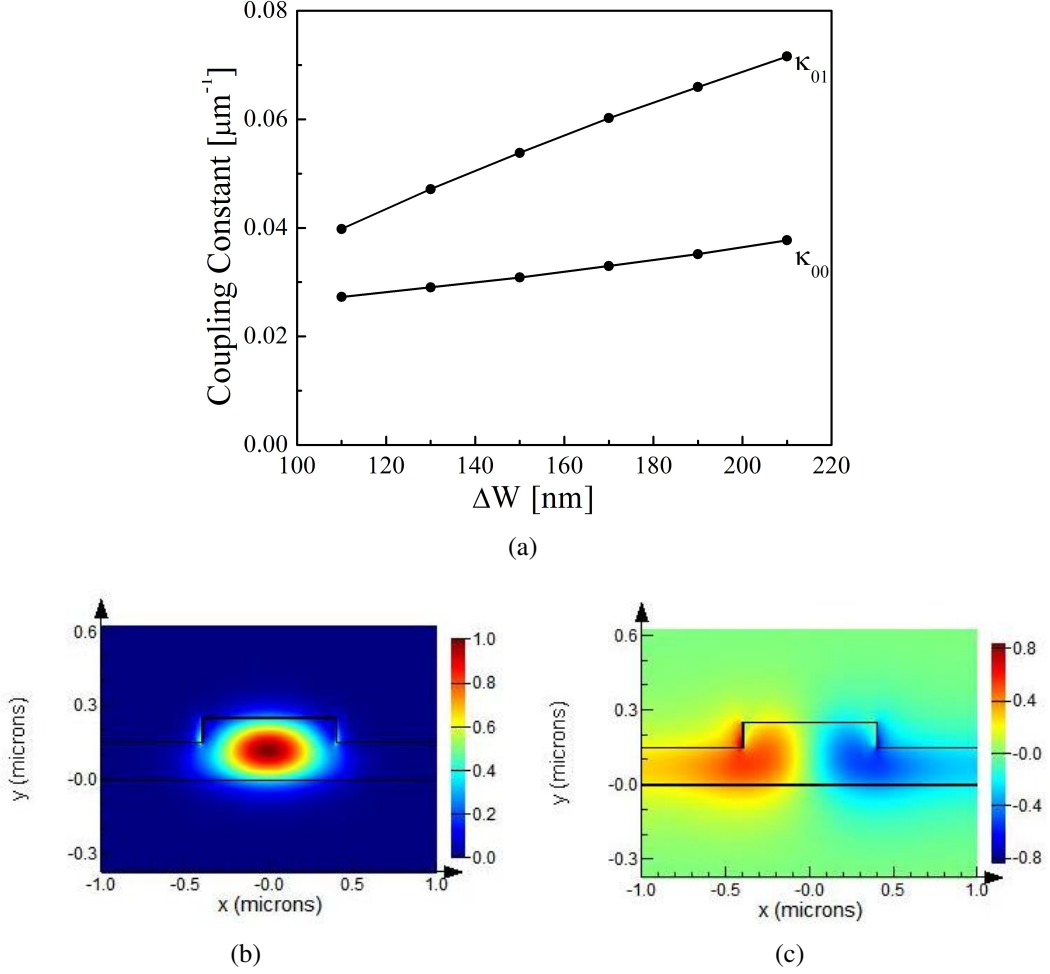


Figure 3.9: (a) Coupling constants κ_{00} and κ_{01} for backward propagating fundamental and first order modes respectively as a function of grating modulation width ΔW . The values are calculated by evaluating mode-field distributions for a waveguide width of $W_2 = W_1 + \Delta W$, where $W_1 = 560$ nm, $H = 250$ nm, and $h = 150$ nm; (b) the distribution of electric field amplitude for the fundamental mode $\mathcal{E}_{0y}(x,y)$; and (c) the distribution of electric field amplitude for the 1st order mode $\mathcal{E}_{1y}(x,y)$, both calculated for $W_2 = 760$ nm.

To evaluate the coupling constant using equation 3.6, we simulated the waveguide cross section using "Lumerical mode solver" for the transverse mode field profiles \mathcal{E}_m and corresponding effective indices n_{eff}^m for the m_{th} order guided mode for a given value of waveguide parameters. Considering $H = 250$ nm, $h = 150$ nm and $W_1 = 560$ nm, we vary the width of the waveguide in grating region $W_2 = W_1 + \Delta W$ from $W_2 = 560$ nm + 150 nm = 710 nm to $W_2 = 560$ nm + 220 nm = 780 nm in the step of 20 nm. Each time we compute the transverse electric field profile and corresponding

effective index for the waveguide width W_2 . Putting the values of the transverse electric field profile and corresponding effective index in the Eq. 3.6 we evaluate the coupling constant x-limit $x_1 = W_1 = 560$ nm to the $x_2 = W_2 = 560$ nm + ΔW . Thus, the evaluated coupling constants $\kappa_{00}at\lambda_B^{00}$ and $\kappa_{01}at\lambda_B^{01}$ for $m = 0$ and 1 in Eq. 3.6 are plotted as a function of grating modulation depth ΔW as shown in Fig. 3.9(a).

We assumed that the transverse electric mode-field distributions in the grating region are not affected by the grating modulation. However, exact field profile and corresponding refractive index can not be found by direct method using eigen mode solver. Since we consider waveguide width as W_2 for the field profile computation, the values of field and refractive index is overestimated in this case. For example, Figs. 3.9(b) and 3.9(c) shows the dominant mode field components $\mathcal{E}_{0y}(x, y)$ and $\mathcal{E}_{1y}(x, y)$ respectively. The Field profiles are computed for $W_2 = 760$ nm, $H = 250$ nm and $h = 150$ nm at $\lambda = 1550$ nm. It can be noticed that the peak intensity of the electric field is concentrated at the center of the waveguide for fundamental mode while the for the first order mode mode, it is concentrated towards the waveguide walls. Since the overlap integration for κ_{0m} calculation is done near the waveguide wall (as grating perturbation is at the side wall), The mode overlap integral will be more for the case of fundamental to first order mode coupling in comparison to that for the case of fundamental to fundamental mode coupling. This in turn would result into $\kappa_{01} > \kappa_{00}$ which is obvious from the Fig. 3.9(a). Relatively stronger field overlap of the first order mode ($m = 1$) with the side-wall grating results into $\kappa_{01} > \kappa_{00}$ as shown in Fig. 3.9(a). Nevertheless, both κ_{01} and κ_{00} increase linearly with the increase of grating perturbations calculated for 110 nm $\leq \Delta W \leq 210$ nm. Although we stated that the backward propagating higher order modes also couple to the forward propagating fundamental mode at some wavelength lower than λ_B^{01} , the actual coupling constants for these modes could not be computed by the above mentioned semi-analytical method accurately as these are non confined modes and no boundary condition will be applied to them and hence no eigen mode solver can compute normalized field distributions for unbounded modes. These leaky modes, thus are also phase matched for wavelengths shorter than λ_B^{01} giving non-zero coupling constant until they leak into the slab at the input waveguide. Since the effective indices of these leaky modes are approximately continuous, the phase matched wavelength will be also approximately continuous. Thus the reflection band for the

wavelengths shorter than λ_B^{01} would result in wider stopband. If such couplings are significantly large and the device is long enough, a wider stop-band associated with a steeper REF response around λ_B^{01} can be expected.

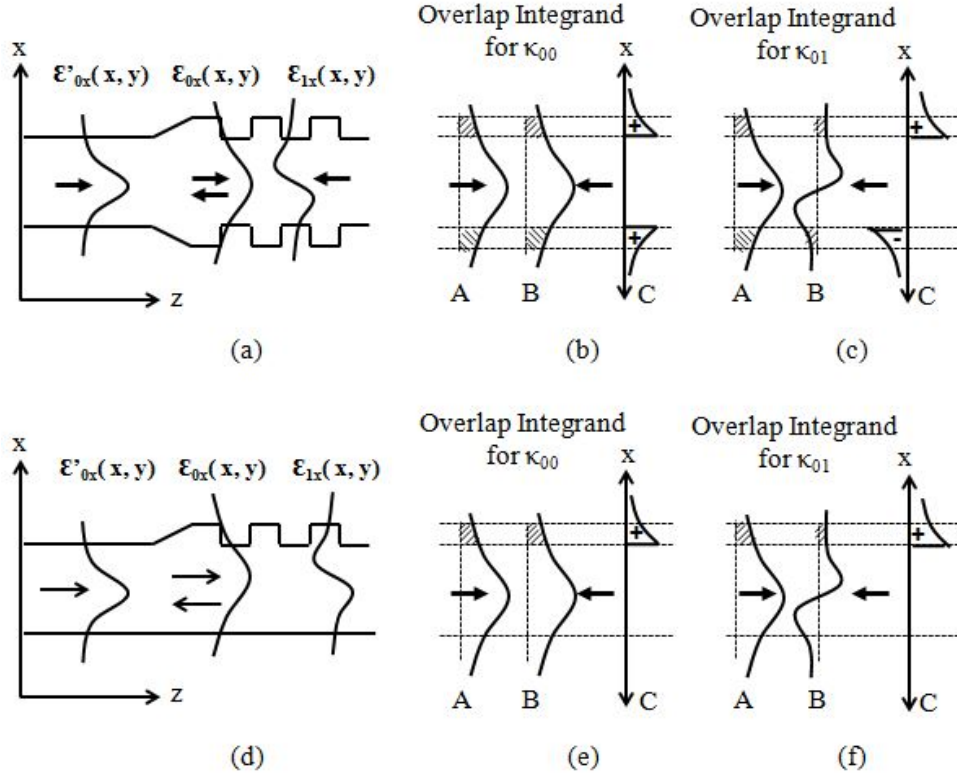


Figure 3.10: Schematic representation of coupling constant κ_{00} and κ_{01} in side wall gratings. (a) symmetric side wall grating with propagating mode field profile, (b) integrand for κ_{00} , (c) integrand for κ_{01} , and (d) asymmetric side wall grating with propagating mode field profile, (e) integrand for κ_{00} , (f) integrand for κ_{01} . The notations represent: A - forward propagating mode, B - backward propagating mode and C - overlap area within the grating modulation region.

What happens to the coupling constant in the case of symmetric side wall grating that is the grating perturbation at both the side walls of the waveguide? Why the asymmetric side wall grating that is grating at one side wall of the waveguide results into the REF device and why not the symmetric side wall grating? To answer these questions, we discuss here the issue with the cartoon representation of the symmetric and asymmetric side wall grating and the coupling constant calculation scheme. Fig. 3.10 shows the cartoon for the same. The symmetric and asymmetric side wall grating (top view) with the mode field distributions $\mathcal{E}'_{0x}(x, y)$, $\mathcal{E}_{0x}(x, y)$ and $\mathcal{E}_{1x}(x, y)$ along x-axis in different regions of waveguide are shown in Fig. 3.10 (a) and 3.10 (d) respectively.

The integrand in the coupling coefficient integral as in Eq. 3.6 for κ_{00} and κ_{01} is graphically represented in Fig. 3.10 (b) and 3.10 (c) respectively for a symmetric side wall grating. Similarly, Fig. 3.10 (e) and 3.10 (f) graphically represent the integrand in the coupling constant integral for κ_{00} and κ_{01} respectively for an asymmetric side wall grating. The notations A, B and C represent the mode field distributions with direction of propagation shown by the arrow head for forward propagating mode, backward propagating mode and overlap area within the grating modulation region respectively. For a symmetric side wall grating, both the forward and backward propagating mode distributions (A and B) are symmetric with respect to the waveguide axis, hence the overlap area within the grating perturbation region i.e. the integrand in the coupling constant integral is positive non-zero value (see 3.10 (a) and (b)). The same result holds for the symmetric side wall grating (see 3.10 (d) and (e)), i.e. $\kappa_{00} \neq 0$. But, for κ_{01} calculation, in a symmetric side wall grating, the forward propagating mode distributions A is symmetric with respect to the waveguide axis while the backward propagating mode distributions B is asymmetric with respect to the waveguide axis, hence resulting into half positive and half negative overlap area setting $\kappa_{01} = 0$ (see 3.10 (a) and (c)). It is interesting to note that the κ_{01} calculation for an asymmetric side wall grating (see 3.10 (d) and (f)), although the mode field profile A and B are of opposite symmetry with respect to the waveguide axis, the overlap area calculated at only one side wall gives the non-zero value of coupling constant i. e. $\kappa_{01} \neq 0$. We have also shown that $\kappa_{01} > \kappa_{00}$ (see Fig. 3.9(a)). This is the reason why an asymmetric side wall grating gives REF response at the wavelength $\lambda = \lambda_B^{01}$.

3.2 Simulation Results

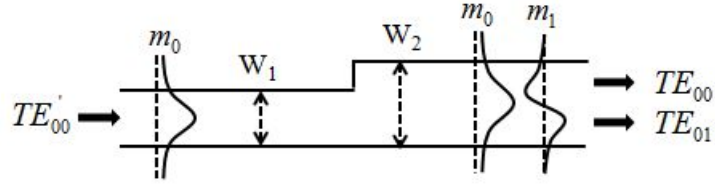
We discussed the design requirements for a REF device and expected filter characteristics qualitatively with the help of semi-analytical method. However the values of effective indices, Bragg wavelengths and coupling constants computed are not accurate. We assumed throughout the calculation that the grating perturbation is not going to change the effective index in the waveguide. However the actual effective index in the grating region would differ due to width variation in the perturbed and unperturbed waveguide region.

The average waveguide width i.e. $W = \frac{1}{2}(W_1 + W_2)$ could possibly predict the actual refractive index in the grating region, but for coupling constant calculation, the average waveguide width can not be considered as the transverse electric field profile need to be computed at W_2 . But this method can predict the nature of the wavelength spectrum and provide a comparative values of coupling constant between κ_{00} and κ_{01} , and their dependency on the waveguide and grating parameters. The actual wavelength characteristic can be given by numerical method of solving Maxwell equations under certain boundary conditions.

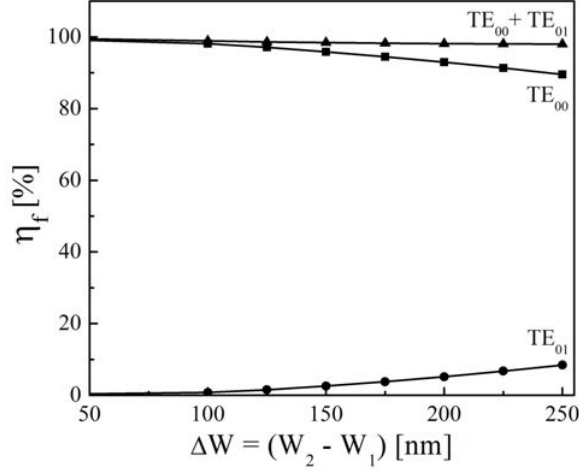
3.2.1 Adiabatic Taper Design

Input/output waveguide width differ to the DBR waveguide width by an amount equal to the grating modulation width ΔW . Higher value of ΔW causes higher value of coupling constant to result into higher reflectivity and larger bandwidth of reflected wave. However, due to mismatch between waveguide widths at the interface of input/output waveguides and DBR waveguide, refractive index mismatch will occur causing the ripples near the reflection and transmission filter edge. As stated earlier, an adiabatic taper between the input/output and DBR waveguide would reduce the mode power conversion from fundamental mode to any other higher order mode(s). The same adiabatic taper would reduce the unwanted ripples by providing index matching between the input/output and DBR waveguide. To estimate the forward modal power coupling efficiency (η_f) from the single-mode (input/output waveguide) to multi-mode waveguide region (DBR waveguide), we have carried out 3D FDTD simulations.

Fig. 3.11(a) shows the schematic of the top view of step transition in waveguide width connecting input/output waveguide to grating region showing possible mode field profiles; m_0 - mode field profile for fundamental mode and m_1 - mode field profile for first order mode. The value of η_f corresponding to percentage of power shares for forward propagating fundamental mode (TE_{00}), 1st order mode TE_{01} , and their sums as a function of ΔW (for $W_1 = 560$ nm) is shown in Fig. 3.11(b) for the abrupt transition in waveguide width (without linear taper) corresponding to Fig. 3.11(a). It is observable from the figure that as the step transition width difference ΔW increases the conversion



(a)

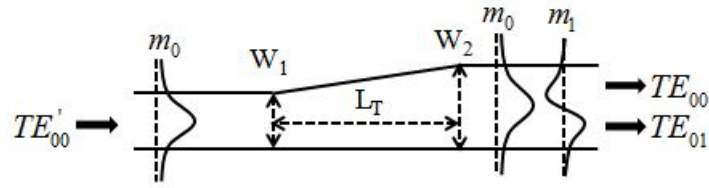


(b)

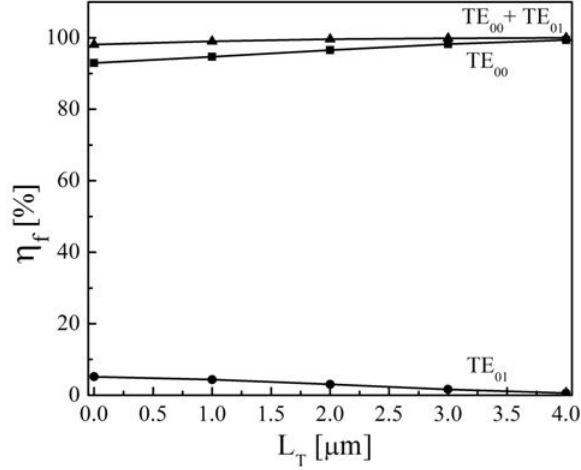
Figure 3.11: (a) Schematic of step transition in waveguide width connecting input/output waveguide to grating region and (b) power coupling efficiency into forward propagating fundamental and 1st order modes, and their sums as a function of ΔW for abrupt junction with $W_1 = 560$ nm.

of fundamental mode power into first order mode power increases. For example, at $\Delta W = 200$ nm, 5% of total incident power from the single-mode waveguide is coupled into the forward propagating first order mode and only remaining 95% of total incident power from the single-mode waveguide is coupled into the forward propagating fundamental mode (assuming no other loss).

However, a linear taper waveguide connecting input/output waveguide to DBR waveguide of sufficient length can reduce this power conversion completely. We simulate structure of fixed ΔW of 200 nm and varying the taper length L_T connected in between the waveguide of width W_1 and W_2 (see Fig. 3.12(a)). For each L_T , we again compute the η_f for forward propagating fundamental mode (TE_{00}), 1st order mode TE_{01} , and their sums as a function of ΔW (for $W_1 = 560$ nm). We increase the value of L_T till the power conversion from fundamental mode to first order mode reduces approximately to zero. For example, a taper of length $L_T = 4 \mu\text{m}$ is sufficient for an adiabatic transition



(a)



(b)

Figure 3.12: (a) Schematic of step transition in waveguide width connecting input/output waveguide to grating region and (b) power coupling efficiency into forward propagating fundamental and 1st order modes, and their sums as a function of taper length L_T between $W_1 = 560$ nm and $W_2 = 760$ nm.

of incident fundamental mode (TE_{00}) into a forward propagating fundamental mode (TE_{00}); i.e., $\sim 100\%$ power couples to the forward propagating fundamental mode (see Fig. 3.12). Since the role of tapering is not significant for $\Delta W \leq 200$ nm, we have ignored the input/output transition regions for simulating transmission characteristics of the proposed REF device using 3D FDTD method.

3.2.2 FDTD Simulations

To validate the semi-analytical study of REF device we present here the 3D FDTD simulations. The device as given in Fig. 3.1(a) was considered for FDTD simulation with the waveguide and grating parameters tabulated in Table 3.2. We used the "Lumerical FDTD Solutions" for the simulation the device with the simulation parameters as given Table 3.3. Actual grating length is considered as $500 \mu\text{m}$ but for FDTD simulation we

Table 3.2: REF device parameters of waveguide and grating used for FDTD simulation

Waveguide Parameters			Grating Parameters		
W_1 [nm]	H [nm]	h [nm]	Λ [nm]	ΔW [nm]	L_g [μm]
560	250	150	290	200	500

simulated only for $L_g = 100 \mu\text{m}$ just for keeping time and memory resources economized. The internal simulation time of the FDTD is decided by the time taken by the light to travel the distance along the device from source to monitor. It is generally expressed in femto second (fs) unit. For the device having resonance, the group velocity of the light reduces hence increasing the higher simulation time requirement. So we have considered large value of internal simulation time as 15000 fs to obtain the error free simulation results. The source calculates the mode and launches the fundamental mode in the waveguide. The monitor time domain pulse into a frequency domain using discrete Fourier transform and stores the transmitted power in 1000 frequency (or wavelength) points.

Table 3.3: FDTD simulation parameters

Parameters	Specification
Boundary condition:	PML (perfectly matched layer)
Source:	3D mode source
Monitor:	Frequency domain field and power monitor
Mesh type:	Auto non-uniform
Minimum mesh step:	0.25 nm
Time step:	0.0585787 fs

We first simulate the symmetric side wall grating with grating modulation at both side walls of the multimode waveguide with the parameters as given in Table 3.2. The schematic for the symmetric side wall grating is shown in Fig. 3.13(a). The transmission and the reflection spectrum is shown in Fig. 3.13(b) and 3.13(c) respectively. Ideally, $\kappa_{01} = 0$ and no λ_B^{01} should exist in transmission. But we observe λ_B^{01} at ~ 1520 nm with larger bandwidth with very less transmission of about 20 %. However, the reflected wave around $\lambda = 1520$ nm leaks into slab completely before reaching in the input waveguide where we have placed the reflection monitor. It can be seen in Fig. 3.13(c) that no reflection is observed around $\lambda = 1520$ nm. There exist zero transmis-

sion and more than 99 % reflection at $\lambda_B^{00} \sim 1605$ nm. This reflection is in the form of fundamental mode which guides well in the input waveguide and hence is recorded by the DFT monitor. But we do not prefer this design for REF device as it does not give rectangular edge at λ_B^{01} as we discussed in the theoretically.

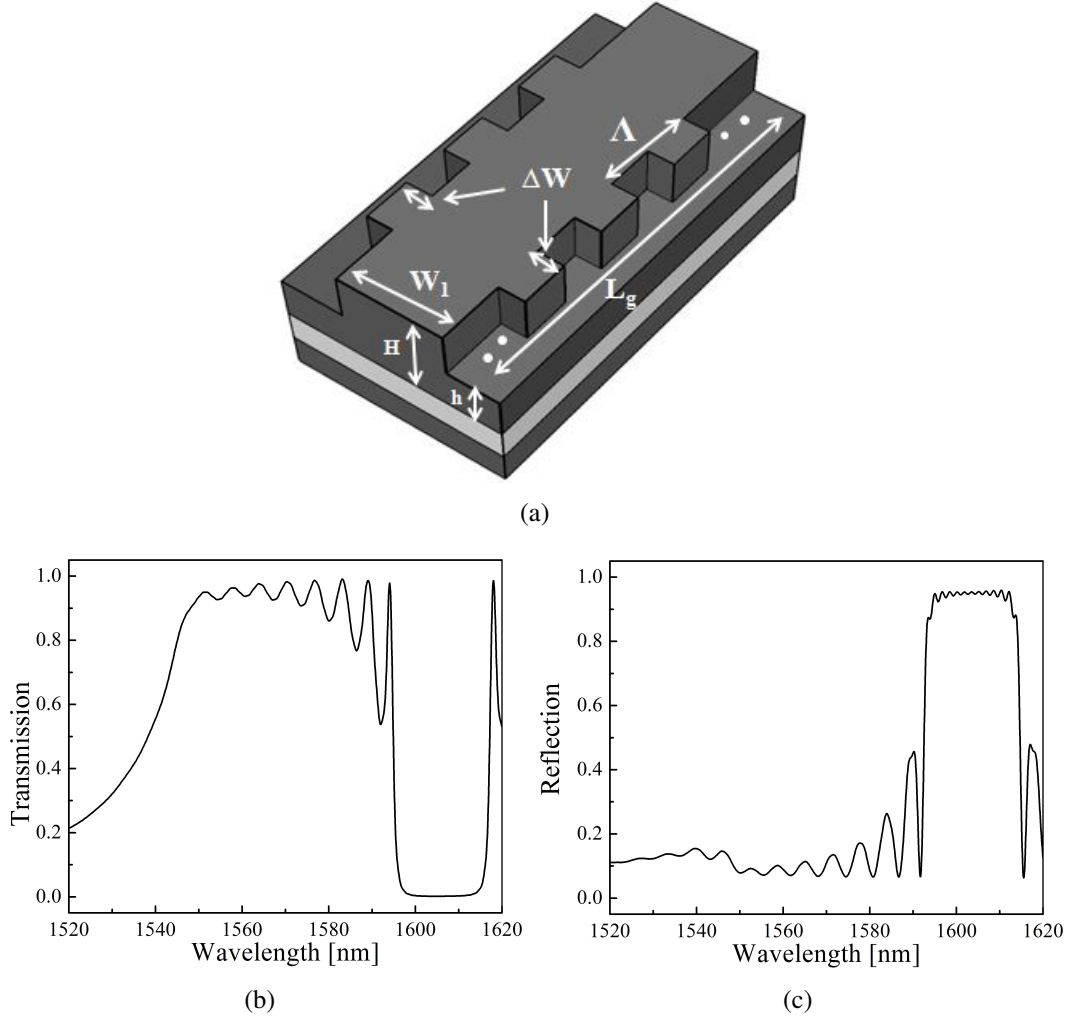
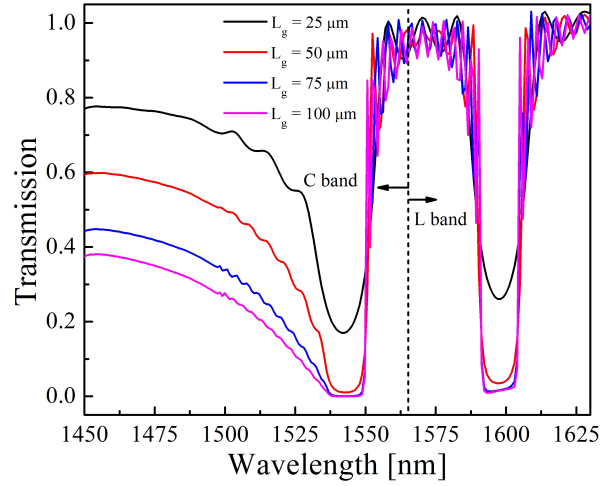


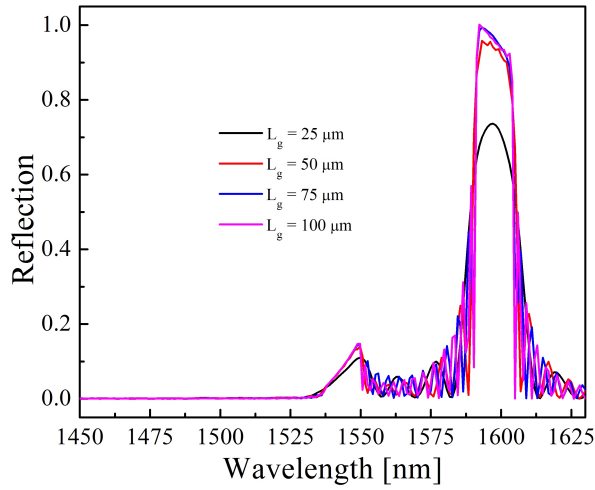
Figure 3.13: (a) 3D schematic of a symmetric side wall grating. FDTD simulation spectrum for a symmetric side wall grating: (a) transmission spectrum, (b) reflection spectrum. The parameter values used for the simulation are $W_1 = 560$ nm, $H = 250$ nm, and $h = 150$ nm, $\Delta W = 200$ nm, $\Lambda = 290$ nm, $L_g = 100$ μm .

So we consider the simulation of an asymmetric side wall grating i.e. the grating at only one of the side walls of the multimode waveguide. The device design can be referred to the Fig 3.1(a). The device parameters are the same as given in Table 3.2 except for grating length L_g varied as 25 μm , 50 μm , 75 μm and 100 μm .

Fig. 3.15 shows the simulated transmission and reflection spectrum for all the four



(a)



(b)

Figure 3.14: FDTD simulation for four different device lengths: (a) transmission spectrum, (b) reflection spectrum. The parameter values used for the simulation are $W_1 = 560$ nm, $\Delta W = 200$ nm, $H = 250$ nm, and $h = 150$ nm.

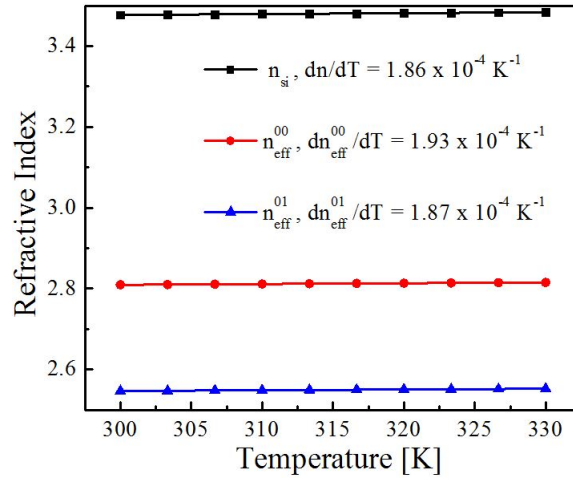
grating lengths. Since $\kappa_{01} \neq 0$ for the asymmetric side wall grating, λ_B^{01} exists in transmission with very less transmission $\sim 0\%$ for $L_g = 100$ μm at $\lambda_B^{01} \sim 1542$ nm within optical C-band (see Fig. 3.14(a)). Also the filter edge to the right side of λ_B^{01} rolls off sharply as the L_g increases. At even higher value of L_g (say $L_g = 500$ μm , which is not possible to simulate as it need very high memory size and simulation time) the edge slope would increase as if it would result into step like shape or rectangular edge shape. As usual the reflected wave around λ_B^{01} 1542 nm leaks into slab completely before reaching in the input waveguide and hence is not recorded by the reflection monitor as it can be seen in Fig. 3.14(b). However, the wavelength $\lambda_B^{00} = 1600$ nm is

absent from transmission and present in reflection for the reason described for the case of symmetric side wall grating. The small peaks at λ_B^{01} in reflection spectra is captured in the power monitor due to backward propagating leaky modes as the power monitor was placed in the input access waveguide but adjacent to device junction point. This would not be appeared if the backward reflected wave is allowed to propagate inside longer distance in the input access waveguide by availing wider computation window. We also observe a delay free transmission band of ~ 50 nm between the two Bragg wavelengths. To the left side of the edge wavelength $\lambda_{edge} \sim \lambda_B^{01}$, a wide stopband results possibly due to the higher order mode coupling in the backward direction as we discussed qualitatively in device theory section. Comparing the transmission intensity at λ_B^{01} and λ_B^{00} we observe from Fig. 3.14(a) that the transmission at λ_B^{01} is deeper than that at λ_B^{00} (it is more visible in logarithmic scale). This is in accordance to the theory as predicted by the semi-analytical calculations that $\kappa_{01} > \kappa_{00}$ as shown in Fig. 3.9(a). Moreover, the transmission deeps and the reflection peak become stronger and stronger for longer grating lengths which is also consistent with the coupled mode theory; reflectivity at Bragg wavelength λ_B^{0m} is given by $R = \tanh^2(\kappa_{0m}L_g)$. Thus for a sufficiently longer device length, the expected REF response can be obtained around λ_B^{01} in the transmission spectrum.

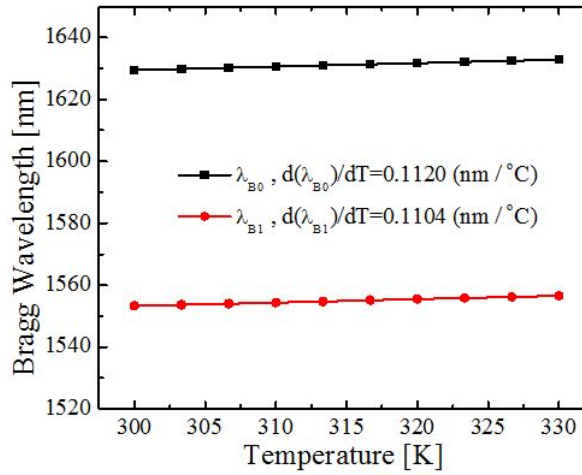
We cross verified results obtained from the FDTD plot with the value obtained in semi-analytical method. For this, we calculate back the values of the effective indices n_{eff}^0 and n_{eff}^1 solving the Eq. 3.4 and 3.5 simultaneously with $\lambda_B^{01} = 1542$ nm and $\lambda_B^{00} = 1598$ nm. We obtain the values of n_{eff}^0 and n_{eff}^1 as 2.76 and 2.56, respectively. These values are then compared with the effective index calculations using eigenmode solver. We have shown the effective index calculations in Fig. 3.7 where we do not consider grating perturbation. Using Fig. 3.7, we tried to compute back the value of waveguide width corresponding to the the effective indices extracted in FDTD. We obtained two different values of the W_2 corresponding to each n_{eff} . This mismatch can be attributed to the altered effective waveguide width and altered dispersion characteristics of the device because of strong grating perturbation ($\Delta W = 200$ nm).

3.2.3 Thermal Detuning

Silicon (the waveguide core) and SiO₂ (waveguide cladding) are thermo-optically active and their thermo-optic coefficients are $1.86 \times 10^{-4}/\text{K}$ and $1.2 \times 10^{-5}/\text{K}$ respectively. The effective index of the guided mode(s) can be increased by heating the sample by integrating micro-heater along with the device or by direct heating by increasing the ambient temperature. The ambient temperature can not provide heat to component se-



(a)



(b)

Figure 3.15: (a) Effective indices versus waveguide temperature plot and (b) Bragg wavelength versus waveguide temperature plot for a SOI rib waveguide with parameters: $W = 760$ nm, $H = 250$ nm and $h = 150$ nm. The calculation was done along a fixed cross section.

lectively. Also, controlling ambient temperature may not be precise and accurate for heating the component on silicon chip. So fabrication of integrated microheater is gen-

erally preferred over the direct heating. Since the wavelength characteristics of the REF device like Bragg wavelength is proportional to the effective refractive indices of the guided modes, we compute the rate of change of guided mode effective indices as a function of temperature using the eigenmode solver. Fig. 3.15(a) shows the variation of the effective indices with respect to temperature of silicon waveguide. Both the effective indices varies linearly with temperature with an average slope approximately comparable to thermo-optic coefficients of silicon. As Bragg wavelengths depend on effective indices which in turn depend on temperature, both λ_B^{00} and λ_B^{01} are plotted versus temperature of the waveguide as shown in Fig. 3.15(b). The average temperature slope of both the Bragg wavelengths are approximately equal to 0.11 nm/°C. This means that a temperature change of ~ 9 °C would shift the Bragg wavelength by ~ 1 nm. In order to validate this semi-analytical study of temperature effect on device characteristic, we carried out 3D FDTD simulation for the device parameters as given Table 3.2 at two different temperatures: $T = 300$ K and 327 K. The corresponding transmission characteristic (in dB scale) is shown in Fig. 3.16. There is a red shift of ~ 2.2 nm

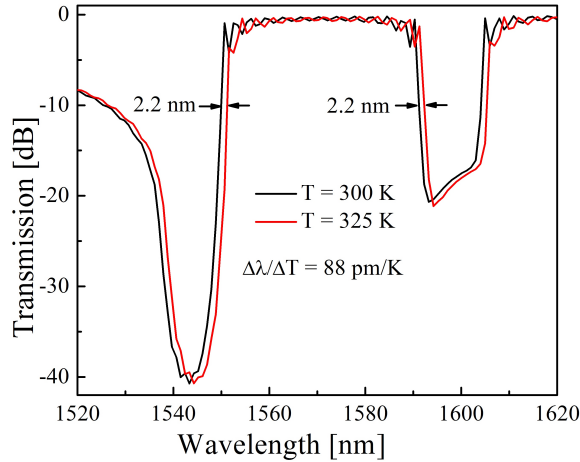


Figure 3.16: Transmission characteristics (obtained by FDTD simulation) at two different temperatures: $T_1 = 300$ K and $T_2 = 325$ K.

in the whole spectrum for a temperature change of 25 K. The wavelength edge ($\lambda_{edge} \sim \lambda_B^{01}$) of the REF is also shifting with the same amount and the edge slope of temperature is calculated to be $\frac{d\lambda_{edge}}{dT} = \frac{d\lambda_B^{01}}{dT} \approx \frac{d\lambda_B^{00}}{dT} \sim 88$ pm/K. Using these slope values and Eq. 3.4 and 3.5, we back calculated the effective indices slope of temperature as $\frac{dn_{eff}^0}{dT} \approx \frac{dn_{eff}^1}{dT} \sim 1.52 \times 10^{-4}/K$. This value differs from that which we computed using semi-analytical method using eigenmode solver. The difference can be attributed to the

altered values of effective indices due to strong grating perturbations as we considered an unperturbed waveguide for effective index calculations.

3.2.4 Effect of Cladding Material

Another way of effective index tuning is to change the cladding material of the waveguide. As the refractive index of cladding material increases, the effective index of guided mode also increases. Hence we should expect a red shift in wavelength characteristic of the DBR device as the Bragg wavelengths are effective index dependent. We simulate the REF device (with the device parameters given in Table 3.2) first with air cladding and then with deionized (DI) water cladding at the top of the waveguide carried out at room temperature $T = 300$ K. The absolute refractive index of the top cladding i.e. air and DI water are 1.0 and 1.318 respectively @ $\lambda \sim 1550$ nm. Fig. 3.17 shows the transmission characteristics of the device with top cladding material as air (black colour) and DI water (red colour). We do observe that the transmissions at

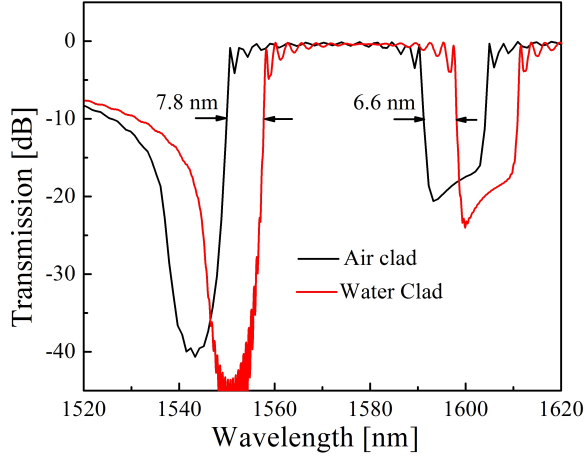


Figure 3.17: Transmission characteristics (obtained by FDTD simulation) by varying top cladding material as air (in black) and water (in red). The parameters used for the device are $W_1 = 560$ nm, $\Delta W = 250$ nm, $H = 200$ nm, and $h = 150$ nm.

Bragg wavelengths ($\lambda_B^{00} \sim 1605$ nm and $\lambda_B^{01} \sim 1550$ nm) are reduced significantly, clearly indicating increased modal overlaps due to DI water cladding. As expected, we also observe a red-shift of $\Delta\lambda_{edge}^{01} = 7.8$ nm and $\Delta\lambda_B^{00} = 6.6$ nm, respectively. The corresponding changes in effective refractive indices are estimated as $\Delta n_{eff}^0 = 1.14 \times 10^{-2}$ and $\Delta n_{eff}^1 = 1.55 \times 10^{-2}$, using Eq. 3.2 and 3.3. Nevertheless, the above simulation

results infers that the device can also be used as a refractive index sensor with an estimated sensitivity (assuming linear red-shift) of $S_\lambda = \frac{\Delta\lambda_{edge}}{\Delta n_c} = 24.5$ nm/RIU and 21 nm/RIU for the Bragg wavelengths at λ_B^{01} and λ_B^{00} , respectively.

From the simulated results discussed above, we also noted that the slope of the transmitted power w.r.t. wavelength increases with the increase of device length (see Fig. 3.17). This is an important figure of merit of a rectangular-edge filter for various applications such as light intensity based sensing, modulation, switching, etc. Though we have not studied this theoretically for longer device lengths (for $L_g > 100$ μm) because of heavy computational budget, we have established it experimentally by fabricating longer grating lengths which is describe in the following section.

3.3 Experimental Results and Discussions

3.3.1 Fabrication

The layout of the mask geometry (designed using same Raith NANOSUITE as we described in Chapter 2, Section 2.3) of DBR and waveguide is shown in Fig. 3.18. The total area of the each mask is 5.5 mm \times 3.5 mm (the aspect ratio shown is not the same as actual one). The DBR at one of the side walls of the waveguide with period $\Lambda = 290$ nm, grating length of 500- μm was integrated between the input/output waveguides. We kept the grating modulation width (ΔW) constant at 200 nm in one set of mask layout as shown in Fig. 3.18(a). It has 9 DBR devices with $\Delta W = 200$ nm, two straight waveguide with $\Delta W = 0$ nm (reference waveguide). We also varied the grating modulation ΔW from 150 nm to 200 nm, in steps of 10 nm in another set of mask layout as shown in Fig. 3.18(b) to study the edge-slope in REF characteristics. It has 6 DBR devices with $\Delta W = 150$ nm to 200 nm, in steps of 10 nm, two straight waveguide with $\Delta W = 0$ nm. we kept these reference waveguides along with the grating device in the mask layout in order to calculate the grating loss, as well as to normalize the DBR characteristics. The mask for the alignment markers and grating couplers are same as we discussed in Chapter 2, Fig. 2.21(b) and 2.21(c) respectively.

Fig. 3.19 shows the zoom-in view of the DBR with $\Delta W = 150$ nm and 200 nm.

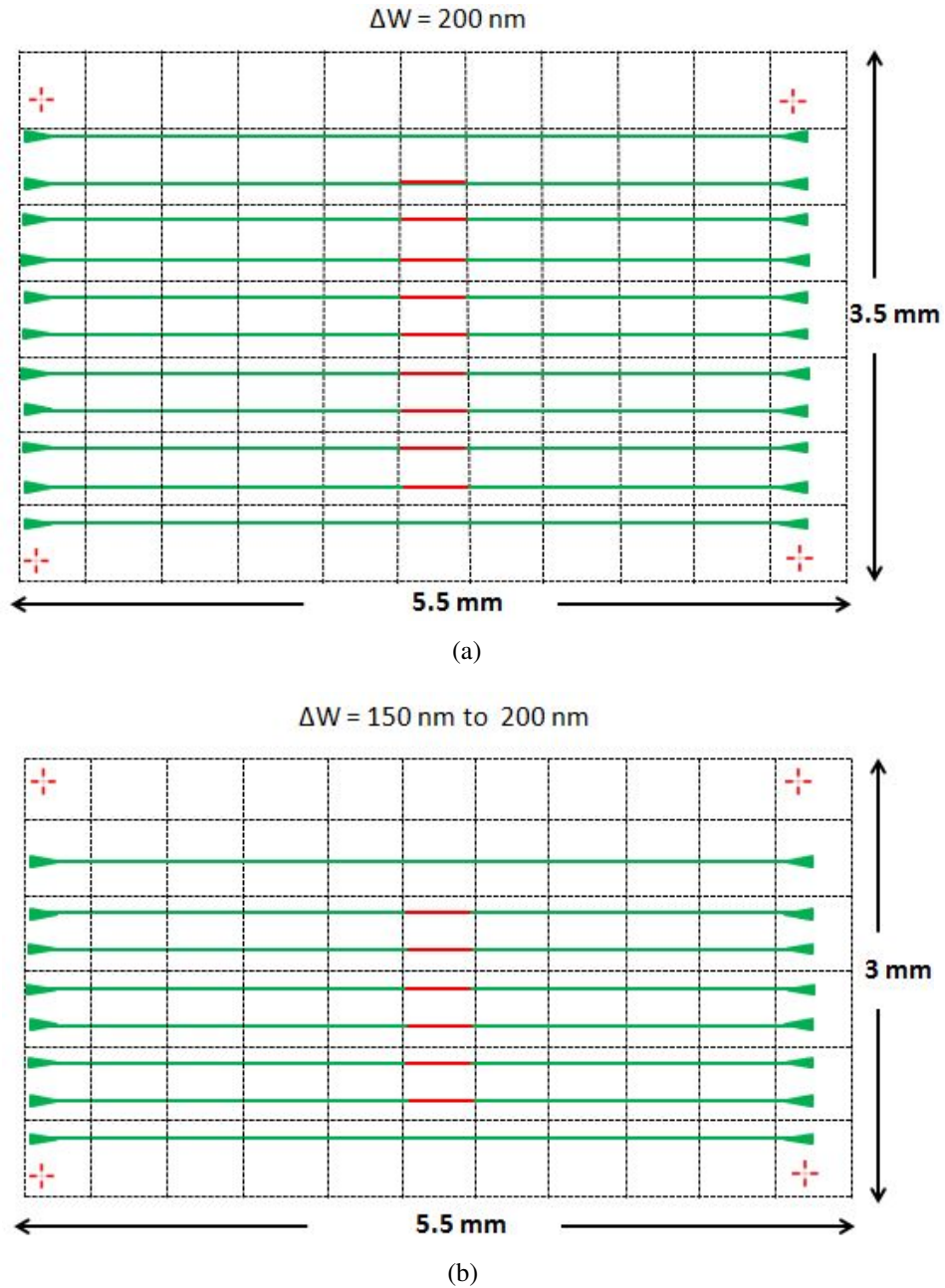
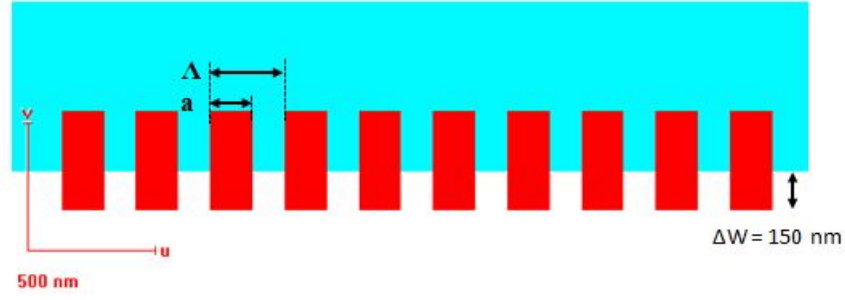
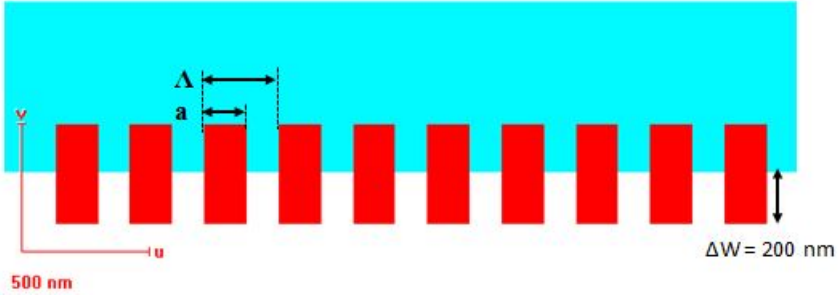


Figure 3.18: Mask layout of REF devices, green colour represents straight waveguide interfaced with input/output grating couplers, red colour in the middle of devices represents the DBR (a) with $\Delta W = 200 \text{ nm}$ (10 devices) and $\Delta W = 0 \text{ nm}$ (two devices), (b) with $\Delta W = 150 \text{ nm to } 200 \text{ nm}$ in the step of 10 nm (six devices) and $\Delta W = 0 \text{ nm}$ (two devices).

The grating pitch and period are shown by "a" and Λ respectively. The grating duty ratio or fill factor defined by $\frac{a}{\Lambda}$ was taken as $160 \text{ nm}/290 \text{ nm}$ i.e. equal to 55 %. Using repeated fabrication, we observed that the final duty ratio after fabrication becomes 50 %. Waveguide width in the mask was defined as 660 nm such as after e-beam patterning and sample development the width reduces approximately 50 nm from each



(a)



(b)

Figure 3.19: Mask layout of REF devices, green colour represents straight waveguide, red colour bars represents the DBR (a) with $\Delta W = 150$ nm and (b) with $\Delta W = 200$ nm.

side resulting into a final width of ~ 560 nm.

The optical grade SOI substrate with a device layer thickness of 250 nm, buried oxide layer thickness of $3 \mu\text{m}$, and handle wafer thickness of $500 \mu\text{m}$ was chosen for fabrication of the REF devices. $12 \mu\text{m} \times 12 \mu\text{m}$ grating coupler with period $\Lambda_{GCi} = \Lambda_{GCo} = 610$ nm were integrated at the both the end of a 5-mm-long single-mode rib waveguides ($W = 560$ nm, $H = 250$ nm, and $h = 150$ nm). The $12 \mu\text{m}$ width of grating coupler is adiabatically tapered down to waveguide width of 560 nm with a taper length of $100 \mu\text{m}$.

The device fabrication process steps and process parameters for REF device are similar to that which we explained in Chapter 2, section 2.3. We imaged the fabricated device with SEM. Although we fabricated the REF devices with ΔW of 150 nm, 160 nm, 170 nm, 180 nm, 190 nm and 200 nm, only the SEM images of a reference waveguide (top view), the DBR device (top view) with $\Delta W = 150$ nm and 200 nm are shown in Fig. 3.20(a), 3.20(b) and 3.20(c), respectively as the difference of 10 nm in grating modulation width can not be resolved with our eyes. We can clearly observed that the

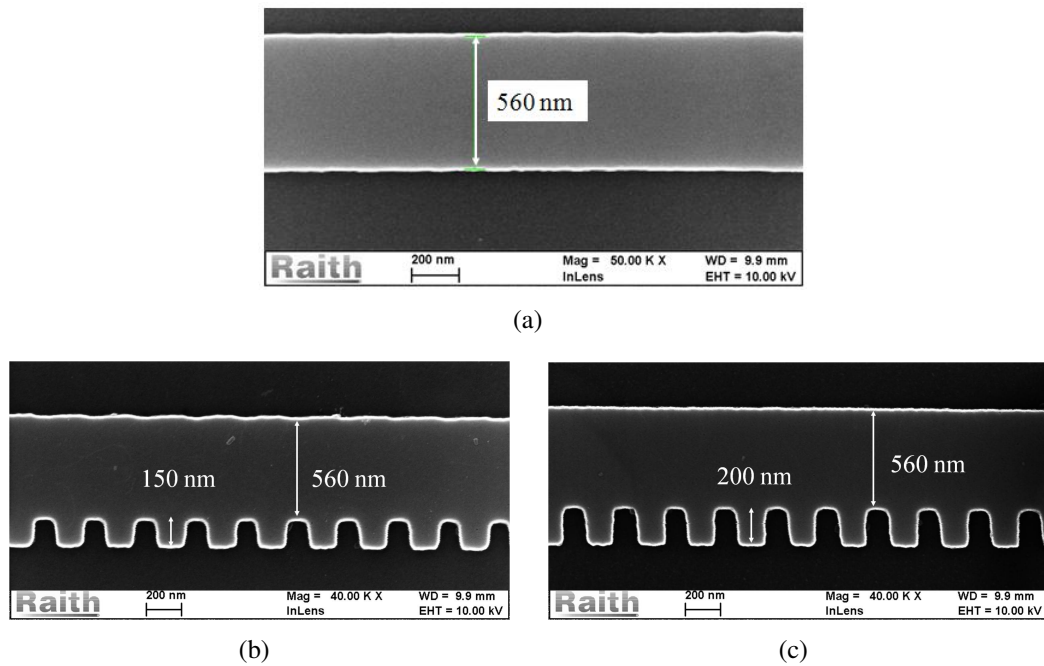


Figure 3.20: SEM images showing top view of rib waveguide ($W = 560$ nm, $H = 250$ nm, and $h = 150$ nm) with side-wall grating modulation: (a) $\Delta W = 150$ nm, and (b) $\Delta W = 200$ nm

waveguide width reduced from 660 nm (in mask layout) to ~ 560 nm after fabrication. Also the duty ratio of the gratings became almost 50 % in the fabricated devices. The fabricated REF devices were characterized using the same characterization setup as we discussed in Chapter 2, Section 2.3, Fig. 2.28. The procedures of the experiment are also the similar as we described in Chapter 2, Section 2.3. So here we directly analyze the experimental results.

3.3.2 Experimental Results

In order to check the device dimension repeatability and the spectral characteristic reproducibility, we fabricated the DBR device several time. The experiment were repeated several time to see any spectral shift in the wavelength characteristics of the devices due to ambient temperature (around 25°C) and due to the internal fluctuations in the laser due to thermal and short noise. Some random shift in spectral characteristics with approximately zero root mean square error were found. These random shift in the order of some pico-meter can be neglected for some applications. However, if the shifts are more then active feedback control circuit can be used externally [102].

A reference waveguide and a grating device with $\Delta W = 200$ nm as shown in SEM image 3.20(a) and 3.20(c), respectively were characterized within optical C and L band of wavelength. Out of several such characteristics, Fig. 3.21 shows one of them. As

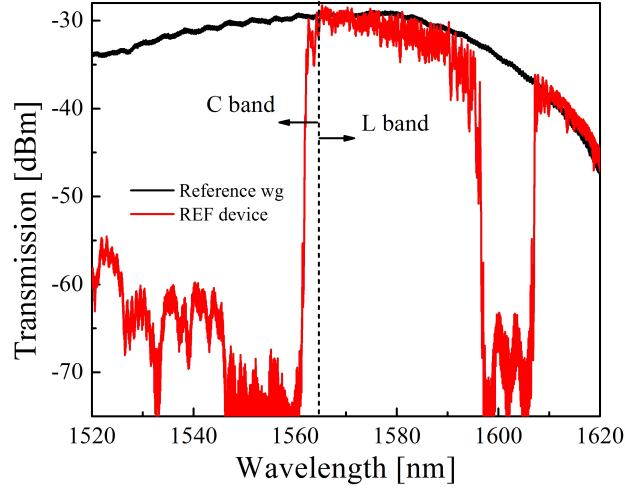


Figure 3.21: Typical transmission characteristics of a REF device with $L_g = 500$ μm , $\Delta W = 200$ nm (red), and that for a reference waveguide without DBR grating (black).

expected from theoretical analysis, the transmission spectrum of the REF device exhibits two stopbands centered at two Bragg wavelengths ($\lambda_B^{00} = \sim 1550$ nm and $\lambda_B^{01} = \sim 1600$ nm). The passband occurring between the two stopbands is ideally flat top passband response. However some ripples at the both edges of the passband can be accounted for impedance mismatch arising due to abrupt junction between multimode grating waveguide and single mode input/output waveguides. However an adiabatic taper connecting grating waveguide to input/output waveguides can minimize impedance mismatch, hence reducing the unwanted band edge fluctuations. The schematic design diagram and theoretical analysis of such a taper have been already presented in section.

The transmission spectrum of the REF device as shown in Fig. 3.21 exhibits a sharp-edge response at $\lambda_{edge} \sim 1560$ nm (inside C-band) and a DBR response at $\lambda_B^{00} \sim 1602$ nm (inside L-band) As expected. The average insertion loss of the grating device can be found by comparing the spectral intensity of grating device with that of a reference waveguide. Comparing the transmission characteristics between reference waveguide and the REF device, we can infer that there is an insertion loss of REF which is ~ 1 dB for $1561 \text{ nm} < \lambda < 1590 \text{ nm}$, whereas almost no insertion loss is observed for $\lambda > 1605$ nm. According to theory and FDTD simulation results, there exist continuous stopbands

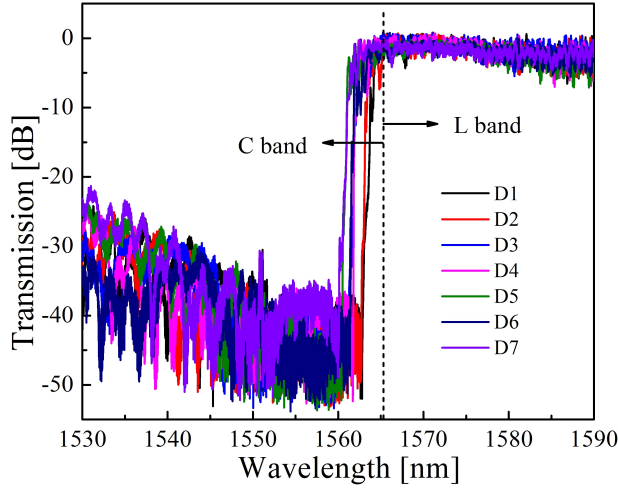


Figure 3.22: Normalized edge-filter characteristics (in C-band) of seven different REF devices (D1 to D7) each fabricated with $L_g = 500 \mu\text{m}$, and $\Delta W = 200 \text{ nm}$ each.

to the left side of the left edge of the rectangular edge filter. So we observe the band rejection of $> 20 \text{ dB}$ for $\lambda < \lambda_{edge} = 1560 \text{ nm}$. Passband to stopband extinction ratio depends on the extent mode coupling constant at phase matched wavelengths. One can notice from Fig. 3.21 that the stop-band extinction at λ_B^{00} ($\sim 35 \text{ dB}$) is lower than that for $\lambda \sim \lambda_B^{01} < \lambda_{edge}$ ($\sim 40 \text{ dB}$), which justifies the theoretical predictions as $\kappa_{01} > \kappa_{00}$.

The ultra-sharp roll-off of the filter can be applicable in Raman or microwave photonics. Fig. 3.21 shows edge-extinction of 40 dB , which can be further improved by incorporating longer length ($> 500 \mu\text{m}$) of grating with larger grating modulation width ($> 350 \text{ nm}$). However, write-field of the e-beam limits longer grating patterning as discussed in section 2.3.2, while large grating modulation width introduces losses in the device characteristics.

Fig. 3.22 shows transmission characteristics (normalized with reference waveguide) for $1530 \text{ nm} \leq \lambda \leq 1590 \text{ nm}$ of seven different REF devices (D1 to D7) each fabricated with $\Delta W = 200 \text{ nm}$. It is evident that all the devices are exhibiting sharp-edge filter response in C-band ($\lambda_{edge} \sim 1561 \pm 1 \text{ nm}$) with an extinction of $> 40 \text{ dB}$. The variation in wavelength edge λ_{edge} is attributed to the variations in waveguide dimensions (W , H , h , and ΔW) resulting out of the process induced errors.

The filter characteristic for six different REF devices (D8 to D13) with $\Delta W = 150 \text{ nm}$, 160 nm , 170 nm , 180 nm , 190 nm , and 200 nm , respectively are shown in Fig.

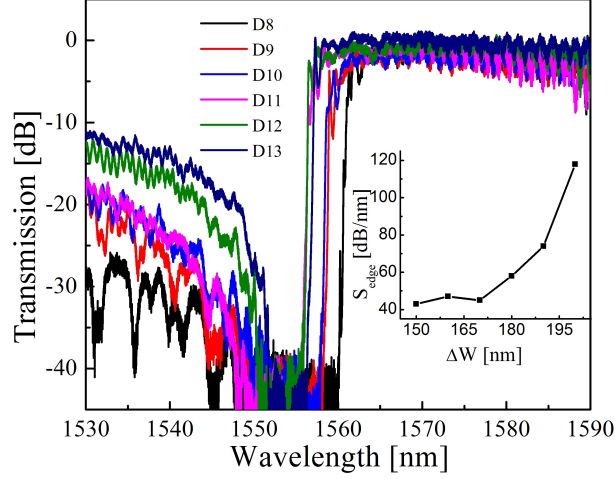


Figure 3.23: Normalized transmission characteristics of six REF devices (D8 to D13) with ΔW varying from 150 nm to 200 nm in steps of 10 nm (each devices has DBR length $L_g = 500 \mu\text{m}$). Inset: slope of the transmitted power $S_{edge} = \frac{dP_T}{d\lambda}$ as a function of ΔW estimated at -20 dB transmission at the edge.

3.23. As expected from the previous discussions, the value of λ_{edge} (~ 1560 nm) is not same for all the devices; however, the deviation ($\Delta\lambda_{edge}$) is limited to $\sim \pm 2$ nm. Nevertheless, we observe a monotonous variation of edge-slope, i.e. $S_{edge} = \frac{dP_T}{d\lambda}$ in the transmission characteristics as a function of ΔW (see inset of Fig.3.23). It is also observed that for $\Delta W > 170$ nm, slope of the edge increases very fast. Thus one can easily obtain a desired slope by suitable choice of a ΔW value.

3.3.3 Tunability of the REF Characteristics

The tunability of the REF characteristics is verified with DI water cladding. Fig. 3.24 compares the transmission characteristics of a REF device ($\Delta W = 200$ nm, $L_g = 500 \mu\text{m}$) for air and DI water claddings. The observed red-shift in λ_{edge} (λ_B^{00}) is 5.42 nm (4.44 nm), which is somewhat lower but consistent with theoretical results shown in Fig. 3.25(a) for a device with $L_g = 100 \mu\text{m}$. By inserting the experimentally observed red-shifts (due to DI water cladding) in Eq. 3.2 and 3.3, we estimate the change in effective refractive indices of $\Delta n_{eff}^0 = 0.76 \times 10^{-2}$ and $\Delta n_{eff}^1 = 1.11 \times 10^{-2}$; the results are consistent with theoretical predictions. In other words, we can infer that the fabricated devices exhibit 1-nm of tunability in λ_{edge} for an effective total change of $\Delta(n_{eff}^0 + n_{eff}^1) \approx 3.45 \times 10^{-3}$. This change in effective refractive index can be eas-

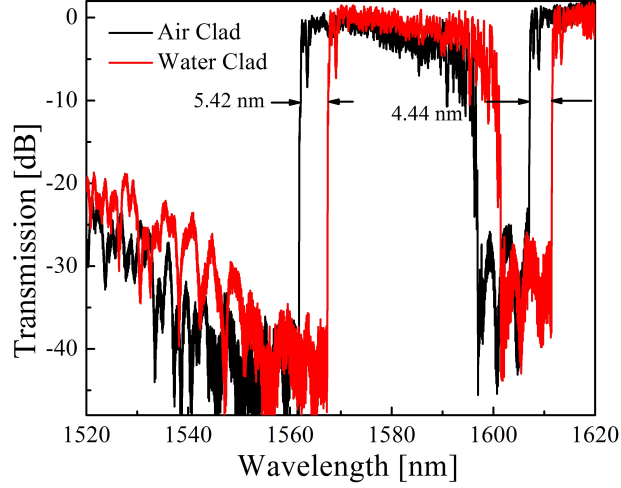


Figure 3.24: Normalized transmission characteristics of a 500- μm -long REF device (D5) with top cladding materials as air (black) and DI water (red).

ily obtained by integrating either a microheater (to avail excellent thermo-optic effect) [36, 103], or a p-i-n/p-n phase-shifter (to avail high-speed plasma dispersion effect) [104]. Besides the red-shift sensitivity of $S_\lambda \sim 18 \text{ nm/RIU}$, we also expect a change in slope of the edge due to the cladding refractive index change as it reduces the strength of grating modulation. This has been studied for two REF devices with $\Delta W = 200 \text{ nm}$ and 180 nm , respectively, and they are presented in Fig. 3.25. It is evident that the edge-slope S_{edge} estimated at a transmission of -20 dB , is reduced from 118 dB/nm (70 dB/nm) to 105 dB/nm (54 dB/nm) for $\Delta W = 200 \text{ nm}$ (180 nm), when air cladding is replaced by DI water cladding. Thus we infer that the proposed REF device can be used as a highly sensitive refractive index sensor by setting a laser wavelength fixed at $\lambda_L \sim \lambda_{edge}$. In this case, the transmitted power dependent refractive index sensitivity (S_p) can be evaluated as:

$$S_p = S_{edge} \cdot S_\lambda \quad (3.7)$$

By setting the laser wavelength λ_L at a transmission operating point of -20 dB near the filter edge, we have estimated the value of $S_p = 1890 \text{ dB/RIU}$ for a REF with $\Delta W = 200 \text{ nm}$ and at a cladding refractive index of $n_c = 1.318$ (DI Water). Therefore, the limit of detection (LOD) for a measurable differential power level of 1 dB is $\sim 5.3 \times 10^{-4} \text{ RIU}$. It must be noted that the red-shift in λ_{edge} is assumed to be linear with the cladding refractive index change (for $n_c > 1$) in the above estimations, which needs to be verified with further experimentation and/or with simulation results.

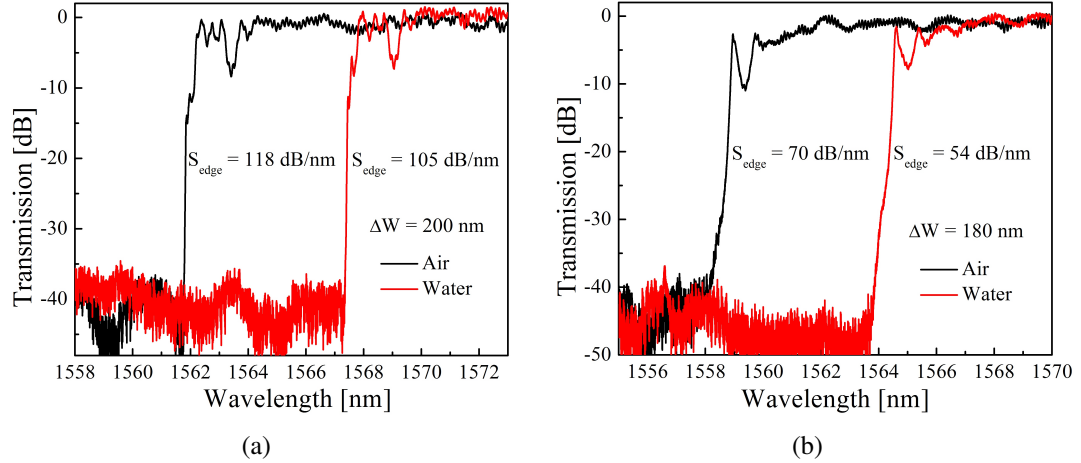


Figure 3.25: Sharp-edge filter characteristics of the devices for air cladding (in black) and DI water cladding (in red): (a) device with $\Delta W = 200$ nm (D5), and (b) device with $\Delta W = 180$ nm (D10).

3.4 Summary

A new integrated optical DBR grating device has been proposed and demonstrated in SOI substrate exhibiting a wavelength transfer function with a sharp-edge or rectangular-edge filter (REF) response in C-band ($1530\text{nm} \leq \lambda \leq 1565$ nm). The device working principle is described first with a semi-analytical model and then FDTD simulations results are presented to quantify various figure of merits. Analyzing the simulation results, the design parameters were finalized and subsequently REF devices were fabricated using standard process developed in our laboratory. The characterization results of fabricated REF devices are found to be consistent with theoretical predictions. A filter response with a sharp-step of > 40 dB is achieved at $\lambda_{edge} \sim 1561$ nm. The slope of the step S_{edge} is found to be 118 dB/nm and 105 dB/nm for air and DI water claddings, respectively. During the literature survey, we found the work of J.St-Yves et. al. (Fig. 1.5 (c) of the revised thesis) showing edge roll-off as high as ~ 50 dB/nm using contra-directional coupling in DBR integrated in directional coupler. In this thesis, we report ultra-sharp edge roll-off of 118 dB/nm which is the highest value to the best of our knowledge.

It has been also shown experimentally that the slope of the REF response can be controlled by varying the grating modulation. Moreover, the rectangular-edge step in the transmission characteristics of fabricated devices is usually followed by a broad

pass-band (~ 40 nm). Such a device can be useful as a long-pass wavelength filter in an on-chip optical WDM networking system. The device can also be used in Raman spectroscopy as it can selectively filter Raman shifted signals from the pump.

Besides device demonstration, a qualitative and quantitative discussions are presented in support of various active applications such as refractive index sensor, reconfigurable filter response by thermo-optic tuning, and high-speed intensity modulation by integrating p-n/p-i-n diode, etc.

CHAPTER 4

Photonic Passband Filter

In the previous Chapter, we experimentally demonstrated a rectangular edge filter device by integrating a DBR structure using asymmetric waveguide width modulation in SOI. A rectangular edge filter with very high slope and high extinction ratio were obtained. In this Chapter, we extend our work by cascading such two DBR of different grating periodicity in a multimode waveguide. The effect of cascading DBR is reflected in tailoring the passband characteristics of the device. Thus, the obtained delay-free passband can be narrowed down and the side stopbands can be widened in the transmission spectrum of the device. The cascading of two DBR is first described semi-analytically to predict the expected spectral result. The device is then fabricated and characterized to validate the theoretically expected results.

To implement an optical bandpass filter using grating one has to separate reflected band from input port via the design techniques based on wavelength splitting or contra-directional coupling into another waveguide or multimode interference. This is possible by keeping two ports at input side - one for input port to launch the light into the device and another for output port to separate reflected light. The schematic diagrams of grating assisted Y-junction, MMI and MZI are shown in Fig. 4.1. Each of these devices can separate out the reflected wave at drop port from the incident wave at input port. In these devices, a number of ports and design complexity obviously increases in order to route the reflected wave in drop ports. All of these techniques are based on the constructive interference of the reflected waves at the drop port. Since a phase shift of 2π or its integral multiple has to be maintained in constructive interference, any phase error introduced within the reflection path may reduce the intensity at "Drop port", also introducing fractional back reflected power at the "In Port" which are undesirable. Phase error becomes more critical in all these cases. Further, the reflected wave (particularly the phase matched wave) suffers a phase change of $\pi/2$ with respect to the incident transmitted waves (particularly out-of-phase waves) introducing a time delay in the signal which may be undesirable in some synchronous detection systems.

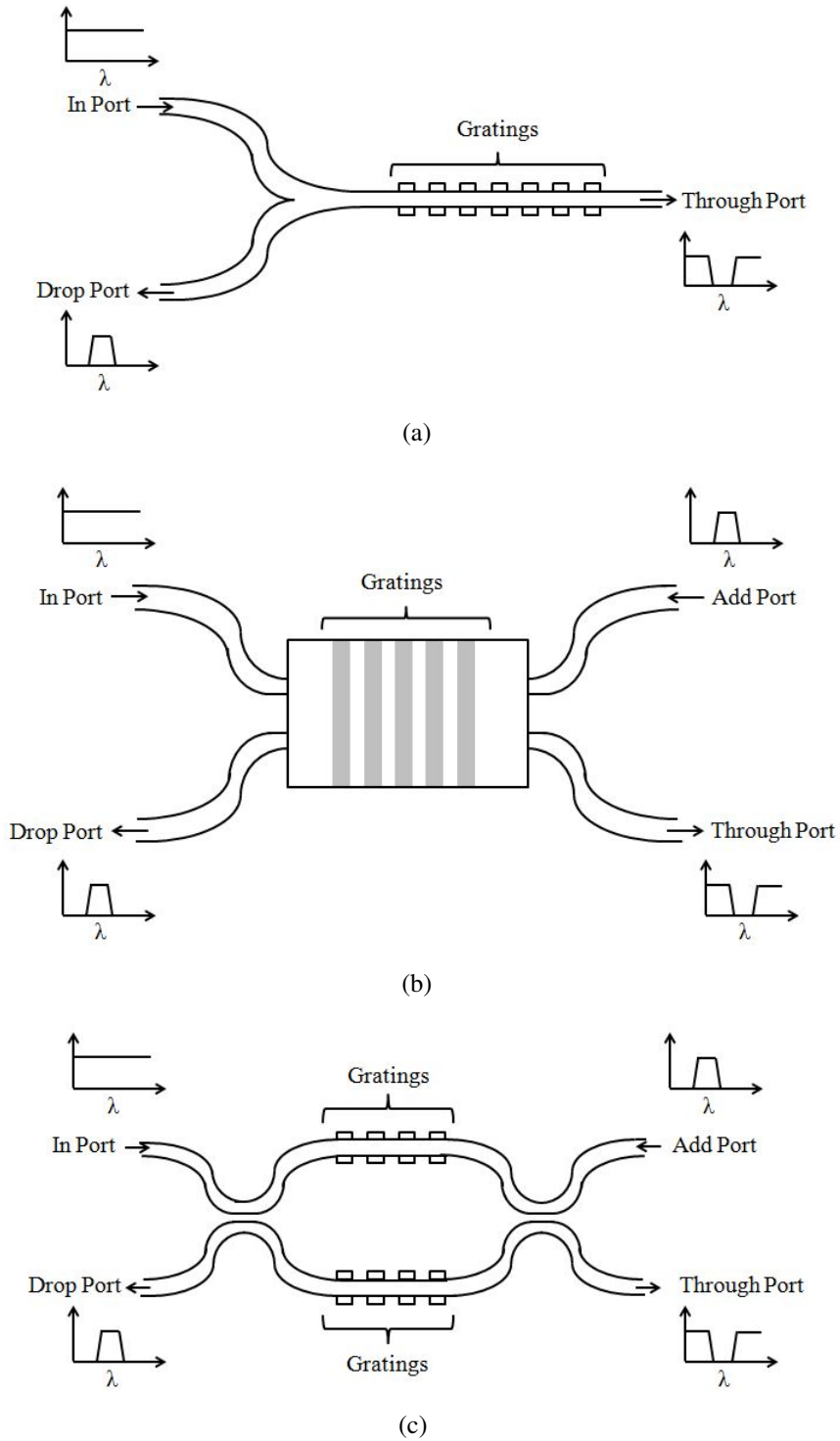


Figure 4.1: Schematic of grating assisted design (top view) of (a) Y-junction, (b) Multi-mode-interferometer and (c) Mach-Zehnder interferometer. The example of expected wavelength spectrum at each ports are also shown.

However, one can achieve the passband in transmission port itself by using proper design technique. Very recently we demonstrated rectangular-edge filter in transmission [98] using asymmetric side wall grating. One can also realize passband in trans-

mission between the two stopbands of a cascaded symmetric grating of a dissimilar period but it has the limitation on stopband control. To enhance spectral properties of the grating-based filters, the cascaded grating has been studied for various purposes, for instance, tunable optical delay line by cascading complementary apodized silicon grating [105], widely bandwidth tunability by grating assisted contra-directional couplers [78] and flat-top spectral response by cascading sub-wavelength resonant gratings vertically [106]. There is need to study the passband engineering in transmission port by cascading two gratings.

Thus, we define new wavelength characteristics of a cascaded DBR device as research work for some specific applications. The transmission characteristic of the cascaded DBR structure should have the following criteria:

1. narrower and phase-delay-free passband in transmission spectrum
2. wider stopbands at both side of the passband in transmission spectrum
3. high passband to stopband extinction ratio
4. the bandwidth of the passband can be engineered by controlling device parameter.

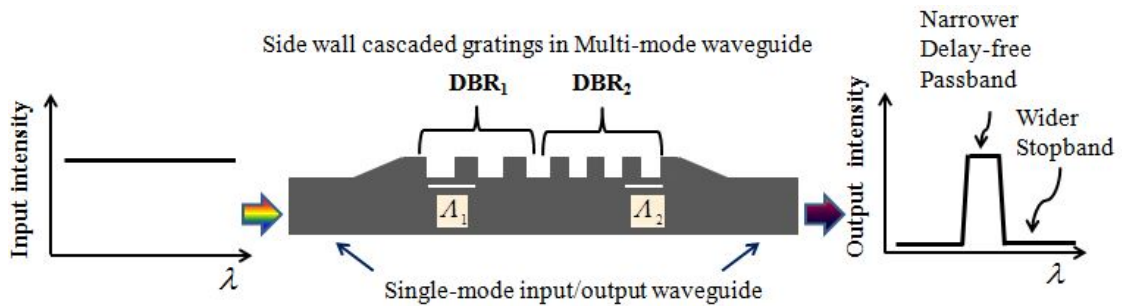


Figure 4.2: A cartoon to represent rectangular edge filter using integrated Bragg grating with the DBR device, input-output wavelength characteristics shown together.

A cartoon representing the wavelength characteristics of a cascaded DBR device in a multimode waveguide is shown in Fig. 4.2. A wide band of wavelength with flat-top intensity is being launched in the device. A relatively narrower delay-free passband is obtained at the output of the device as a result. One can achieve a delay-free passband in the transmission spectrum of the DBR device by using the single stage side wall grating in a multimode waveguide. But, in this way, the passband width cannot be narrowed down beyond a certain limit and at the same time side, stopbands also cannot be

widened up to some extent. Therefore passband control has been limited by device parameters in such a single stage device reported. We start with the qualitative discussion of limitations of single stage grating on passband width first, followed by presenting cascaded grating with semi-analytical theory, experimental result, and discussion.

4.1 Limitations of Single Stage DBR on Pass Bandwidth

In chapter 3, section 3.1.1 we have presented the iterative method for computing Bragg wavelengths λ_B^{00} and λ_B^{01} . We also plotted the graphs of converged Bragg wavelengths as a function of waveguide width ($W_2 = W_1 + \Delta W$) for a different grating period. As waveguide width increases, both λ_B^{00} and λ_B^{01} increase approximately linearly. But since we kept W_1 constant at 560 nm, increasing the value of W_2 actually increases the value of grating modulation ΔW . So the effect of ΔW on two stopbands (around these Bragg wavelengths) and the passband between the two stopbands have been studied here. The stopbands occurring at λ_B^{0m} can be given as [97]:

$$\Delta\lambda_{sb}^{0m} = \frac{2(\lambda_B^{0m})^2}{\pi[n_{eff}^{00}(\lambda_B^{0m}) + n_{eff}^{0m}(\lambda_B^{0m})]} |\kappa^{0m}| \quad (4.1)$$

for $m = 0, 1$. where λ_B^{0m} are given by Eq. 3.2 and 3.3, the coupling coefficient κ^{0m} is given by Eq. 3.6. Substituting $(n_{eff}^{00}(\lambda_B^{0m}) + n_{eff}^{0m}(\lambda_B^{0m}))$ with $\frac{\lambda_B^{0m}}{\Lambda}$ in Eq. 4.1 it can be simplified to be the function of Λ , κ^{0m} and λ_B^{0m} as given by the following equation:

$$\Delta\lambda_{sb}^{0m} = \frac{2}{\pi} \Lambda \lambda_B^{0m} |\kappa_{0m}| \quad (4.2)$$

Clearly from Eq. 4.1, $\Delta\lambda_{sb}^{0m}$ depends on κ^{0m} which in turn depends on modal overlap between forward and backward propagating modes. The overlap region is defined by etching depth of the grating and grating modulation width ΔW . Also, $\Delta\lambda_{sb}^{0m}$ depends on grating period Λ and Bragg wavelengths λ_B^{0m} which in turn depend on grating and waveguide parameters. Since the two Bragg wavelengths are discrete and are separated sufficiently (see Fig. 3.6), there exist the passband between these stopbands. The

passband width $\Delta\lambda_{pb}$ can be obtained by:

$$\Delta\lambda_{pb} = (\lambda_B^{00} - \lambda_B^{01}) - \frac{1}{2}(\Delta\lambda_{sb}^{00} + \Delta\lambda_{sb}^{01}) \quad (4.3)$$

Also its center wavelength λ_C can be given as:

$$\lambda_C = \frac{\lambda_B^{00} + \lambda_B^{01}}{2} + \frac{1}{4}(\Delta\lambda_{sb}^{01} - \Delta\lambda_{sb}^{00}) \quad (4.4)$$

One way of shifting λ_C in passive manner is to change the value of grating period as the Bragg wavelengths (λ_B^{0m}) shift with grating period as already shown in Fig. 3.6. The calculated value of $\frac{d\lambda_B^{0m}}{d\Lambda}$ are 4.4 nm and 4.1 nm for $m = 1$ and 2 respectively.

Substituting Eqs. 3.2, 3.3, 4.1 in Eq. 4.3, we can redefine passband width as:

$$\Delta\lambda_{pb} = (1 - \frac{\Lambda}{\pi}|\kappa^{00}|)\lambda_B^{00} - (1 + \frac{\Lambda}{\pi}|\kappa^{01}|)\lambda_B^{01} \quad (4.5)$$

Thus, Eq. 4.5 helps to estimate photonic passband width of side wall grating integrated in a multimode waveguide at one of the side walls. As the values of λ_B^{0m} depend on W_2 , Λ and n_{eff}^{0m} and the values of $|\kappa_{0m}|$ depend on grating modulation ΔW , the passband width can be engineered/controlled by suitable choice of a waveguide as well as grating parameters. Calculated passband width $\Delta\lambda_{pb}$, side stopbands widths $\Delta\lambda_{sb}^{00}$ and $\Delta\lambda_{sb}^{01}$ and passband center wavelength λ_C as a function of waveguide width W_2 (with $H = 250$ nm and $h = 150$ nm) are shown in Fig. 4.3 for three different grating periodicity ($\Lambda = 282$ nm, 286 nm, and 290 nm).

We can observed that the side stopband widths are increased with the waveguide width (since the values of κ_{0m} increases with $W_2 - W_1$) as we discussed earlier. But $\kappa_{01} > \kappa_{00}$ is due to higher value of overlap between the fundamental and first order modes as compared to that between fundamental to fundamental modes. This is obvious as the first order mode intensity is more towards the wall of the grating where modal overlap takes place in one sided side wall grating. It is also worth noticing that photonic passband width reduces as the waveguide width increases. It is intuitively explained as separation between effective indices $\Delta n_{eff} = n_{eff}^{00} - n_{eff}^{01}$ reduces at higher waveguide width since modes become more relaxed in multimode dimension. The direct effect of

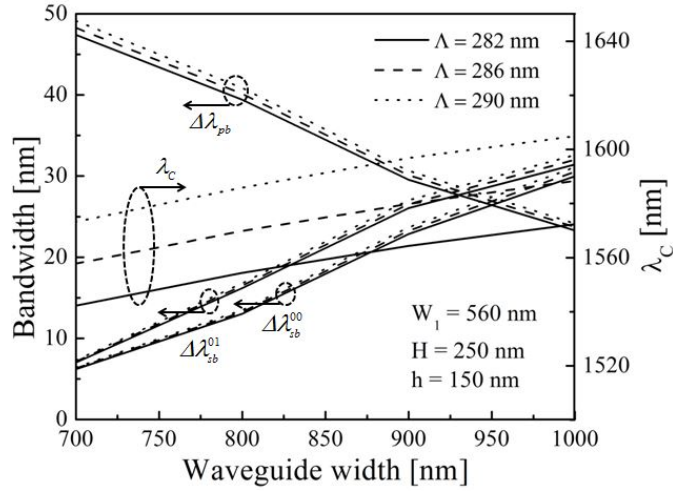


Figure 4.3: Calculated spectral widths of photonic passband ($\Delta\lambda_{pb}$) and its center wavelength (λ_C), and side stopbands ($\Delta\lambda_{sb}^{00}$ and $\Delta\lambda_{sb}^{01}$) as a function waveguide width W_2 supporting only two lower order modes in TE-polarization, for three different grating periods.

Δn_{eff} on passband width $\Delta\lambda_{pb}$ can be established by simply putting the values of λ_B^{0m} in Eq. 4.3 as:

$$\Delta\lambda_{pb} = \Lambda(n_{eff}^{00} - n_{eff}^{01}) - \frac{\Lambda^2}{2\pi}[2n_{eff}^{00}k^{00} + (n_{eff}^{00} + n_{eff}^{01})k^{01}] \quad (4.6)$$

Again the center wavelength (λ_C) of the passband varies significantly as a function of grating period Λ as well as with the waveguide width W_2 . Since the waveguide width cannot be increased beyond $1.25 \mu\text{m}$ to avoid further higher order guided modes (see Fig. 3.7) and to keep $\lambda_C \sim 1550 \text{ nm}$, the pass bandwidth cannot be decreased below $\sim 25 \text{ nm}$ and side stopband widths cannot be increased above $\sim 30 \text{ nm}$. Therefore, to achieve a narrower photonic passband and wider side stopbands, it is preferable to go for cascaded DBR gratings. Thus for a given device parameters, the width of passband can be predicted theoretically. For instance, We calculated BW_{pb} as 38 nm for $W_1 = 560 \text{ nm}$, $W_2 = 760 \text{ nm}$, $H = 250 \text{ nm}$, $h = 150 \text{ nm}$, $\Lambda = 290 \text{ nm}$. This value of passband width matches to the experimentally observed passband width for same device parameters as we studied in Chapter 3, Section 3.3, Fig. 3.21.

4.2 Device Description and Design

The proposed device 3D schematic is shown in Fig. 4.4 where DBR₁ with period Λ_1 and DBR₂ with period Λ_2 are being cascaded and integrated with multimode rib waveguide at one of the side walls of the waveguide. The rib waveguide of width W_1 in the input/output waveguide supports fundamental transverse electric (TE) mode only and the rib waveguide of width W_2 in the grating region supports fundamental and first order TE modes. The input/output waveguides are adiabatically coupled to the multimode grating section.

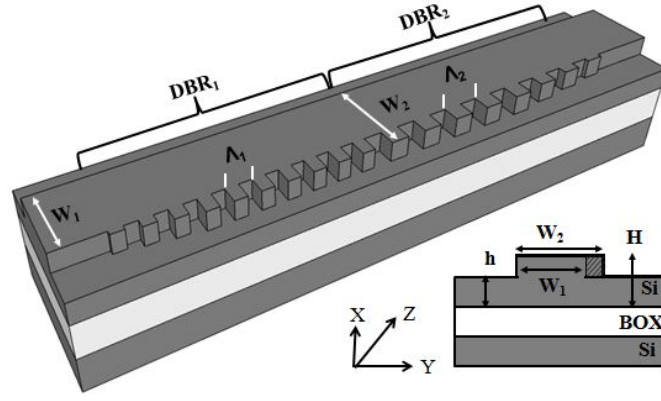


Figure 4.4: Schematic of 3D integrated cascaded grating devices with grating period Λ_1 and Λ_2 ; the cross section of the device with the device parameters: W_1 , W_2 - waveguide widths, H , h - core height and slab height is shown at bottom right corner.

The cross-section of the device with coupling regions (dashed lines) is shown in Fig. 4.4 (right bottom corner), where W_1 is the waveguide width in input/output access waveguides and W_2 is the waveguide width in a grating assisted waveguide; H and h are waveguide's core height and slab height respectively. The device parameters were selected such as the passband filter characteristic of the device is within the wavelength range: ($1500 \text{ nm} \leq \lambda \leq 1650 \text{ nm}$) and supporting two lower order modes.

In the device with only DBR₁ or DBR₂, fundamental mode expands adiabatically through the taper section and enters into the grating section. In a grating section, fundamental and first-order modes get reflected back due to periodic perturbations at two different phase-matched wavelengths as they couple to the forward propagating fundamental mode. The reason for two modes excitation in the backward direction is the multimode nature of waveguide in grating section. The resulting phase-matched wave-

lengths are defined by Bragg equation [97, 98] (see Eq. 3.2 and 3.3 in Chapter 3). The filtering characteristics of the proposed devices are qualitatively described in Fig. 4.5. The first DBR grating (DBR_1) with period Λ_1 matches the phase of the forward

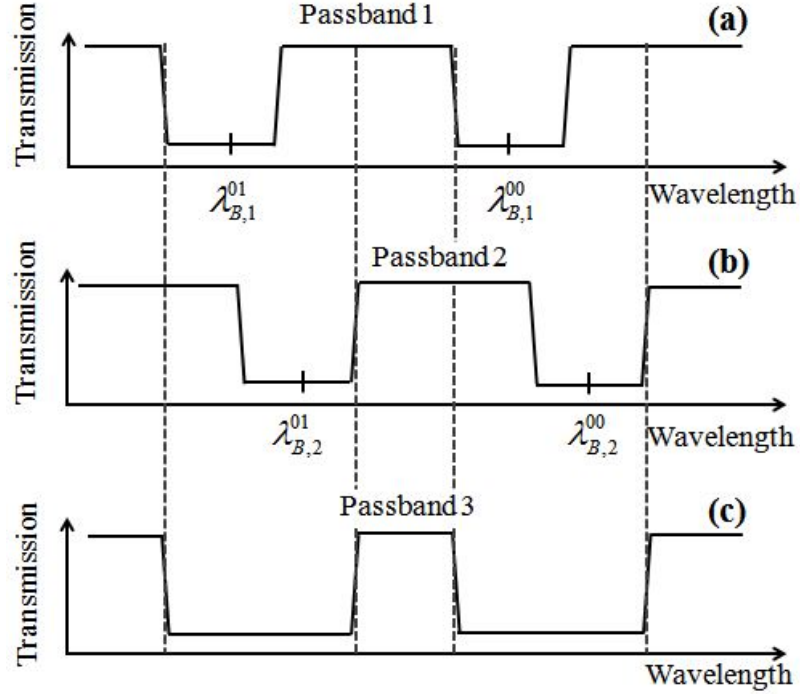


Figure 4.5: Schematic representation of the transmission spectra of the proposed photonic bandpass filter devices: (a) DBR_1 with period Λ_1 ; (b) DBR_2 with period Λ_2 ; and (c) cascaded DBR_1 and DBR_2 as represented in Fig. 4.4.

propagating fundamental mode with backward propagating fundamental mode and first order mode at two different wavelengths ($\lambda_{B,1}^{00}$) and ($\lambda_{B,1}^{01}$), respectively. This results into stopbands at around ($\lambda_{B,1}^{00}$) and ($\lambda_{B,1}^{01}$) with bandwidths $\Delta\lambda_{sb}^{00}$ and $\Delta\lambda_{sb}^{01}$ respectively. Similarly, for DBR grating (DBR_2) with period Λ_2 , two phase matched Bragg wavelengths are $\lambda_{B,2}^{00}$) and ($\lambda_{B,2}^{01}$). As we have explained in the previous section that the bandwidths of these stopbands are limited by the acceptable value of $\Delta W = W_2 - W_1$ or the strength of grating modulation. A well-defined passband between $\lambda_{B,1}^{00}$ and $\lambda_{B,1}^{01}$ is represented as "Passband1" and between $\lambda_{B,2}^{00}$ and $\lambda_{B,2}^{01}$ is represented as "Passband2" for the devices DBR_1 and DBR_2 as shown in Fig. 4.5 (a), (b) respectively. The "Passband2" is red shifted with respect to "passband1" as the grating period $\Lambda_2 > \Lambda_1$. It was shown earlier that such a passband is sufficiently broad and escorted by relatively narrower stop-bands.

Since the transfer function of individual DBR grating gets multiplied when they are cas-

caded, the resultant transmission characteristic of the cascaded DBR grating system can be defined as the overlap of the two individual transmission characteristics as shown in Fig. 4.5 (c). The resultant pass bandwidth (represented by Passband3) is significantly reduced and the side stopbands are effectively widened.

For two cascaded DBR gratings with slightly varying periods Λ_1 and Λ_2 ($\Lambda_1 < \Lambda_2$) and identical κ^{00} and κ^{01} (assuming grating modulation width ΔW same for both DBR gratings), the resultant photonic passband ($\Delta\lambda_{pb}^{casc}$) and its center wavelength (λ_C^{casc}) are given by:

$$\Delta\lambda_{pb}^{casc} = \left(1 - \frac{\Lambda_1}{\pi} |\kappa^{00}| \right) \lambda_{B,1}^{00} - \left(1 + \frac{\Lambda_2}{\pi} |\kappa^{01}| \right) \lambda_{B,2}^{01} \quad (4.7)$$

$$\lambda_C^{casc} = \frac{\lambda_{B,1}^{00} + \lambda_{B,2}^{01}}{2} + \frac{1}{4} (\Delta\lambda_{sb,2}^{01} - \Delta\lambda_{sb,1}^{00}) \quad (4.8)$$

Here (1) and (2) in the subscript of λ_B^{0m} representation correspond to DBR₁ and DBR₂ of cascaded DBR structures respectively. Thus, by a suitable choice of Λ_1 and Λ_2 , one can achieve photonic passband $\Delta\lambda_{pb}^{casc} \ll \Delta\lambda_{pb}$.

Delay-free passband can be defined by analyzing reflectivity and delay characteristics of a DBR grating. Fig. 4.6 shows the reflectivity (R) and normalized effective group delay (τ/τ_0) as a function of wavelength for $\kappa L_g = 3$, where τ_0 is the path delay without DBR of waveguide length of L_g . The filter addressed in this chapter is the

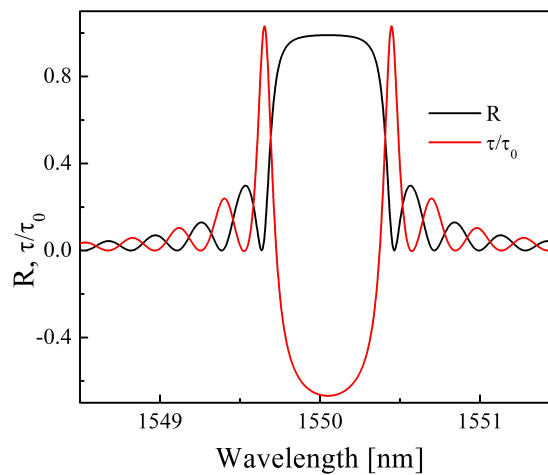


Figure 4.6: Normalized effective group delay τ/τ_0 and reflectance R of a DBR as function of wavelength.

bandpass filter occurring in between the two Bragg wavelengths that is λ_B^{00} and λ_B^{01} .

This region of the wavelength characteristic is completely outside the resonance. Only at the edges of the passband is slightly affected by delay, otherwise it stands delay-free in whole middle region (see Fig. 4.6).

4.3 Experimental Results and Discussions

To validate the theoretical passband and stopband widths for individual DBR gratings and cascaded DBR gratings, devices were fabricated with the optimized device parameters in Silicon. Here we will discuss the effect of grating period and modulation width on photonic passband and stopband characteristics. The spectral characteristics of the cascaded grating system are shown to have better control over photonic passband and stopband characteristics. Finally, fabrication tolerance has been studied in context to justify the experimentally observed trend in pass bandwidth and center wavelengths.

4.3.1 Device Fabrication

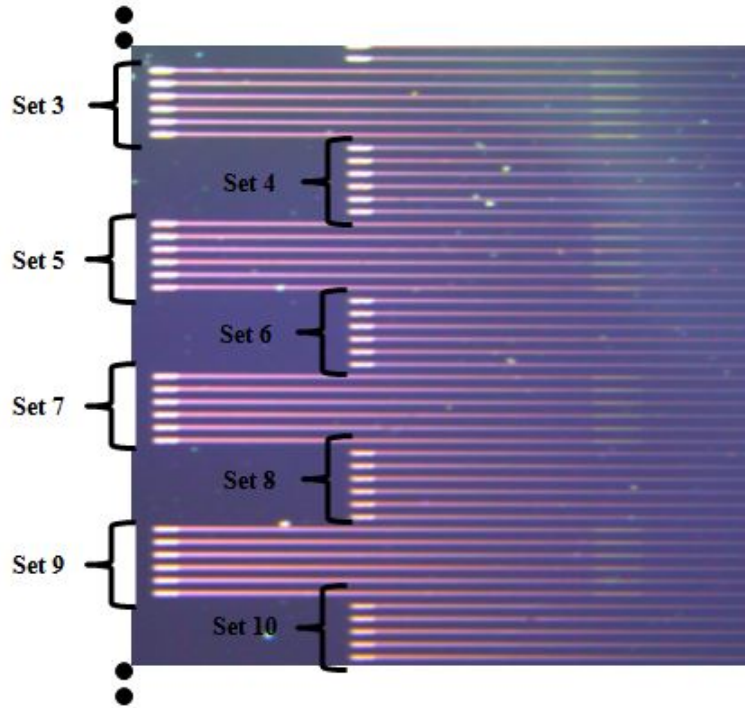
The optical grade SOI substrate with a device layer thickness of 250 nm, buried oxide layer thickness of 3 μm , and handle wafer thickness of 500 μm was chosen for fabrication of the waveguide, grating coupler, DBR grating and cascaded DBR grating devices. Devices were fabricated using single step e-beam lithography followed by dry etching procedure. We adopted the similar optimized fabrication process parameters as given in Chapter 2, Section 2.3. Thirteen sets of devices were fabricated on 2 cm \times 2 cm SOI sample, their optical photograph is shown in Fig. 4.7(a). Detail of each set is tabulated in Table 4.1. There are sets of a straight waveguide (waveguide written as wg), DBR grating of different periods and cascade DBR gratings of different period combinations. Straight waveguides were fabricated along with DBR grating devices in order to normalize the grating characteristics for calculating the loss of grating devices. Individual DBR gratings with different periods were fabricated to study the effect of grating period on center wavelength and passband of the devices as we have theoretically studied these effects in Section 4.1 using Fig. 4.3. Cascaded gratings with the combination of different periods have been fabricated to analyze the passband and

stopband engineering.

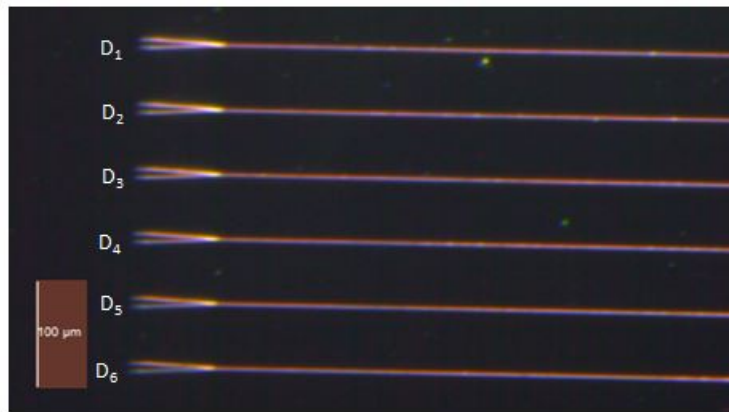
Table 4.1: Device specifications for the fabricated devices as shown in Fig. 4.7(a).

Set No.	Device type	Device No.	Device parameters		
			Λ_1	Λ_2	L_g
1	Straight wg	$D_1 - D_6$			
2	DBR	$D_7 - D_{12}$	290 nm		500 μm
3	DBR	$D_{13} - D_{18}$	290 nm		250 μm
4	DBR	$D_{19} - D_{24}$	282 nm		250 μm
5	cascade DBR	$D_{25} - D_{30}$	290 nm	290 nm	500 μm
6	DBR	$D_{31} - D_{36}$	284 nm		250 μm
7	cascade DBR	$D_{37} - D_{42}$	290 nm	284 nm	500 μm
8	DBR	$D_{43} - D_{48}$	286 nm		250 μm
9	cascade DBR	$D_{49} - D_{54}$	290 nm	286 nm	500 μm
10	DBR	$D_{55} - D_{60}$	288 nm		250 μm
11	cascade DBR	$D_{61} - D_{66}$	290 nm	288 nm	500 μm
12	DBR	$D_{67} - D_{72}$	282 nm		250 μm
13	cascade DBR	$D_{73} - D_{78}$	290 nm	292 nm	500 μm

Each set of devices consists of six waveguides. The individual waveguides are named as D_i , $i = 1, 2, \dots, 78$. Each of the devices is terminated with input and output grating couplers for characterization purpose using optical fiber and laser setups. Fig. 4.7(b) shows the optical photograph of six devices (set number 1, straight waveguides: D_1 to D_6) with the input grating coupler visible at left side of the devices. Gratings of periods varying from 282 nm to 292 nm in the step of 2 nm and their cascade with grating period 290 nm were fabricated in SOI with device parameters W_1 , W_2 , H and h as 560 nm, 910 nm, 250 nm and 150 nm respectively in the devices with set number 2 to 13 device number D_7 to D_{78} . 2 nm detuning in the grating period were characterized to provide better bandwidth narrowing down as analyzed in theoretical analysis (see Fig. 4.5). There is no inaccuracy in relative width patterning using e-beam. However, it can give unexpected dc shifts in patterning widths, but keeping relative width approximately constant. Thus, 2 nm difference in the grating pitch is quite reproducible. Optical lithography as for e.g. dip UV can better control the dc shift in the device width, without disturbing the relative device widths. To reduce the ripples at the transition width $W_1 \rightarrow W_2$, in DBR grating devices, ΔW is increased in the step of 20 nm with taper



(a)

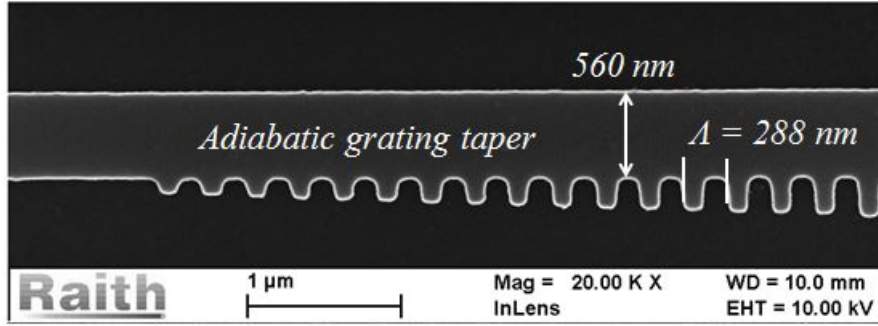


(b)

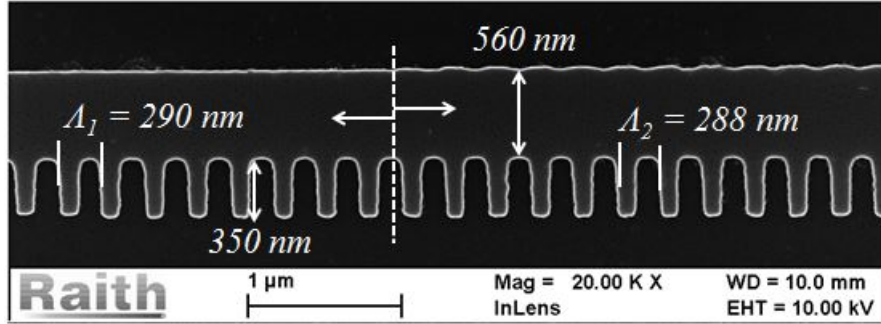
Figure 4.7: Optical photographs of fabricated (a) whole sample with all the sets of devices and (b) one set of devices.

length of $\sim 5 \mu\text{m}$ at both interfaces of grating. The SEM image of tapered grating modulation width is shown in Fig. 4.8(a). This adiabatic taper also helps in expanding fundamental mode while propagating from input waveguide (width W_1) to grating waveguide (width W_2). Fig. 4.8(b) shows the SEM image of one of the cascaded gratings devices with periodicities $\Lambda_1 = 288 \text{ nm}$ and $\Lambda_2 = 290 \text{ nm}$.

As the devices were defined directly by e-beam lithography (relatively slow process), we could not avoid small drift in the grating region for period of 288 nm. However, we



(a)



(b)

Figure 4.8: SEM images of fabricated devices: (a) adiabatically tapered grating of periodicity 288 nm; and (b) transition region of two cascaded DBR gratings of $\Lambda_1 = 290$ nm and $\Lambda_2 = 288$ nm.

have not observed any significant degradation in device characteristics for these small periodic ripples in grating structure (see Fig. 4.8).

Fig. 4.9 shows the transmission characteristics of three multimode waveguide devices each integrated with a 250- μm -long DBR grating period $\Lambda = 282$ nm. Their average transmission characteristics (red color) and the transmission characteristics of a reference waveguide are also shown. All the devices exhibit a passband centering around $\lambda_C \sim 1563$ nm and side stopbands at $\lambda_B^{01} \sim 1543$ nm and $\lambda_B^{00} \sim 1583$ nm, respectively. There is a relatively narrower passband observed below lower-side stopband (at $\lambda \sim 1535$ nm). The low transmission band below $\lambda \sim 1530$ is attributed to the coupling to leaky substrate modes. Average insertion loss for the entire passband at $\lambda_C \sim 1563$ nm is estimated to be ~ 3.5 -dB.

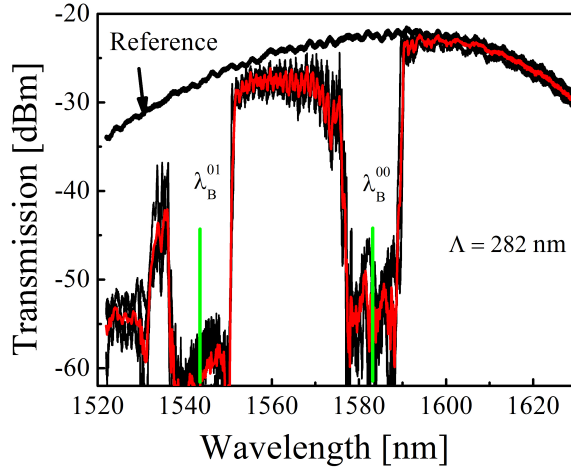


Figure 4.9: Transmission spectra of three multimode waveguides each integrated with 250- μm -long DBR grating ($\Lambda = 282$ nm, $\Delta W = 350$ nm) in one of the side-walls of a multimode waveguide with W , H , h as 560nm, 250 nm and 150 nm, respectively. Their average transmission spectrum (red color) and the transmission spectrum corresponding to a reference waveguide (black color) are also shown.

4.3.2 Photonic Passband Filter: Single-Stage DBR

The normalized transmission characteristics of gratings with period 282 nm, 284 nm, 286 nm, 288 nm, 290 nm and 292 nm are shown in Fig. 4.10. These characteristics were obtained by subtracting wavelength dependent transmission of a reference waveguide in dB scale. Each plot contains five or six similar device characteristics. The average transmission characteristics of the devices are shown in red colour.

The central wavelength (λ_C lying in the center of the passband as defined in Eq. 4.8) is shifting almost linearly towards higher wavelength region as grating period increases. The rate of increment of central wavelength with respect to the grating periods measured from Fig. as $\frac{d\lambda_C}{d\Lambda} = 4.3$.

Various parameters can be extracted from these experimental results which fully characterize the spectrum. For example, effective indices at corresponding Bragg wavelengths, their dispersion, center wavelength, stop bandwidth, pass bandwidth and coupling constants for two device sets with grating period $\Lambda = 284$ nm and $\Lambda = 286$ nm are shown in Table 4.2. The value of $\Delta\lambda_{pb}$ for the device with $\Lambda = 284$ nm is slightly higher than that of the device with $\Lambda = 286$ nm (contradicting theoretical prediction), which may be attributed to variations in device parameters (e.g. waveguide width, grat-

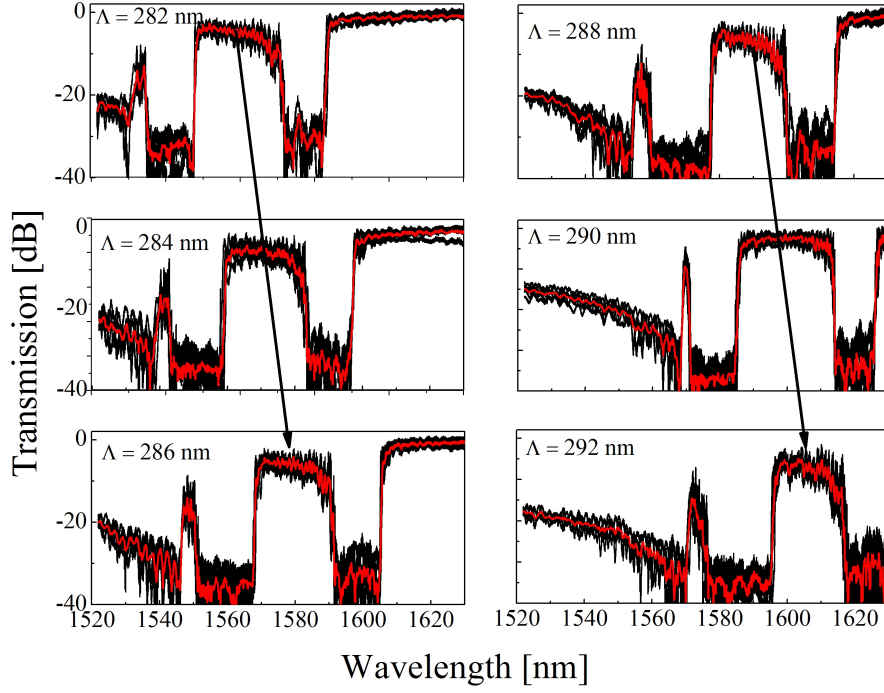


Figure 4.10: Transmission characteristics of DBR devices with grating period $\Lambda = 282$ nm - 292 nm, in step of 2 nm with $L_g = 250 \mu\text{m}$ grating ($\Lambda = 282$ nm, $\Delta W = 350$ nm) in one of the side-walls of a multimode waveguide with W , H , h as 560nm, 250 nm and 150 nm

Table 4.2: Device parameters extracted from the experimental results shown in Fig. 4.10.

Parameters	$\Lambda = 284$ nm	$\Lambda = 286$ nm
$n_{eff}^{00}(\lambda_B^{00})$	2.7993	2.7945
$n_{eff}^{00}(\lambda_B^{01})$	2.8265	2.8209
$n_{eff}^{01}(\lambda_B^{01})$	2.6347	2.6301
$\frac{dn_{eff}^{00}}{d\lambda}(\text{nm}^{-1})$	6.988×10^{-4}	6.988×10^{-4}
$\frac{dn_{eff}^{01}}{d\lambda}(\text{nm}^{-1})$	5.813×10^{-4}	5.813×10^{-4}
λ_C (nm)	1571	1579
$\Delta\lambda_{pb}$ (nm)	~ 24	~ 23
$\Delta\lambda_{sb}^{00}$ (nm)	~ 14	~ 14
$\Delta\lambda_{sb}^{01}$ (nm)	~ 16.4	~ 17.8
$\kappa^{00}(\mu\text{m}^{-1})$	0.0487	0.0481
$\kappa^{01}(\mu\text{m}^{-1})$	0.0571	0.0634

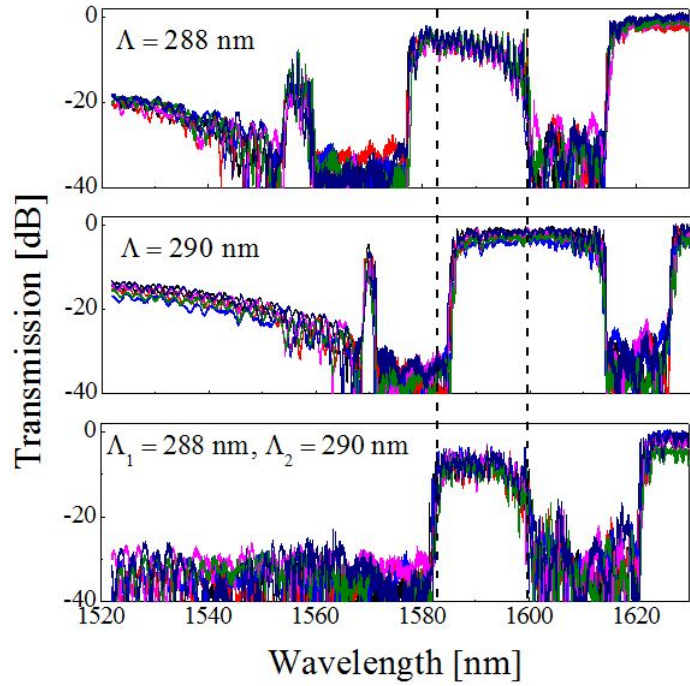
ing duty cycle etc.) after fabrication. The fabrication tolerance in device width using e-beam lithography may be within \pm nm. However, the spectral bandwidths of the side stopbands are found to be relatively narrower than that of photonic passbands, as

expected from theoretical simulation results discussed earlier.

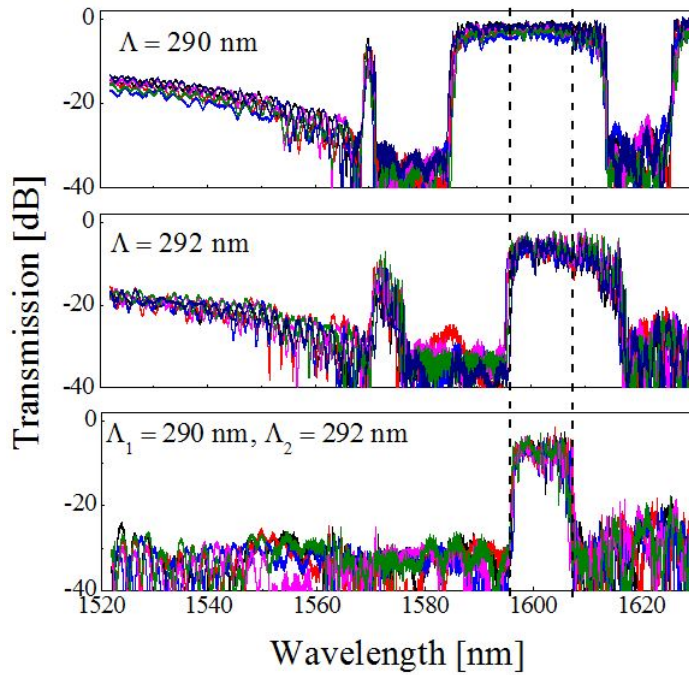
4.3.3 Photonic Passband Engineering: Cascaded DBR

Fig. 4.11(a) shows normalized transmission characteristics of the DBR devices with individual grating periods of 288 nm (at the top) and 290 nm (at middle); and their cascade (at the bottom). The passband in transmission characteristic of the cascaded DBR should be the overlap of the two individual passbands. However, the left edge of the passband in cascaded response is not perfectly matching to the left edge of the passband at the middle. This is caused due to fact that the grating modulation widths in the individual DBR are not the same as in the cascaded DBR. This happened because the three devices are fabricated on the same chip but in a different set of position-list in patterning scheme. It was observed that there is ΔW variation between the DBR devices of two different sets. But the ΔW variation in DBR devices of the same set are found to be negligible. The measured values of the ΔW in single stage grating of period 290 nm are ~ 360 nm, while the that for the DBR device with single stage grating of period 288 nm and that of cascaded DBR is 350 nm. The fabrication issues can be eliminated by continuous optimization of shifts in dose, beam current, aperture alignment, astigmatism corrections and many more patterning parameters. We measured the spectral width of the photonic passband of the cascaded device to be $\Delta\lambda_{pb}^{casc} \sim 17$ nm which is reduced significantly in comparison to the devices with single-stage DBR ($\Delta\lambda_{pb}^{casc} > 24$ nm) using Fig. 4.11(a). Using extracted parameters given in Table 4.2 and slopes $\frac{d\lambda_B^{00}}{d\Lambda} = \frac{d\lambda_B^{00}}{d\Lambda} = 4$ (also extracted from Fig. 4.10) along with Eqs. 3.2, 3.3 and 4.7; we computed the corresponding widths of photonic passband as 15 nm, which is fairly in good agreement with the above experimental results.

Similarly, Fig. 4.11(b) shows normalized transmission characteristics of the DBR devices with individual grating periods of 290 nm (at the top) and 292 nm (at middle); and their cascade (at the bottom). Here, the right edge of the passband in cascaded response is not perfectly matching to the right edge of the passband at the top. This is also caused due to the same region as we addressed earlier. Since ΔW of the single-stage DBR with period 292 nm has deviated 10 nm from that of the cascaded BDBR,



(a)



(b)

Figure 4.11: Transmission spectra of two single stage DBR (with different periodicity) and one cascaded DBR (with periodicity Λ_1 and Λ_2) (a) for DBR of period 288 nm, 290 nm, and their cascade, and (b) for DBR of period 290 nm, 292 nm, and their cascade. The DBR with $L_g = 250 \mu\text{m}$ grating, $\Lambda = 282$ nm, $\Delta W = 350$ nm was integrated in a multimode waveguide with W , H , h as 560nm, 250 nm and 150 nm, respectively.

no perfect overlap was achieved between the two individual DBR. Also, we measured the spectral width of the photonic passband of the cascaded device to be $\Delta\lambda_{pb}^{casc} \sim 10.6$ nm which is reduced significantly in comparison to the devices with single-stage DBR ($\Delta\lambda_{pb}^{casc} > 24$ nm) using Fig. 4.11(b). Using extracted parameters given in Table 4.2 and slopes $\frac{d\lambda_B^{00}}{d\Lambda} = \frac{d\lambda_B^{01}}{d\Lambda} = 4$ along with Eqs. 3.2, 3.3 and 4.7; we computed the corresponding widths of photonic passband as 10.8 nm, which is fairly in good agreement with the above experimental results. The side stopbands are also widened for these devices following theoretical prediction. The extinction of side stopbands in each of the cascaded devices is estimated to be ~ 30 -dB with respect to the maximum transmission of the photonic passbands. The passband width of the cascaded DBR can be further reduced by increasing the difference between the two periods of the cascaded DBR. The sharp roll-off at the wavelength 1605 nm in Fig. 4.11 is due to larger grating modulation width (~ 350 nm). However the edge roll-off near to the resonance wavelength $\lambda_B^{01} \sim 1590$ nm is more than that at resonance wavelength $\lambda_B^{00} \sim 16010$ nm. In this chapter, we are interested in the bandwidth narrowing property of the cascaded DBR structures with slightly detuned grating periods.

4.4 Fabrication Tolerance

A small change in device width (W) or slab height (h) during device fabrication can shift the transmission plots in wavelength. Waveguide lateral dimensions like width, a duty ratio of gratings, grating modulation etc can vary between the fabricated and geometrical mask of devices depending on e-beam lithography machine tolerance, a reliability of the e-beam resist, development time, pre-/post- bake time etc. The vertical dimensions of the waveguide, like slab height h ($h =$ device layer thickness H - etch depth) mainly depends on the physical and chemical environment of the dry etch processes, such as: temperature, pressure, chemicals(gases for reactive ion etching), etch time etc. Device slab height can also vary by warp and bow present in the sample itself which is controlled by the foundry. The rate of change of effective indices with respect to W and h are extracted from Fig. 3.7 and tabulated in Table 2.4 as included in Chapter 2. Since device output parameters as Bragg wavelengths (λ_B^{0m}) stop bandwidth ($\Delta\lambda_{sb}$),

pass bandwidth ($\Delta\lambda_{pb}$) and center wavelength (λ_C) all of these depend on effective indices and wavelength, the variation of effective index with respect to device parameters (W, h) gets reflected on all these parameters. For example, we can predict the effect of W and h on the central wavelength (λ_c) defined approximately as:

$$\lambda_C \sim \frac{\lambda_B^{00} + \lambda_B^{01}}{2} = \Lambda[3n_{eff}^{00} + n_{eff}^{01}] \quad (4.9)$$

The change in the central wavelength with respect to $\Delta\lambda_C(W, h)$ can be defined as total derivative:

$$\Delta\lambda_C \sim \frac{d\lambda_C}{dW}\Delta W + \frac{d\lambda_C}{dh}\Delta h \quad (4.10)$$

Using Equations 3.2, 3.3, 4.9 and 4.10 we can represent the change in the central wavelength again as:

$$\Delta\lambda_C \sim \Lambda \left[3 \frac{dn_{eff}^{00}}{dW} + \frac{dn_{eff}^{01}}{dW} \right] \Delta W + \Lambda \left[3 \frac{dn_{eff}^{00}}{dh} + \frac{dn_{eff}^{01}}{dh} \right] \Delta h \quad (4.11)$$

From Eq. 4.11 and Table 2.4, $\Delta\lambda_C$ can be found ~ 2 nm for $\Delta W = \Delta h = 1$ nm, $\Lambda = 290$ nm. Similar effect can also be predicted theoretically for filter edges.

The variation of filter edges in wavelength characteristics of the six different devices fabricated with same device parameters (see Fig. 4.10) can be attributed to the variation in waveguide width and slab height (W, h) due to fabrication and foundry limitations on planar surface. We have theoretically shown that the variations in W and h of ~ 1 nm can bring about change in center wavelength by ~ 1 nm. All follow the same pattern except a small shift of ~ 2 nm. This has been predicted theoretically that 1 nm variation in slab height can shift grating response.

4.5 Summary

In summary, we have demonstrated an integrated silicon photonics device which exhibits a delay-free (or resonance-free) photonic passband with highly extinguished side stopbands. The passband width was controlled by cascading the DBR of detuned peri-

odicity. The photonic passband filter device is designed with a multi-mode waveguide with side wall grating, which is adiabatically interfaced with input/output single-mode waveguides. The optical passband filter in transmission port of waveguide was demonstrated first time to the best of our knowledge. The pass-bands are bounded by two highly extinguished stop-bands (with an extinction of > 35 dB with edge roll-off of > 70 dB/nm) of $\Delta\lambda_{sb} > 15$ nm. The existence of two stopbands is due to two Bragg phase-matching conditions. The filter response is in the transmission, flat-top is naturally achieved however passband ripple were further minimized within ~ 1 dB by providing an adiabatic taper at input and output interfaces of DBR grating. The bandwidth is further narrowed down by cascading two gratings with detuned parameters. A semi-analytical model is used to analyze the filter characteristics ($1500 \text{ nm} \leq \lambda \leq 1650 \text{ nm}$). The pass bandwidth of waveguide devices integrated with single-stage gratings is measured to be ~ 24 nm, whereas for the device with two cascaded gratings with slightly detuned periods ($\Delta\Lambda = 2$ nm) exhibit pass bandwidth down to ~ 10 nm. Insertion loss and ripples in the passband can be reduced by improving side-wall roughness and by increasing taper lengths. It has been shown that the spectral widths of the photonic passband (and side stopbands) can be engineered depending on various applications.

CHAPTER 5

Conclusion

This thesis contributes in the area of silicon photonics - widely accepted as an enabling technology for the growth of semiconductor industries. It has been accomplished through a state-of-the-art literature survey followed by a series of failures and learning steps. Initially, the research work started with the theoretical understanding and demonstration of integrated optical DBR and DBR cavity in single-mode SOI waveguides. The major research outcome of this thesis work is a novel design and demonstration of rectangular edge filter and passband engineering by cascaded DBR structures in multimode SOI waveguides. Although there were no novelty in demonstrating the DBR and DBR cavity as they were already demonstrated earlier by many researchers, we understood the design criteria, minute details of the fabrication process steps, developing sophisticated characterization setup and analyzing measured results. In following two sub-sections, we present the thesis summary and the further scopes of research, respectively.

5.1 Thesis Summary

In the introduction chapter, first we reviewed the up-to-date progress of silicon photonics starting from optical interconnect solutions to futuristic silicon photonics quantum signal processing applications. Thereafter, we discussed how the concept of fiber Bragg grating has been translated into integrated silicon photonics for the demonstration of optical modulator, add-drop multiplexer, and sensing applications. Finally, with the view of international research scenario and the state-of-the-art research activities at IIT Madras, a feasible research objective was defined.

In Chapter 2, sub-micron dimension waveguide in SOI were presented in the light of effective indices of the guided mode in order to study the effect of waveguide parameters on guided mode(s). Shallow etched waveguide (of device layer thickness $H =$

220 nm - 250 nm, $h > 120$ nm) were found as exciting only TE guided mode(s) while the deeply etched ($h < 120$ nm) waveguide were found to excite both TE as well as TM mode(s). The waveguide become multimode for the larger values of the waveguide width. The waveguide dispersion were studied mainly because of the DBR device are highly dispersive around the phase matched wavelength. Phase matching condition for grating coupler as well as DBR were discussed with the help of wavevector diagram. Coupling coefficient were computed for TE mode for a single mode waveguide to analyze the DBR and phase shifted DBR characteristics using transfer matrix method. The DBR devices were fabricated using standard process developed in our laboratory. During fabrication, using e-beam lithography system, we found stitching error for longer grating length which was mitigated using longer write field. It was observed that there is trade-off between write field and quality of fabricated grating teeth i.e. smaller the write field better will be the quality of fabricated grating teeth. But, the smaller write field would not allow to pattern longer grating with stitching-error free DBR. Proximity error was another problem in patterning mixture of FBMS path and conventional geometry as they require different dose of charge per unit square. This was removed by proper design and dose selection.

Generally the device fabricated at the foundry are repeatable and takes lesser time. However, we at institute research level research, found the fabrication was the most challenging to produce a repeatable result using our institute resource. Nevertheless, this helped us to gain the skills of hands-on-practice for device fabrications. Integrated DBR and DBR cavity devices were demonstrated in a single mode SOI waveguide of 250 nm device layer thickness. Input-output grating couplers were integrated at both the ends of the waveguide in a single-step of e-beam patterning. The 3dB bandwidth of the grating coupler was found to be ~ 68 nm. The reflectivity of the DBR filter device was measured to be ~ 38 nm. The credit of getting high DBR reflectivity goes to longer grating length. A quarter-wave phase-shifted DBR cavity was designed with a shallowly etched waveguide, small grating modulation depth and longer grating length with submicron size grating period. The Q-factor of the fabricated DBR cavity device with the optimized parameters is measured to be as high as 8×10^4 . The overall footprint of the device is small.

In Chapter 3, a novel integrated optical DBR grating device has been proposed and demonstrated in SOI substrate exhibiting a wavelength transfer function with a sharp-edge or REF response in C-band ($1530\text{nm} \leq \lambda \leq 1565\text{ nm}$). The device working principle is described first with a semi-analytical model and then FDTD simulations results are presented to quantify various figure of merits. Analyzing the simulation results, the design parameters were finalized and subsequently REF devices were fabricated using standard process developed in our laboratory. The characterization results of fabricated REF devices are found to be consistent with theoretical predictions. A filter response with a sharp-step of $> 40\text{ dB}$ is achieved at $\lambda_{edge} \sim 1561\text{ nm}$. The slope of the step S_{edge} is found to be 118 dB/nm and 105 dB/nm for air and DI water claddings, respectively. It has been also shown experimentally that the slope of the REF response can be controlled by varying the grating modulation. Moreover, the rectangular-edge step in the transmission characteristics of fabricated devices is usually followed by a broad pass-band ($\sim 40\text{ nm}$). Such a device can be useful as a long-pass wavelength filter in an on-chip optical WDM networking system. The device can also be used in Raman spectroscopy as it can selectively filter Raman shifted signals from the pump. Besides device demonstration, a qualitative and quantitative discussions are presented in support of various active applications such as refractive index sensor, re-configurable filter response by thermo-optic tuning, and high-speed intensity modulation by integrating p-n/p-i-n diode, etc.

In Chapter 4, we have demonstrated an integrated silicon photonics device which exhibits a delay-free (or resonance-free) photonic passband with highly extinguished side stopbands. The passband width were controlled by cascading the DBR of de-tuned periodicity. The photonic passband filter device is designed with a multi-mode waveguide with side wall grating, which is adiabatically interfaced with input/output single-mode waveguides. The optical passband filter in transmission port of waveguide was demonstrated first time to the best of our knowledge. The pass-bands are bounded by two highly extinguished stop-bands (with extinction of $> 35\text{ dB}$ with edge roll-off of $> 70\text{ dB/nm}$) of $\Delta\lambda_{sb} > 15\text{ nm}$. Existence of two stopband is due two Bragg phase matching conditions. The filter response being in the transmission, flat-top is naturally achieved however passband ripple were further minimized within $\sim 1\text{ dB}$ by providing adiabatic taper at input and output interfaces of DBR grating. The bandwidth is further

narrowed down by cascading two gratings with detuned parameters. A semi-analytical model is used to analyze the filter characteristics ($1500 \text{ nm} \leq \lambda \leq 1650 \text{ nm}$). The pass bandwidth of waveguide devices integrated with a single-stage gratings are measured to be $\sim 24 \text{ nm}$, whereas for the device with two cascaded gratings with slightly detuned periods ($\Delta\Lambda = 2 \text{ nm}$) exhibit pass bandwidth down to $\sim 10 \text{ nm}$. Insertion loss and ripples in the passband can be reduced by improving side-wall roughness and by increasing taper lengths. It has been shown that the spectral widths of photonic passband (and side stopbands) can be engineered depending on various applications.

5.2 Future Scopes

We believe the rectangular edge filter fabricated with DBR in multimode SOI waveguide can be effectively used for designing integrated optical intensity modulator, RF photonics filter, thermo-optic switch and lab-on-chip applications. The demonstrated devices exhibit well-defined wavelength edge (λ_{edge}) will be useful to design compact silicon modulator with similar working principle as ring-resonator based intensity modulators [39] and/or as electro-absorption modulator [93] in ON-OFF configuration but with a very high extinction ratio. Higher edge roll-off of the REF device would find applications in sensors with high sensitive. Photonic passband of the cascaded grating characteristics may be explored for RF photonics filter (for RADAR signal processing) as an alternative to conventional optical notch/band-pass filters [99], in quantum communication by effectively filtering generated entangled photons from the pump signal [26] and Raman spectroscopy [31].

APPENDIX A

List of Publications Based on Thesis

A.0.1 Patent

1. **Parimal Sah** and B. K. Das, "Broadband wavelength filter device using sidewall grating for filtering optical signals", App. No. - PCT/IN2017/050403.

A.0.2 Journal

1. **Parimal Sah**, and B. K. Das, "Photonic Bandpass Filter Characteristics of Multimode SOI Waveguides Integrated with Submicron Gratings" *Manuscript under review*.
2. **Parimal Sah**, and B. K. Das, "Integrated Optical Rectangular-Edge Filter Devices in SOI." *IEEE/OSA Journal of Lightwave Technology* vol. 35 no. 2, pp. 128-135, 2017.
3. B. K. Das, N. DasGupta, S. Chandran, **Parimal Sah** et al., "Silicon Photonics Technology: Ten Years of Research at IIT Madras," *Asian Journal of Physics*, vol. 25, no. 7, 2016.

A.0.3 Conference (Presentations / Proceedings/Workshop)

1. **Parimal Sah** and Bijoy Krishna Das, "Integrated Optical $\lambda/4$ Phase-Shifted High-Q DBR Cavity in Silicon-On-Insulator", selected for Oral Presentation in ICAOP-2017, Hisar, Haryana, India (23-36 November 2017).
2. Sumi R, **Parimal Sah**, and B.K. Das, "Integrated 1D Photonic Crystal Devices with SOI Waveguides", Symposium on Photonic Crystal: 30 Years of Photonic Crystals - the Indian Scenario, IIT Kanpur, 21-23 September 2017.
3. B.K. Das, R.K. Gupta, **Parimal Sah** and S Chandran, "Novel wavelength filter devices in SOI for optical interconnect applications", selected for Invited talk in ICMAT 2017 (18-23 June 2017)
4. **Parimal Sah** and Bijoy Krishna Das, "Broadband wavelength filter device using a sidewall grating in multimode SOI rib waveguide", Oral Presentation in OFC 2017, Los Angeles, CA, USA (19-23 March 2017) .
5. B.K. Das, S. Chandran, **Parimal Sah**, and R.K. Gupta, "Novel wavelength filter devices in SOI for sensing applications", 13th International Conference on Fiber Optics and Photonics, IIT Kanpur, India, 4-8 December 2016 (Invited Talk, Paper- Tu2F.2)
6. B. K. Das, S. Chandran, R. Sidharth, S. Kaushal, and **Parimal Sah**, "Nanoscale Tolerance for Silicon Optical Interconnect Devices", National Conference on Nanoscience and Nanotechnology (NS&NT - 2014), 18-19 September 2014, CRNN, University of Calcutta, Kolkata (Invited Talk)

REFERENCES

- [1] G. Keiser, *Optical fiber communications*. McGraw-Hill New York, 1983.
- [2] G. P. Agrawal, *Fiber-optic communication systems*. John Wiley & Sons, 2012, vol. 222.
- [3] Y. e. Jeong, J. Sahu, D. Payne, and J. Nilsson, “Ytterbium-doped large-core fiber laser with 1.36 kW continuous-wave output power,” *Optics Express*, vol. 12, no. 25, pp. 6088–6092, 2004.
- [4] C. R. Giles and E. Desurvire, “Modeling erbium-doped fiber amplifiers,” *Journal of Lightwave Technology*, vol. 9, no. 2, pp. 271–283, 1991.
- [5] Y. Chen, C. Hu, C. Lee, K. Feng, M. Lu, C.-H. Chang, Y. Tu, and S. Tzeng, “Low-crosstalk and compact optical add-drop multiplexer using a multiport circulator and fiber Bragg gratings,” *IEEE Photonics Technology Letters*, vol. 12, no. 10, pp. 1394–1396, 2000.
- [6] F. Bilodeau, D. Johnson, S. Theriault, B. Malo, J. Albert, and K. Hill, “An all-fiber dense wavelength-division multiplexer/demultiplexer using photoimprinted Bragg gratings,” *IEEE Photonics Technology Letters*, vol. 7, no. 4, pp. 388–390, 1995.
- [7] K. J. Ebeling, *Integrated optoelectronics: waveguide optics, photonics, semiconductors*. Springer Science & Business Media, 2012.
- [8] D. A. Miller, “Device requirements for optical interconnects to silicon chips,” *Proceedings of the IEEE*, vol. 97, no. 7, pp. 1166–1185, 2009.
- [9] R. Kirchain and L. Kimerling, “A roadmap for nanophotonics,” *Nature Photonics*, vol. 1, no. 6, pp. 303–305, 2007.
- [10] A. C. Cangellaris, “The interconnect bottleneck in multi-ghz processors; new opportunities for hybrid electrical/optical solutions,” in *Massively Parallel Processing, 1998. Proceedings. Fifth International Conference on*. IEEE, 1998, pp. 96–103.
- [11] D. Pavesi, “Silicon fundamentals for photonics applications,” *Silicon Photonics*, pp. 2000–2000, 2004.
- [12] R. H. Havemann and J. A. Hutchby, “High-performance interconnects: An integration overview,” *Proceedings of the IEEE*, vol. 89, no. 5, pp. 586–601, 2001.
- [13] R. Soref and B. Bennett, “Electrooptical effects in silicon,” *IEEE Journal of Quantum Electronics*, vol. 23, no. 1, pp. 123–129, 1987.

- [14] D. Thomson, A. Zilkie, J. E. Bowers, T. Komljenovic, G. T. Reed, L. Vivien, D. Marris-Morini, E. Cassan, L. Viroat, J.-M. Fédéli *et al.*, “Roadmap on silicon photonics,” *Journal of Optics*, vol. 18, no. 7, p. 073003, 2016.
- [15] L. Vivien and L. Pavesi, *Handbook of silicon photonics*. Taylor & Francis, 2016.
- [16] A. Inoue, M. Shigehara, M. Ito, M. Inai, Y. Hattori, and T. Mizunami, “Fabrication and application of fiber Bragg grating—a review,” *Optoelectronics-Devices and Technologies*, vol. 10, no. 1, pp. 119–130, 1995.
- [17] S. Devra and G. A. Vikas, “Fabrication and applications of fiber Bragg grating—a review,” *Advanced Engineering Technology and Application*, vol. 4, no. 2, pp. 15–25, 2015.
- [18] J. Chen, B. Liu, and H. Zhang, “Review of fiber Bragg grating sensor technology,” *Frontiers of Optoelectronics in China*, vol. 4, no. 2, pp. 204–212, 2011.
- [19] R. Kashyap, *Fiber Bragg gratings*. Academic press, 2009.
- [20] W. Bogaerts, M. Fiers, and P. Dumon, “Design challenges in silicon photonics,” *IEEE Journal of Selected Topics in Quantum Electronics*, vol. 20, no. 4, pp. 1–8, 2014.
- [21] C. Sun, M. T. Wade, Y. Lee, J. S. Orcutt, L. Alloatti, M. S. Georgas, A. S. Waterman, J. M. Shainline, R. R. Avizienis, S. Lin *et al.*, “Single-chip microprocessor that communicates directly using light,” *Nature*, vol. 528, no. 7583, pp. 534–538, 2015.
- [22] Luxtera, “Luxtera samples world’s first 40 Gigabit optical active cable,,” 2007.
- [23] B. R. Koch, A. Alduino, L. Liao, R. Jones, M. Morse, B. Kim, W.-Z. Lo, J. Basak, H.-F. Liu, H. Rong *et al.*, “A 4x12. 5 Gbps CWDM silicon photonics link using integrated hybrid silicon lasers,” in *CLEO: Science and Innovations*. Optical Society of America, 2011, p. CThP5.
- [24] R. Won and M. Paniccia, “Integrating silicon photonics,” 2010.
- [25] F. E. Doany, B. G. Lee, A. V. Rylyakov, D. M. Kuchta, C. Jahnes, C. Baks, F. Libsch, and C. L. Schow, “Terabit/sec 48-channel fiber-coupled optical module based on holey CMOS transceiver IC,” in *Electronic Components and Technology Conference (ECTC), 2012 IEEE 62nd*. IEEE, 2012, pp. 1499–1504.
- [26] J. W. Silverstone, D. Bonneau, J. L. O’Brien, and M. G. Thompson, “Silicon quantum photonics,” *IEEE Journal of Selected Topics in Quantum Electronics*, vol. 22, no. 6, pp. 390–402, 2016.
- [27] R. Soref, “The past, present, and future of silicon photonics,” *IEEE Journal of Selected Topics in Quantum Electronics*, vol. 12, no. 6, pp. 1678–1687, 2006.
- [28] R. Baets, P. Dumon, W. Bogaerts, G. Roelkens, D. Taillaert, B. Luyssaert, G. Priem, G. Morthier, P. Bienstman, and D. Van Thourhout, “Silicon-on-insulator based nano-photonics: Why, how, what for?” in *Group IV Photonics, 2005. 2nd IEEE International Conference on*. IEEE, 2005, pp. 168–170.

- [29] S. Assefa, S. Shank, W. Green, M. Khater, E. Kiewra, C. Reinholm, S. Kamapurkar, A. Rylyakov, C. Schow, F. Horst *et al.*, “A 90 nm CMOS integrated nano-photonics technology for 25 Gbps WDM optical communications applications,” in *Electron Devices Meeting (IEDM), 2012 IEEE International*. IEEE, 2012, pp. 33–8.
- [30] I. D. Rukhlenko, M. Premaratne, and G. P. Agrawal, “Nonlinear silicon photonics: analytical tools,” *IEEE Journal of Selected Topics in Quantum Electronics*, vol. 16, no. 1, pp. 200–215, 2010.
- [31] S. Fathpour and B. Jalali, *Silicon photonics for telecommunications and biomedicine*. CRC Press, 2011.
- [32] Q. Xu, B. Schmidt, S. Pradhan, and M. Lipson, “Micrometre-scale silicon electro-optic modulator,” *Nature*, vol. 435, no. 7040, p. 325, 2005.
- [33] G. Cocorullo, M. Iodice, and I. Rendina, “All-silicon Fabry–Perot modulator based on the thermo-optic effect,” *Optics Letters*, vol. 19, no. 6, pp. 420–422, 1994.
- [34] H. Park, A. W. Fang, S. Kodama, and J. E. Bowers, “Hybrid silicon evanescent laser fabricated with a silicon waveguide and III-V offset quantum wells,” *Optics Express*, vol. 13, no. 23, pp. 9460–9464, 2005.
- [35] B. Chmielak, M. Waldow, C. Matheisen, C. Ripperda, J. Bolten, T. Wahlbrink, M. Nagel, F. Merget, and H. Kurz, “Pockels effect based fully integrated, strained silicon electro-optic modulator,” *Optics Express*, vol. 19, no. 18, pp. 17 212–17 219, 2011.
- [36] W. S. Fegadolli, N. Pavarelli, P. O’Brien, S. Njoroge, V. R. Almeida, and A. Scherer, “Thermally controllable silicon photonic crystal nanobeam cavity without surface cladding for sensing applications,” *ACS Photonics*, vol. 2, no. 4, pp. 470–474, 2015.
- [37] W. S. Fegadolli, J. E. Oliveira, V. R. Almeida, and A. Scherer, “Compact and low power consumption tunable photonic crystal nanobeam cavity,” *Optics Express*, vol. 21, no. 3, pp. 3861–3871, 2013.
- [38] X. Duan, Y. Huang, Y. Cui, J. Wang, and C. M. Lieber, “Indium phosphide nanowires as building blocks for nanoscale electronic and optoelectronic devices,” *Nature*, vol. 409, no. 6816, pp. 66–69, 2001.
- [39] G. T. Reed, G. Mashanovich, F. Gardes, and D. Thomson, “Silicon optical modulators,” *Nature Photonics*, vol. 4, no. 8, pp. 518–526, 2010.
- [40] L. Chrostowski and M. Hochberg, *Silicon photonics design: from devices to systems*. Cambridge University Press, 2015.
- [41] M. Hochberg and T. Baehr-Jones, “Towards fabless silicon photonics,” *Nature Photonics*, vol. 4, no. 8, pp. 492–494, 2010.

- [42] L. B. Soldano and E. C. Pennings, “Optical multi-mode interference devices based on self-imaging: principles and applications,” *Journal of Lightwave Technology*, vol. 13, no. 4, pp. 615–627, 1995.
- [43] M. Bachmann, P. A. Besse, and H. Melchior, “General self-imaging properties in $n \times n$ multimode interference couplers including phase relations,” *Applied Optics*, vol. 33, no. 18, pp. 3905–3911, 1994.
- [44] P. Orlandi, F. Morichetti, M. J. Strain, M. Sorel, A. Melloni, and P. Bassi, “Tunable silicon photonics directional coupler driven by a transverse temperature gradient,” *Optics Letters*, vol. 38, no. 6, pp. 863–865, 2013.
- [45] Z. Lu, H. Yun, Y. Wang, Z. Chen, F. Zhang, N. A. Jaeger, and L. Chrostowski, “Broadband silicon photonic directional coupler using asymmetric-waveguide based phase control,” *Optics Express*, vol. 23, no. 3, pp. 3795–3808, 2015.
- [46] A. Liu, R. Jones, L. Liao, D. Samara-Rubio, D. Rubin, O. Cohen, R. Nicolaescu, and M. Paniccia, “A high-speed silicon optical modulator based on a metal–oxide–semiconductor capacitor,” *Nature*, vol. 427, no. 6975, pp. 615–618, 2004.
- [47] J. Niehusmann, A. Vörckel, P. H. Bolivar, T. Wahlbrink, W. Henschel, and H. Kurz, “Ultrahigh-quality-factor silicon-on-insulator microring resonator,” *Optics Letters*, vol. 29, no. 24, pp. 2861–2863, 2004.
- [48] P. Dumon, W. Bogaerts, D. Van Thourhout, D. Taillaert, R. Baets, J. Wouters, S. Beckx, and P. Jaenen, “Compact wavelength router based on a silicon-on-insulator arrayed waveguide grating pigtailed to a fiber array,” *Optics Express*, vol. 14, no. 2, pp. 664–669, 2006.
- [49] T. E. Murphy, “Design, fabrication and measurement of integrated Bragg grating optical filters,” Ph.D. dissertation, Massachusetts Institute of Technology, 2001.
- [50] M. Moharam and T. K. Gaylord, “Diffraction analysis of dielectric surface-relief gratings,” *JOSA*, vol. 72, no. 10, pp. 1385–1392, 1982.
- [51] A. Yariv and P. Yeh, *Photonics: optical electronics in modern communications*. Oxford University Press New York, 2007, vol. 6.
- [52] P. Prabhathan, V. Murukeshan, Z. Jing, and P. V. Ramana, “Compact SOI nanowire refractive index sensor using phase shifted Bragg grating,” *Optics Express*, vol. 17, no. 17, pp. 15 330–15 341, 2009.
- [53] X. Wang, “Silicon photonic waveguide Bragg gratings,” Ph.D. dissertation, University of British Columbia, 2013.
- [54] C. A. Barrios, V. R. De Almeida, and M. Lipson, “Low-power-consumption short-length and high-modulation-depth silicon electrooptic modulator,” *Journal of Lightwave Technology*, vol. 21, no. 4, pp. 1089–1098, 2003.
- [55] J. Schmid, P. Cheben, P. Bock, R. Halir, J. Lapointe, S. Janz, A. Delage, A. Densmore, J.-M. Fedeli, T. Hall *et al.*, “Refractive index engineering with subwavelength gratings in silicon microphotonic waveguides,” *IEEE Photonics Journal*, vol. 3, no. 3, pp. 597–607, 2011.

- [56] R. Halir, A. Ortega-Monux, J. H. Schmid, C. Alonso-Ramos, J. Lapointe, D.-X. Xu, J. G. Wangüemert-Pérez, I. Molina-Fernandez, and S. Janz, “Recent advances in silicon waveguide devices using sub-wavelength gratings,” *IEEE Journal of Selected Topics in Quantum Electronics*, vol. 20, no. 4, pp. 279–291, 2014.
- [57] L. H. Gabrielli, J. Cardenas, C. B. Poitras, and M. Lipson, “Silicon nanostructure cloak operating at optical frequencies,” *Nature Photonics*, vol. 3, no. 8, pp. 461–463, 2009.
- [58] D. Taillaert, P. Bienstman, and R. Baets, “Compact efficient broadband grating coupler for silicon-on-insulator waveguides,” *Optics Letters*, vol. 29, no. 23, pp. 2749–2751, 2004.
- [59] T. E. Murphy, J. T. Hastings, and H. I. Smith, “Fabrication and characterization of narrow-band Bragg-reflection filters in silicon-on-insulator ridge waveguides,” *Journal of Lightwave Technology*, vol. 19, no. 12, p. 1938, 2001.
- [60] X. Wang, W. Shi, H. Yun, S. Grist, N. A. Jaeger, and L. Chrostowski, “Narrow-band waveguide Bragg gratings on SOI wafers with CMOS-compatible fabrication process,” *Optics Express*, vol. 20, no. 14, pp. 15 547–15 558, 2012.
- [61] M. W. Pruessner, T. H. Stievater, and W. S. Rabinovich, “Integrated waveguide Fabry-Perot microcavities with silicon/air Bragg mirrors,” *Optics Letters*, vol. 32, no. 5, pp. 533–535, 2007.
- [62] A. W. Fang, B. R. Koch, R. Jones, E. Lively, D. Liang, Y.-H. Kuo, and J. E. Bowers, “A distributed Bragg reflector silicon evanescent laser,” *IEEE Photonics Technology Letters*, vol. 20, no. 20, pp. 1667–1669, 2008.
- [63] I. Giuntoni, D. Stolarek, A. Gajda, G. Winzer, J. Bruns, B. Tillack, K. Petermann, and L. Zimmermann, “Integrated drop-filter for dispersion compensation based on SOI rib waveguides,” in *Optical Fiber Communication (OFC), collocated National Fiber Optic Engineers Conference, 2010 Conference on (OFC/NFOEC)*. IEEE, 2010, pp. 1–3.
- [64] D. Tan, K. Ikeda, and Y. Fainman, “Coupled chirped vertical gratings for on-chip group velocity dispersion engineering,” *Applied Physics Letters*, vol. 95, no. 14, p. 141109, 2009.
- [65] D. Tan, K. Ikeda, R. Saperstein, B. Slutsky, and Y. Fainman, “Chip-scale dispersion engineering using chirped vertical gratings,” *Optics Letters*, vol. 33, no. 24, pp. 3013–3015, 2008.
- [66] A. Ricciardi, S. Campopiano, A. Cusano, T. F. Krauss, and L. O’Faolain, “Broadband mirrors in the near-infrared based on subwavelength gratings in SOI,” *IEEE Photonics Journal*, vol. 2, no. 5, pp. 696–702, 2010.
- [67] Y. Wang, X. Wang, J. Flueckiger, H. Yun, W. Shi, R. Bojko, N. A. Jaeger, and L. Chrostowski, “Focusing sub-wavelength grating couplers with low back reflections for rapid prototyping of silicon photonic circuits,” *Optics Express*, vol. 22, no. 17, pp. 20 652–20 662, 2014.

- [68] P. J. Bock, P. Cheben, J. H. Schmid, J. Lapointe, A. Delâge, S. Janz, G. C. Aers, D.-X. Xu, A. Densmore, and T. J. Hall, "Subwavelength grating periodic structures in silicon-on-insulator: a new type of microphotonic waveguide," *Optics Express*, vol. 18, no. 19, pp. 20 251–20 262, 2010.
- [69] W. Bogaerts, P. Dumon, D. Van Thourhout, and R. Baets, "Low-loss, low-cross-talk crossings for silicon-on-insulator nanophotonic waveguides," *Optics Letters*, vol. 32, no. 19, pp. 2801–2803, 2007.
- [70] P. Sanchis, P. Villalba, F. Cuesta, A. Håkansson, A. Griol, J. V. Galán, A. Brimont, and J. Martí, "Highly efficient crossing structure for silicon-on-insulator waveguides," *Optics Letters*, vol. 34, no. 18, pp. 2760–2762, 2009.
- [71] V. Donzella, A. Sherwali, J. Flueckiger, S. M. Grist, S. T. Fard, and L. Chrostowski, "Design and fabrication of SOI micro-ring resonators based on sub-wavelength grating waveguides," *Optics Express*, vol. 23, no. 4, pp. 4791–4803, 2015.
- [72] J. Wang, I. Glesk, and L. R. Chen, "Subwavelength grating filtering devices," *Optics Express*, vol. 22, no. 13, pp. 15 335–15 345, 2014.
- [73] W. S. Zaoui, A. Kunze, W. Vogel, M. Berroth, J. Butschke, F. Letzkus, and J. Burghartz, "Bridging the gap between optical fibers and silicon photonic integrated circuits," *Optics Express*, vol. 22, no. 2, pp. 1277–1286, 2014.
- [74] F. Van Laere, T. Claes, J. Schrauwen, S. Scheerlinck, W. Bogaerts, D. Taillaert, L. O'Faolain, D. Van Thourhout, and R. Baets, "Compact focusing grating couplers for silicon-on-insulator integrated circuits," *IEEE Photonics Technology Letters*, vol. 19, no. 23, pp. 1919–1921, 2007.
- [75] D. Vermeulen, S. Selvaraja, P. Verheyen, G. Lepage, W. Bogaerts, P. Absil, D. Van Thourhout, and G. Roelkens, "High-efficiency fiber-to-chip grating couplers realized using an advanced CMOS-compatible silicon-on-insulator platform," *Optics Express*, vol. 18, no. 17, pp. 18 278–18 283, 2010.
- [76] X. Wang, W. Shi, R. Vafaei, N. A. Jaeger, and L. Chrostowski, "Uniform and sampled Bragg gratings in SOI strip waveguides with sidewall corrugations," *IEEE Photonics Technology Letters*, vol. 23, no. 5, pp. 290–292, 2011.
- [77] S.-L. Tsao, J.-H. Tien, and C.-W. Tsai, "Simulations on an SOI grating-based optical add/drop multiplexer," *IEEE Journal of Selected Topics in Quantum Electronics*, vol. 8, no. 6, pp. 1277–1284, 2002.
- [78] J. St-Yves, H. Bahrami, P. Jean, S. LaRochelle, and W. Shi, "Widely bandwidth-tunable silicon filter with an unlimited free-spectral range," *Optics Letters*, vol. 40, no. 23, pp. 5471–5474, 2015.
- [79] K. Koo and A. Kersey, "Bragg grating-based laser sensors systems with interferometric interrogation and wavelength division multiplexing," *Journal of Light-wave Technology*, vol. 13, no. 7, pp. 1243–1249, 1995.

- [80] L. Eldada, S. Yin, C. Poga, C. Glass, R. Blomquist, and R. Nonwood, "Integrated multichannel OADMs using polymer Bragg grating MZIs," *IEEE Photonics Technology Letters*, vol. 10, no. 10, pp. 1416–1418, 1998.
- [81] M. Caverley, X. Wang, K. Murray, N. A. Jaeger, and L. Chrostowski, "Silicon-on-insulator modulators using a quarter-wave phase-shifted Bragg grating," *IEEE Photonics Technology Letters*, vol. 27, no. 22, pp. 2331–2334, 2015.
- [82] A. D. Simard and S. LaRochelle, "A dynamic model of silicon Bragg grating modulators," *IEEE Journal of Selected Topics in Quantum Electronics*, vol. 22, no. 6, pp. 107–115, 2016.
- [83] S. Akiyama, M. Imai, T. Baba, T. Akagawa, N. Hirayama, Y. Noguchi, M. Seki, K. Koshino, M. Toyama, T. Horikawa *et al.*, "Compact pin-diode-based silicon modulator using side-wall-grating waveguide," *IEEE Journal of Selected Topics in Quantum Electronics*, vol. 19, no. 6, pp. 74–84, 2013.
- [84] M. Verbist, W. Bogaerts, and D. Van Thourhout, "Design of weak 1-d Bragg grating filters in SOI waveguides using volume holography techniques," *Journal of Lightwave Technology*, vol. 32, no. 10, pp. 1915–1920, 2014.
- [85] V. Veerasubramanian, G. Beaudin, A. Giguère, B. Le Drogoff, V. Aimez, and A. G. Kirk, "Waveguide-coupled drop filters on SOI using quarter-wave shifted sidewalled grating resonators," *Optics Express*, vol. 20, no. 14, pp. 15 983–15 990, 2012.
- [86] Y.-B. Cho, B.-K. Yang, J.-H. Lee, J.-B. Yoon, and S.-Y. Shin, "Silicon photonic wire filter using asymmetric sidewall long-period waveguide grating in a two-mode waveguide," *IEEE Photonics Technology Letters*, vol. 20, no. 7, pp. 520–522, 2008.
- [87] S. Honda, Z. Wu, J. Matsui, K. Utaka, T. Edura, M. Tokuda, K. Tsutsui, and Y. Wada, "Largely-tunable wideband Bragg gratings fabricated on SOI rib waveguides employed by deep-RIE," *Electronics Letters*, vol. 43, no. 11, pp. 630–631, 2007.
- [88] P. Prabhathan, V. Murukeshan, and Z. Jing, "Compact resonant Bragg grating filters using submicron silicon-on-insulator (SOI) waveguide for optical communication network," in *Photonics Asia 2010*. International Society for Optics and Photonics, 2010, pp. 78 470H–78 470H.
- [89] P. Prabhathan, V. Murukeshan, Z. Jing, and P. V. Ramana, "Broadband tunable bandpass filters using phase shifted vertical side wall grating in a submicrometer silicon-on-insulator waveguide," *Applied Optics*, vol. 48, no. 29, pp. 5598–5603, 2009.
- [90] Y. Painchaud, M. Poulin, C. Latrasse, and M.-J. Picard, "Bragg grating based Fabry–Perot filters for characterizing silicon-on-insulator waveguides," in *Group IV Photonics (GFP), 9th International Conference*. IEEE, 2012, pp. 180–182.

- [91] Z. Zou, L. Zhou, M. Wang, K. Wu, and J. Chen, “Tunable spiral Bragg gratings in 60-nm-thick silicon-on-insulator strip waveguides,” *Optics Express*, vol. 24, no. 12, pp. 12 831–12 839, 2016.
- [92] N. N. Klimov, T. Purdy, and Z. Ahmed, “Fabrication and characterization of on-chip integrated silicon photonic Bragg grating and photonic crystal cavity thermometers,” *arXiv preprint arXiv:1508.01419*, 2015.
- [93] J. Liu, M. Beals, A. Pomerene, S. Bernardis, R. Sun, J. Cheng, L. C. Kimerling, and J. Michel, “Waveguide-integrated, ultralow-energy GeSi electro-absorption modulators,” *Nature Photonics*, vol. 2, no. 7, pp. 433–437, 2008.
- [94] “Lumerical inc. <http://www.lumerical.com/tcad-products/mode/>.”
- [95] S. Chandran, R. K. Gupta, and B. K. Das, “Dispersion enhanced critically coupled ring resonator for wide range refractive index sensing,” *IEEE Journal of Selected Topics in Quantum Electronics*, vol. 23, no. 2, pp. 1–9, 2017.
- [96] S. Chandran, R. K. Gupta, and B. K. Das, “Dispersion enhanced critically coupled ring resonator for wide range refractive index sensing,” *IEEE Journal of Selected Topics in Quantum Electronics*, vol. 23, no. 2, pp. 1–9, 2017.
- [97] A. Yariv, “Coupled-mode theory for guided-wave optics,” *IEEE Journal of Quantum Electronics*, vol. 9, no. 9, pp. 919–933, 1973.
- [98] P. Sah and B. K. Das, “Integrated optical rectangular-edge filter devices in SOI,” *Journal of Lightwave Technology*, vol. 35, no. 2, pp. 128–135, 2017.
- [99] R. A. Minasian, “Photonic signal processing of microwave signals,” *IEEE Transactions on Microwave Theory and Techniques*, vol. 54, no. 2, pp. 832–846, 2006.
- [100] M.-C. Estevez, M. Alvarez, and L. M. Lechuga, “Integrated optical devices for lab-on-a-chip biosensing applications,” *Laser & Photonics Reviews*, vol. 6, no. 4, pp. 463–487, 2012.
- [101] K. Tan, G. Singh, C. Herrington, and C. Brown, “Near-infrared raman spectroscopy using hollow-core photonic bandgap fibers,” *Optics Communications*, vol. 283, no. 16, pp. 3204–3206, 2010.
- [102] P. Dumais, D. Goodwill, M. Kiaei, D. Celo, J. Jiang, C. Zhang, F. Zhao, X. Tu, C. Zhang, S. Yan *et al.*, “Silicon photonic switch subsystem with 900 monolithically integrated calibration photodiodes and 64-fiber package,” in *Optical Fiber Communication Conference*. Optical Society of America, 2017, pp. W4E–4.
- [103] S. Kaushal and B. K. Das, “Modeling and experimental investigation of an integrated optical microheater in silicon-on-insulator,” *Applied Optics*, vol. 55, no. 11, pp. 2837–2842, 2016.
- [104] O. Dubray, A. Abraham, K. Hassan, S. Olivier, D. Marris-Morini, L. Vivien, I. O’Connor, and S. Menezo, “Electro-optical ring modulator: An ultracompact model for the comparison and optimization of p-n, p-i-n, and capacitive junction,” *IEEE Journal of Selected Topics in Quantum Electronics*, vol. 22, no. 6, pp. 1–10, 2016.

- [105] S. Khan and S. Fathpour, “Demonstration of complementary apodized cascaded grating waveguides for tunable optical delay lines,” *Optics Letters*, vol. 38, no. 19, pp. 3914–3917, 2013.
- [106] A. S. Chang, W. Wu, and S. Y. Chou, “Cascaded subwavelength resonant grating filters for flat-top spectral response,” in *Lasers and Electro-Optics, 2003. CLEO’03. Conference.* IEEE, 2003, pp. 2–pp.